UNIVERSITÀ DEGLI STUDI DI PADOVA

UNIVERSITÀ DEGLI STUDI DI NAPOLI FEDERICO II

Università degli Studi di Padova

Centro interdipartimentale "Centro Ricerche Fusione"

Università di Napoli Federico II

JOINT RESEARCH DOCTORATE IN FUSION SCIENCE AND ENGINEERING

Cycle XXXVI

Investigation of corrosion-erosion phenomena in primary cooling circuits of reactor components

Coordinator:

Prof. Gianmaria De Tommasi

Supervisors:

Prof. Piergiorgio Sonato

Dr. Mauro Dalla Palma

Ph.D Student: Caterina Cavallini

Padova, October 2023

Abstract

Components within nuclear reactors and fusion facilities are subjected to severe conditions, primarily characterized by the need to endure high thermal fluxes (up to tens of MW/m^2) and high voltages (up to 1MV). Consequently, the units responsible for initiating, supporting, and operating a fusion reaction require active cooling through primary heat transfer systems, typically utilizing high-purity water to minimize transport of impurities and current leakage along the cooling circuits of high-voltage components.

The water circulating through pipes and structures interacts with the inner surfaces of channels made of copper alloys and aluminium, all of which possess high thermal diffusivity, and stainless steel. This interaction can lead to the thinning of cooling channel walls over time, potentially resulting in sudden failures. To mitigate corrosion and erosion phenomena, robust designs are crucial, and ongoing monitoring of water chemistry characteristics is essential to minimize the formation of corrosion products, thereby enhancing the performance of reactors and experimental facilities.

The investigation into localized and distributed corrosion-erosion phenomena takes into account factors such as water conductivity, leakage current, dissolved oxygen and carbon dioxide levels, pH, flow velocity, and temperature. In fusion systems, where dissimilar metal junctions and electrical polarization are commonly present, galvanic corrosion can also pose a concern. Moreover, impurities can exacerbate corrosion when they are transported and trapped in crevices.

The focus of this Industrial Doctorate project is to study and investigate the causes of water chemistry degradation and corrosion-erosion phenomena, particularly within components of the ITER Neutral Beam Test Facility (NBTF) that are cooled by ultrapure water with resistivity values up to 10 MΩ·cm. The NBTF, located at Consorzio RFX in Padua, Italy, hosts two experiments: MITICA, a 1 MeV full-scale prototype of the ITER Neutral Beam Injector (NBI), and SPIDER, the low-energy 100 keV ITER NBI full-size Ion Source.

The investigation commenced by examining the main components used in the primary cooling systems of SPIDER and MITICA, which are primarily made of copper alloys and stainless steel. Metal release tests were conducted to estimate the corrosion rate of these materials under various environmental conditions, including oxidizing and reducing environments. Furthermore, the corrosion rates were determined when these materials were coupled and joined, as is the case in NBTF, using a specific joining technique known as Vacuum Tight Threaded Junction (VTTJ). Particular attention was paid to characterizing copper oxides formed in both high and low oxygen environments. Metal releases tests results were compared with preliminary Stress Corrosion Cracking analyses of copper and stainless steel samples exposed to the same environmental conditions of the metal releases experiment ones.

The second part of the analysis focused on investigating water degradation within some of the primary circuits of SPIDER and MITICA. The most significant degradation was

observed in the primary circuits cooling the power supplies. Specific circulation tests were conducted at constant temperature and flow rate to estimate the increase in conductivity and measure the metallic cations dissolved in the water using the Inductively Coupled Plasma-Mass Spectrometry (ICP-MS) technique. Undesirable metals, such as zinc, were identified.

The associations between the experimental observation and the material characterization carried out during this Industrial Doctorate project identified potential circuit improvements proposed and tested to mitigate water degradation and to prevent thinning of cooling channel walls. To address these issues, online sensors were recommended and subsequently installed in a SPIDER primary circuit. These sensors are designed to continuously monitor oxygen levels and ph. Their data will be utilized as soon as SPIDER resumes operation. Additionally, modifications were proposed and implemented in a MITICA primary circuit to minimize the ingress of air from elevated locations within the plant. These adjustments have proven effective in reducing water degradation. Additionally, online mixed bed resins were introduced to ensure a continuous purification of water in the primary loops, thereby maintaining low levels of water conductivity as a first complemental solution to the cyclic replacement of the degraded water.

Riassunto

I componenti all'interno dei reattori nucleari e di quelli sperimentali da fusione sono sottoposti a severe condizioni, principalmente caratterizzate dalla necessità di resistere a elevati flussi termici (fino a decine di MW/m^2) e alte tensioni elettriche (fino a 1 MV). Di conseguenza, tutti i componenti e le unità responsabili di iniziare, sostenere ed operare una reazione di fusione richiedono un raffreddamento attivo attraverso sistemi di trasferimento del calore primari. Questi sistemi tipicamente usano acqua ultrapura per minimizzare il trasporto di impurità e le correnti di fuga lungo i circuiti dei componenti ad alta tensione.

L'acqua che circola attraverso tubazioni e strutture interagisce con le superfici interne dei canali realizzati con materiali ad alta diffusività termica, come leghe di rame, alluminio, e materiali più resistenti alla corrosione, come l'acciaio inossidabile. Questa interazione può portare ad un assottigliamento nel tempo delle pareti dei canali di raffreddamento, potenzialmente causando guasti improvvisi. Per mitigare fenomeni di corrosione ed erosione, sono cruciali lo studio e il progetto meticoloso di ogni singolo componente e il monitoraggio continuo delle caratteristiche chimiche dell'acqua al fine di ridurre al minimo la formazione di prodotti di corrosione, migliorando così le prestazioni dei reattori e delle apparecchiature sperimentali.

L'indagine sui fenomeni di corrosione ed erosione, sia localizzata che distribuita, comprende lo studio e il monitoraggio di parametri come la conducibilità dell'acqua, la corrente di fuga, i livelli di ossigeno e di anidride carbonica disciolti, il pH, la velocità di flusso e la temperatura. Nei reattori sperimentali a fusione, dove sono comunemente presenti giunzioni di metalli dissimili e polarizzazione elettrica, la corrosione galvanica può rappresentare un potenziale problema, così come le impurità che possono essere trasportate e intrappolate in fessure, esacerbando i fenomeni corrosivi.

Questo progetto di Dottorato Industriale verte principalmente sullo studio e sull'indagine delle cause della degradazione della chimica dell'acqua e dei fenomeni di corrosione ed erosione, in particolare all'interno dei componenti della Neutral Beam Test Facility (NBTF) di ITER, raffreddati con acqua ultrapura con valori di resistività fino a 10 MΩ·cm. La NBTF, situata presso il Consorzio RFX a Padova, Italia, ospita due esperimenti: MITICA, un prototipo in grandezza reale da 1 MeV dell'Iniettore di Fasci Neutrali (NBI) di ITER, e SPIDER, la sorgente di ioni a piena taglia da 100 keV per l'NBI di ITER.

L'indagine è iniziata esaminando i principali componenti presenti nei sistemi di raffreddamento primario di SPIDER e MITICA, principalmente composti da leghe di rame e acciaio inossidabile. Sui metalli sono stati condotti test di rilascio per stimare il tasso di corrosione di questi materiali in diverse condizioni ambientali, compresi ambienti ossidanti

e riducenti. Inoltre, sono stati determinati i tassi di corrosione quando questi materiali sono accoppiati e uniti, come nel caso della giunzione "Vacuum Tight Threaded Junction" (VTTJ), utilizzata a NBTF. Particolare attenzione è stata dedicata alla caratterizzazione degli ossidi di rame formati in ambienti ad alto e basso contenuto di ossigeno. I risultati degli esperimenti di rilascio sono stati confrontati con i risultati di prime analisi di tensocorrosione di provini di acciaio e rame esposti nelle medesime condizioni degli esperimenti di rilascio.

La seconda parte dell'analisi si è concentrata sull'indagine sulla degradazione dell'acqua in alcuni dei circuiti primari di SPIDER e MITICA. La degradazione più significativa è stata osservata nei circuiti primari che raffreddano le alimentazioni elettriche. Sono stati condotti specifici test di circolazione a temperatura e portate costanti per stimare l'aumento della conducibilità e misurare i cationi metallici disciolti nell'acqua utilizzando la tecnica dell'Inductively Coupled Plasma-Mass Spectrometry (ICP-MS). Sono stati identificati metalli indesiderati, come lo zinco.

Le associazioni tra le osservazioni sperimentali e la caratterizzazione dei materiali effettuata durante questo progetto di Dottorato Industriale hanno identificato possibili miglioramenti dei circuiti che sono stati in primis proposti e successivamente testati per mitigare la degradazione dell'acqua e prevenire l'assottigliamento delle pareti dei canali di raffreddamento. Per affrontare questi problemi, sono stati raccomandati e successivamente installati sensori in linea in un circuito primario di SPIDER. Questi sensori sono progettati per monitorare continuamente i livelli di ossigeno e il pH. I loro dati saranno utilizzati non appena SPIDER rientrerà in operazione. Inoltre, sono state proposte e implementate modifiche in un circuito primario di MITICA per ridurre al minimo l'ingresso di aria dalle regioni più elevate dell'impianto. Queste modifiche si sono dimostrate efficaci nel ridurre la degradazione dell'acqua. Inoltre, come prima soluzione complementare alla sostituzione ciclica dell'acqua degradata, sono state testate resine a letto misto in linea per garantire una purificazione continua dell'acqua nei circuiti primari, mantenendo così bassi i livelli di conducibilità dell'acqua.

General Structure of the Work

The work performed for this thesis is presented in nine chapters. The first chapter, gives an overview of the fusion and NBI, focusing on NBTF, where this work of thesis was carried out. In Chapter 2, a brief overview of the importance of water quality in nuclear power plants and fusion facilities is given. Additionally, the prime parameters and processes that are relevant for the interaction between water and reactor components are presented. Chapter 3 deals of material degradation exposed to Ultrapure Water. Mechanisms of material degradation within reactor water systems will be explored, with a specific focus on copper and stainless steel, the main materials utilized in SPIDER and MITICA. Chapter 4 includes a general overview of the techniques used to characterize the materials presented in this thesis. In Chapter 5, an investigation into the general corrosion behaviour of copper and stainless steel in ultrapure water is presented by metal release experiments. Preliminary Stress Corrosion Cracking initiation tests are reported as a support of metal release results. Chapter 6 and Chapter 7 deals with the water degradation issue related to some of NBTF Primary Circuits (PCs), specifically the ones responsible for cooling down the power supplies, designated as PC01 for SPIDER and PC08 for MITICA. Circulation tests were performed on PC01, PC03, which was taken as reference circuit, and PC08 in order to determine the main causes of water degradation occurring. Some improvements were suggested and implemented. Finally, summary and future works are presented in the “Conclusions” and “Future Works” chapters.

List of Publications

Journal Publications

a) Investigation on Caesium Dispersion and Molybdenum Coating on SPIDER Component
DocumentID: 32922
DOI: 10.3390/ma16010206 1
Authors: *C. Cavallini*, V. Candela et al

b) On the road to ITER NBIs: SPIDER improvement after first operation and MITICA construction progress
DocumentID: 30319
DOI: 10.1016/j.fusengdes.2021.112622
Authors: V. Toigo *et al*

c) Design of a large non-evaporable getter pump for the full size ITER beam source prototype
DocumentID: 35840
DOI: 10.1116/6.0002395
Authors: E. Sartori *et al*

d) First operations with caesium of the negative ion source SPIDER
DocumentID: 33000
DOI: 10.1088/1741-4326/ac715e
Authors: E. Sartori *et al*

e) SPIDER, the negative ion source prototype for ITER: overview of operations and caesium injection
DocumentID: 32998
DOI: 10.1109/TPS.2022.3226239
Authors: G. Serianni *et al*

Conference Publications

a) Investigations of corrosion-erosion phenomena in the primary cooling system of SPIDER
DocumentID: 28483
DOI: 10.1016/j.fusengdes.2021.112271
Authors: *C. Cavallini* et al

b) Corrosion and metal release of copper and stainless steel exposed to Ultrapure Water
DocumentID: 31407

DOI: 10.1109/TPS.2022.3182804
Authors: *C. Cavallini* et al

c) Study, design and thermal-hydraulic simulations of Vacuum Enhancement Module cooling circuit
DocumentID: 33106
DOI: 10.1016/j.fusengdes.2023.113926
Authors: *C. Cavallini* et al

f) Lessons learned after three years of SPIDER operation and the first MITICA integrated tests
DocumentID: 33244
DOI: 10.1016/j.fusengdes.2023.113590
Authors: D. Marcuzzi *et al*

g) Status of the SPIDER source after 3.5 years operation
DocumentID: 33215
DOI: 0.1016/j.fusengdes.2023.113831
Authors: M. Pavei *et al*

h) Water degradation in ITER Neutral Beam Test Facility cooling circuits
DocumentID: 30449
DOI: 10.1109/TPS.2022.3173737
Authors: C. Gasparrini *et al*

Oral Presentations

a) Environmental Degradation of Materials on Nuclear Power Systems – Water Reactors (ENVDEG2022). Title of the work "Investigation on release rates of Vacuum Tight Threaded Junction (VTTJ) samples exposed to ultrapure water"

List of Figures

List of Tables

Abbreviations

AGPS	Acceleration Grid Power Supply
ASTM	American Society for Testing and Materials
BP	Bias Plate
BS	Beam Source
BSE	Back Scattered Electrons
BWR	Boiling Water Reactor
CCS	Chemical Control System
CEASC	Centro di Analisi e Servizi Per la Certificazione
CVCS	Chemical and Volume Control System
CP	Cooling Plant
DEMO	DEMOnstration power plant
DO	Dissolved Oxygen
DP	Driver Plate
DTT	Divertor Tokamak Test
ECP	Electrochemical Corrosion Potential
EDS	Energy Dispersive X- ray Spectroscopy
EG	Extraction Grid
EIA	Energy Information Administration
EPDM	Ethylene-Propylene Diene Monomer
ERID	Electrostatic Residual Ion Dump
FAC	Flow Accelerated Corrosion
FSBP	Faraday Shield Back Plate
FSLW	Faraday Shields Lateral Walls
GG	Grounded Grid
HNBR	Hydrogenated Nitrile Butadiene Rubber
HO	High Oxygen
HV	High Voltage

HVD	High Voltage Deck
HX	Heat eXchanger
ICMATE	Instituto di Chimica della Materia Condensata e di Tecnologie per l'Energia
ICP-MS	Inductively Coupled Plasma Mass Spectrometry
ICP-OES	Inductively Coupled Plasma Optical Emission Spectrometry
ISBI	Ion Source BIas power supply
ISEG	Ion Source Extraction Grid power supply
ISEPS	Ion Source and Extraction Power Supplies
ISFB	Ion Source Filament Bias power supply
ISFH	Ion Source Filament Heater power supply
ISO	International Organization for Standardization
ISRF	Ion Source Radio-Frequency power supply
ISS1, ISS2	Ion Source core Snubber bias circuit power supply
ISSS	Ion Source Support power Supply
JET	Joint European Torus
JT-60A	Japan Torus 60 Super Advanced
LO	Low Oxygen
LOD	Limit of Detection
MaMuG	Multi Aperture Grids
MITICA	Megavolt ITER Injector and Concept Advancement
NBR	Nitrile Butadiene Rubber
NED	Neutraliser and Electron Dump
NBI	Neutral Beam Injection
NBTF	Neutral Beam Test Facility
PC	Primary Circuit
PF	Poloidal Field
PFA	PerFluoroAlkoxy
PG	Plasma Grid
PP	PolyPropylene

PP-RCT	PolyPropylene-Random Cristallinity Temperature
PRIMA	Padova Research on ITER Megavolt Accelerator
PRZ	Pressurizer
PS	Power Supplies
PWR	Pressurized Water Reactor
RF	Radio-Frequency
RFP	Reversed Field Pinch
SC	Secondary Circuit
SCC	Stress Corrosion Cracking
SCE	Saturated Calomel Electrode
SEI	Secondary Electrons Imaging
SEM	Scanning Electron Microscope
SCE	Saturated Calomel Electrode
SCLW	Source Case Lateral Wall
SD	Standard Deviation
SPIDER	Source for Productions of Ions of Deuterium Extracted from a Radio-frequency plasma
TC	Tertiary Circuit
TCWS	Tokamak Cooling Water System
TL	Trasmission Line
TPS	Testing Power Supply
TS	Tensile Stress
UPW	Ultrapure Water
VTTJ	Vacuum Tight Threaded Junction
VV	Vacuum Vessel
WB	Water Basin
WDS	Wavelength Dispersive X-ray Spectroscopy
XRD	X-ray Diffraction

Index

Chapter 1
Fusion and NBI

Components within nuclear reactors and fusion facilities face harsh conditions, primarily characterized by the requirement to withstand intense thermal fluxes (reaching up to tens of MW/m^2) and high voltages (up to 1MV). Consequently, the systems responsible for initiating, supporting, and operating fusion reactions necessitate active cooling through primary heat transfer systems. These systems typically employ high-purity water to minimize current leakage along the cooling pathways of high-voltage components. The challenges associated with using water as a coolant in fusion facilities are reminiscent of those observed in fission reactors.

Considering that this thesis work was primarily conducted at the Neutral Beam Test Facility (NBTF) in Padua, a fusion facility, this first chapter addresses the need to explore alternative energy sources to carbon-based ones. Fusion energy emerges as one of the potential solutions, and its fundamental principles are elaborated upon. Tokamak machines are introduced as the predominant type of fusion reactors currently under study and investigation.

Subsequently, in the third and fourth sections, we delve into the specifics of Neutral Beam Injection (NBI) technology and provide an overview of the NBTF and the Padova Research on ITER Megavolt Accelerator (PRIMA) facilities. The final part of this chapter provides an introduction to the cooling system employed at NBTF.

1.1 Thermonuclear Fusion

Access to affordable, abundant energy, mainly from fossil fuel sources, has been a key factor in economic growth since the Industrial Revolution [1]. Nevertheless, the growth in world energy demand from fossil fuels has played an important role in the upward trend in CO_2 emissions: it has been demonstrated that in 2016, the average concentration of CO_2 was about 40% higher than in the mid-1800s, with an average growth of 2 ppm/year in the last decade. The global energy consumption is increasing rapidly and, according to the U.S. Energy Information Administration (EIA), the world energy demand will be 28% higher in 2040 compared to that of 2015 (Figure 1.1). Furthermore, the biggest increase is expected to come from developing countries [2]. As a consequence, the research on renewable sources of energy is nowadays one of the most important scientific topics and goals. To sustain the non-renewable resources and reduce CO_2 emissions, the only available path is to develop new forms of renewable energy production.

Nuclear fusion is a future energy option since it could acquire a significant role in providing sustainable, secure and safe energy to the whole world. As a matter of fact, the nuclear fusion reaction is an inherently safe reaction since there are no possibilities of runaway reactions. Moreover, the fuel used to carry out this reaction has no availability limits, no long-lived radioactive waste is produced and finally, no CO_2 greenhouse gas emissions are released.

1.1.1 Principles of Nuclear Fusion

Fusion is a form of nuclear energy that involves the merging of light elements to create a nucleus of larger mass number.

The nucleus of atoms are constituted by a number of protons (Z) and neutrons (N=A-Z, where A is the atomic number of the element), but the mass of a nucleus is always less than the sum of the single masses of its protons and neutrons. The difference represents the nuclear binding energy, which holds the nucleus together [3].

The binding energy of a nucleus is the energy required to completely disassemble it into separate protons and neutrons. The energy released during a fusion reaction indicates a decrease in the final total nuclear mass. This difference in mass is transformed into energy following the Einstein's equation:

$$E = \Delta m c^2 \qquad \text{Eq. 1.1}$$

All fusion reactions can only occur if the interacting nuclei have a kinetic energy that overcomes the repulsive Coulomb potential energy [3]. The probability that this Coulomb barrier will be overcome and that two light nuclei will undergo a nuclear fusion reaction is defined as cross section s. The reaction rate of a nuclear reaction is the number of reactions

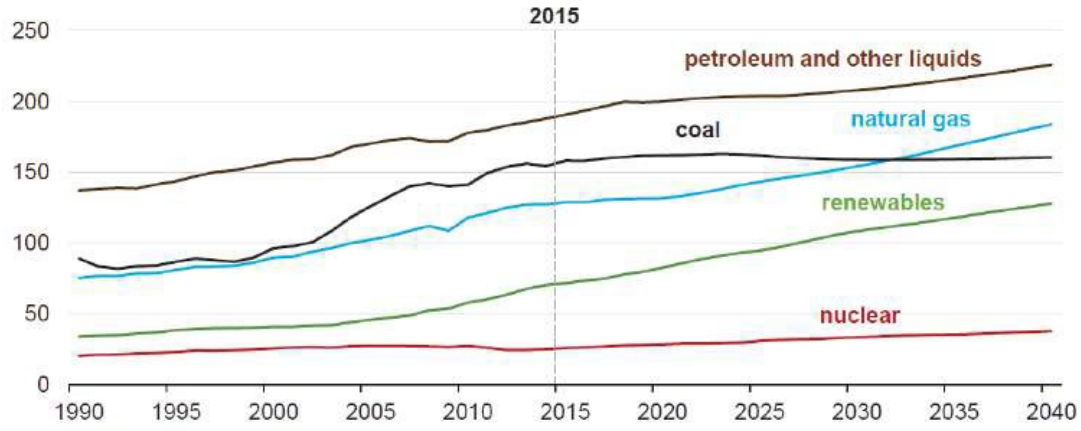

Figure 1.1: World energy consumption by energy source [2]

per unit volume per unit time and is proportional to <σn>. This latter is an average product of σ and n, which is the nuclei relative velocity of the nuclei taking into account the distribution of velocities of the different particles [4]. A candidate reaction for commercial power plant must be exothermic and the cross-section must be high enough at achievable energies. Moreover, the reaction chosen should let the fusion power plant to reach a fusion gain between Q[1]=10 and 50. Some of the considered and studied reactions to achieve controlled thermonuclear fusion under on earth involve the hydrogen isotopes deuterium (D) ${}_1^2H$ and tritium (T) ${}_1^3H$ and are listed below:

1. Deuterium – Deuterium reaction (D - D)

$$ {}_1^2H + {}_1^2H \rightarrow {}_2^3He + {}_0^1n + 3.27MeV \qquad \text{Eq. 1.2} $$

$$ {}_1^2H + {}_1^2H \rightarrow {}_1^3H + {}_1^1H + 4.04MeV \qquad \text{Eq. 1.3} $$

2. Deuterium – Helium reaction (D - ${}_2^3He$)

$$ {}_1^2H + {}_2^3He \rightarrow {}_2^4He + {}_1^1H + 18.3MeV \qquad \text{Eq. 1.4} $$

3. Deuterium – Tritium reaction (D - T)

$$ {}_1^2H + {}_1^3H \rightarrow {}_2^4He + {}_0^1n + 17.59MeV \qquad \text{Eq. 1.5} $$

Figure 1.1 shows reaction the rates variation with temperature for reactions reported in Eq. 1.2, Eq. 1.3, Eq. 1.4 and Eq. 1.5. The D-T reaction (Eq. 1.5) has the highest reactivity at lower temperature. As a matter of fact, it can be carried out at about 150 - 200 million °C whereas the D - D reaction (Eq. 1.2 and Eq. 1.3) requires higher temperatures of 400 - 500 million °C since there is a lower probability that a pair of D - D nuclei will collide [5].

To generate the requisite energy for surpassing the Coulomb barrier, it is essential to subject the reactants to extremely elevated temperatures, causing them to transform into a state known as plasma. A thermonuclear plasma can be defined as a totally ionized gas containing ions and electrons. In a plasma, some electrons are freed from their atoms, allowing current to flow [6].

Considering the deuterium-tritium reaction (Eq. 1.5), which is the most advantageous, the final products are charged alfa particles ${}_2^4He$ and neutrons. The alfa particles can be confined by a magnetic field, as will be better explained in Section 1.3. These particles engage with other charged constituents, such as ions and electrons, within the plasma, serving

[1] The term "Q", in fusion, is the energy gain factor: ratio between the power produced by the fusion reactions and the external power required to sustain them via plasma heating.

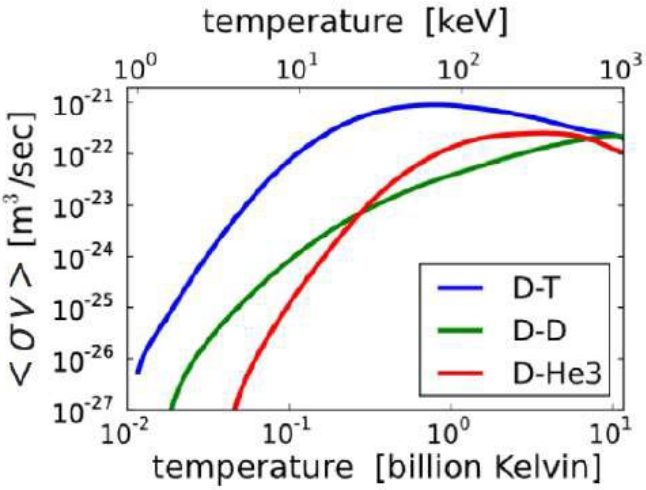

Figure 1.2: Reaction rates of the D - T; D - D and D - ${}^3_2He$ reactions [5].

as a source of heating. In contrast, neutrons cannot be constrained and exit the plasma, impacting the solid walls encircling it and transmitting energy to them [5].

One of the main advantages of fusion is the high natural abundance of inexpensive fuel that has the potential to supply large amounts of energy for thousands of years. As a matter of fact, deuterium, which is one of the reactant, can be distilled from water. By contrast, tritium, the second required fuel, is a fast-decaying radioelement of hydrogen with a short half-life[2] of about 12 years and so does not occur naturally in abundance on earth [4]. To address this challenge, tritium is generated in the surrounding blanket region of the D - T reaction zone and is produced through the fusion reaction involving lithium. Neutrons that escape from the plasma interact with the lithium present in the reactor's blanket, resulting in the production of tritium through the following series of reactions:

$$ {}^6_3Li + {}^1_0n \rightarrow {}^3_1H + {}^4_2He + 4.78MeV \qquad \text{Eq. 1.6} $$

$$ {}^7_3Li + {}^1_0n \rightarrow {}^3_1H + {}^4_2He + {}^1_0n - 2.5MeV \qquad \text{Eq. 1.7} $$

The second reaction (Eq. 1.7) is endothermic, therefore the Li-fuel is enriched by ${}^6_3Li$ to maximize energy output [5].

The conditions that must be achieved by the plasma in order to have a net production of energy are determined by the *Lawson Criterion*. In 1955 John D. Lawson proposed an

[2] Half-life: the amount of time that a given amount of substance takes to half undergo some specified process. For a radioactive substance, is the time required by half of its atoms to decay.

ignition criteria for the Deuterium-Tritium (D - T) plasma in a magnetic fusion device. This criterion is following reported in terms of triple product:

$$nT\tau_E \geq 1.2 \cdot 10^{21} \quad [keVsm^{-3}] \qquad \text{Eq. 1.8}$$

where *n* is the plasma density, *T* is the temperature of the D - T plasma in KeV and τ_E is the plasma confinement time in seconds, which indicates the rate at which the plasma loses energy. In order to produce energy from fusion reactions, a sufficiently hot (*T*) and dense (*n*) plasma must be confined effectively (τ_E) [7].

1.2 The Tokamak Machine

To initiate fusion reactions, specific conditions must be met. In stars, their immense mass generates gravitational forces capable of compressing hydrogen to such high densities and temperatures that they enable the creation of hot and confined plasma, initiating nuclear fusion reactions. On Earth, the gravitational force is insufficient to achieve the desired plasma density. Unlike stars, which rely on gravity, our planet requires higher temperatures to overcome the Coulomb barrier and trigger fusion. Achieving these high temperatures can be accomplished through gas heating techniques, such as circulating a strong current (known as ohmic heating) or introducing high-energy particle beams or radiation (referred to as additional heating).

One method being explored for maintaining the high-temperature plasma necessary for fusion reactions on Earth is magnetic confinement. Over the years, various closed magnetic configurations designed for plasma confinement have been developed and tested, including Tokamak, Stellarators, Z-pinch, and Reversed Field Pinch (RFP).

The Tokamak machine is the most extensively investigated machine, so far. The word "tokamak" is derived from the Russian words, toroidalnaya, kamera and magnitnaya katushka , meaning "toroidal chamber" and "magnetic coil". This reactor takes on the shape of a torus. The direction along this toroidal shape is referred to as the "toroidal direction," while the plane perpendicular to it is known as the "poloidal plane."

The primary function of the magnetic field in a Tokamak is to confine the plasma and prevent it from coming into direct contact with the reactor's first wall. This first wall serves as a protective barrier, shielding the internal structure from direct radiation and particle loads. Beyond the first wall lies the breeding blanket, which serves three essential purposes: first, it extracts heat from the reactor to generate electricity; second, it generates new fuel by producing tritium from lithium; and finally, it acts as a shield for the vacuum vessel. (Figure 1.3a).

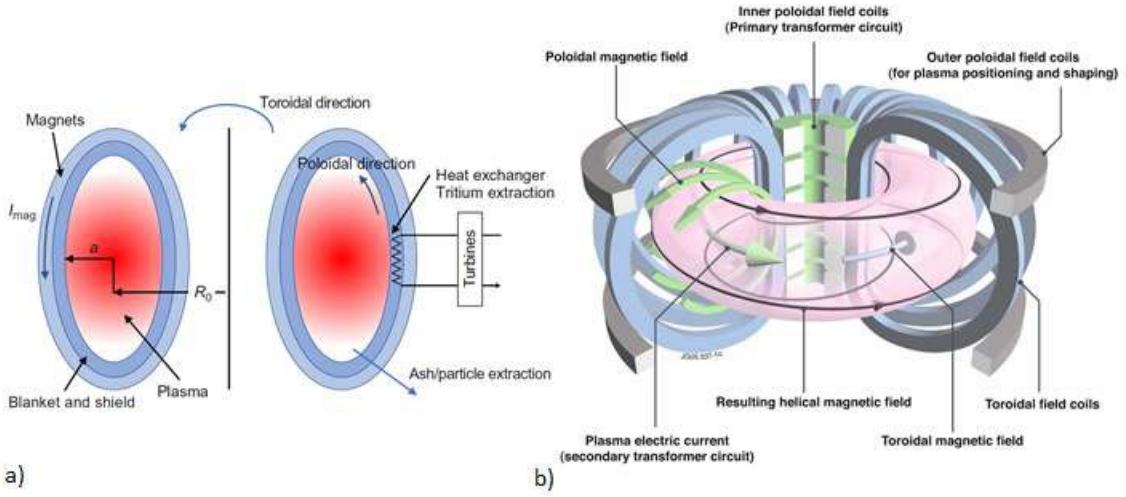

Figure 1.3: a)Section of a Tokamak showing the plasma, blanket, shield, magnets and power extraction; b) Diagram illustrating the tokamak principle: arrangement of magnetic field coils and the resulting magnetic field that confines the plasma [4].

Any tokamak has a set of external poloidal-field coils, including the primary transformer and additional control coils, concentric with the toroidal vacuum vessel. Furthermore, a series of coils, placed all around the torus, generates a toroidal magnetic field B_T. The magnetically confined plasma inside the chamber acts as the secondary winding of a transformer. Plasma is ohmically heated by the current I_P produced in the primary. This current also induces a poloidal field B_P. The combination of the toroidal B_T and poloidal fields B_P give rise to magnetic field lines which have helical trajectory around the torus [8]. A tokamak geometry can be generically defined by its major radius R_0, minor radius a, the toroidal field B_T and the plasma current I_P. A schematic representation of a tokamak is reported in Figure 1.3b.

The balance of a fusion reactor is given by:

$$\frac{\partial W}{\partial t} = P_R + P_H - P_L \qquad \text{Eq. 1.9}$$

where W is the plasma energy density ($W \sim 3nT$ by assuming equals the ion and the electron density and temperature), P_R is the power per unit volume produced by the fusion reactions, P_H the auxiliary heating per unit volume and P_L the power loss per unit volume.

The largest Tokamak is the Joint European Torus (JET) built in Culham, close to Oxford, in the early '80s. Currently, 35 nations are collaborating to build the world's largest tokamak, ITER, a magnetic fusion device that has been designed to prove the feasibility of fusion as a large-scale and carbon-free source of energy. ITER ("The Way" in Latin) is one of the most ambitious energy projects in the world today and is going to be build next to Cadarache in Saint-Paullès-Durance, in Provence, southern France.

1.2.1 ITER

TER represents a significant step forward in the pursuit of a controlled thermonuclear fusion reactor. Located in southern France, this ambitious project involves collaboration among 35 nations to construct the world's largest tokamak. ITER aims to accomplish several crucial milestones essential for the development of a fusion power plant. These include achieving robust burning plasma[3] regimes, testing conventional physics solutions for power exhaust, and validating breeding blanket concepts.

The design goal for ITER is to generate 500 MW of fusion power, equivalent to the capacity of a medium-sized power plant. With an injected power of 50 MW, this results in a fusion gain, denoted as Q=10. ITER will also demonstrate the main technologies for a fusion power plant. The main technical data and parameters of the ITER experiment are listed in Table 1.1 [9].

Table 1.1: Main ITER parameters

Total fusion power	500 MW
Amplification factor Q	~10
Plasma inductive burn time	≥400 s
Plasma major radius (R0)	6.2 m
Plasma minor radius (r)	2.0 m
Plasma current (Ip)	15 MA
Safety factor (q)	3
Toroidal magnetic field (B)	5.3 T
Electron density (ne)	$1020 m^{-3}$
Plasma total external heating	~ 50 MW
Neutral Beam Injector	33 MW
Plasma type	deuterium-tritium
Plasma volume	840 m

ITER would offer the possibility of studying several reactor relevant scientific and technological issues, which are beyond the present experimental capabilities. The principal aims of ITER are:

1. Achieve a deuterium-tritium plasma in which the fusion conditions are sustained mostly by internal fusion heating. ITER wants to reach the fusion of 0.5 g of deuterium/tritium mixture in its approximately 840 m^3 reactor

[3] Burning plasma: plasmas in which the energy of the helium nuclei produced by the fusion reactions is enough to maintain the temperature of the plasma, thereby reducing or eliminating the need for external heating

chamber and demonstrate steady state operation using non-inductive current drive. ITER's goal is to efficiently confine the plasma in a manner where the self-heating effect becomes the dominant source of heating, surpassing any other external heating methods;

2. Generate 500 MW of fusion power in its plasma. ITER is designed to reach $Q_{fus}/Q_{aux} \geq 10$. where Q_{fus} is the the energy gain by fusion and Q_{aux} the energy needed by auxiliary systems to heat the plasma. This achievement must be demonstrated under various operating scenarios, ensuring that the nominal fusion power output of around 500 MW can be sustained for an extended duration of approximately 400 seconds. This extended timeframe is necessary to reach and maintain stationary conditions, confirming the feasibility of ITER's fusion power generation capabilities;

3. Contribute to the demonstration of the integrated operation of technologies for a fusion power plant. ITER will allow scientists to study plasmas under conditions similar to those expected in a future power plant and to test innovative technologies;

4. Test tritium breeding: for the first time, tritium will be produced within the vacuum vessel;

5. Demonstrate the safety characteristics of a fusion device. ITER operation will demonstrate the control of the plasma and the fusion reactions with negligible consequences to the environment.

A cutaway of ITER is shown in Figure 1.4 with the indication of the main components. Starting from the outermost layer, the stainless steel cryostat, measuring about 29 meters by 29 meters, serves multiple crucial functions. It creates a vacuum and cold environment, enveloping the vacuum vessel and the superconducting magnets. Additionally, it acts as a protective shield, safeguarding the reactor from external damage.

Inside this cryostat, ten thousand tons of superconducting magnets play a pivotal role in generating magnetic fields that initiate, confine, shape, and control the plasma. The stainless steel vacuum vessel serves a dual purpose: maintaining a vacuum environment and serving as the primary safety containment barrier.

Further inward, the blanket plays a vital role by shielding the inner part of the steel vacuum vessel and external components from the intense heat and high-energy neutron fluxes generated during the fusion reactions.

On the lower side of the vacuum vessel, the divertor assumes a critical role. It must withstand the highest heat flux within the machine and manage the discharge of waste gases and impurities from the reactor.

To support the fusion process, three auxiliary heating systems are employed: neutral beam injectors, ion cyclotron antennae, and electron cyclotron antennae. These systems collectively provide a maximum total power of 73 MW, with 33 MW delivered by neutral beam injectors (wo neutral beam injectors, each capable of delivering a 16.5 MW deuterium beam with particle energies of 1 MeV, are currently planned for ITER), 20 MW from the ion cyclotron antenna, and an additional 20 MW from the electron cyclotron antenna [10].

1.3 Neutral Beam Injection

In order to have sufficient fusion processes occurring, the confined plasma must be bring to extremely high temperature, T ≃10 keV. There are three main way to heat the plasma:

1. **Ohmic heating**: in a Tokamak reactor, the generation of the poloidal field is achieved by utilizing the plasma itself as a conductor and directing a

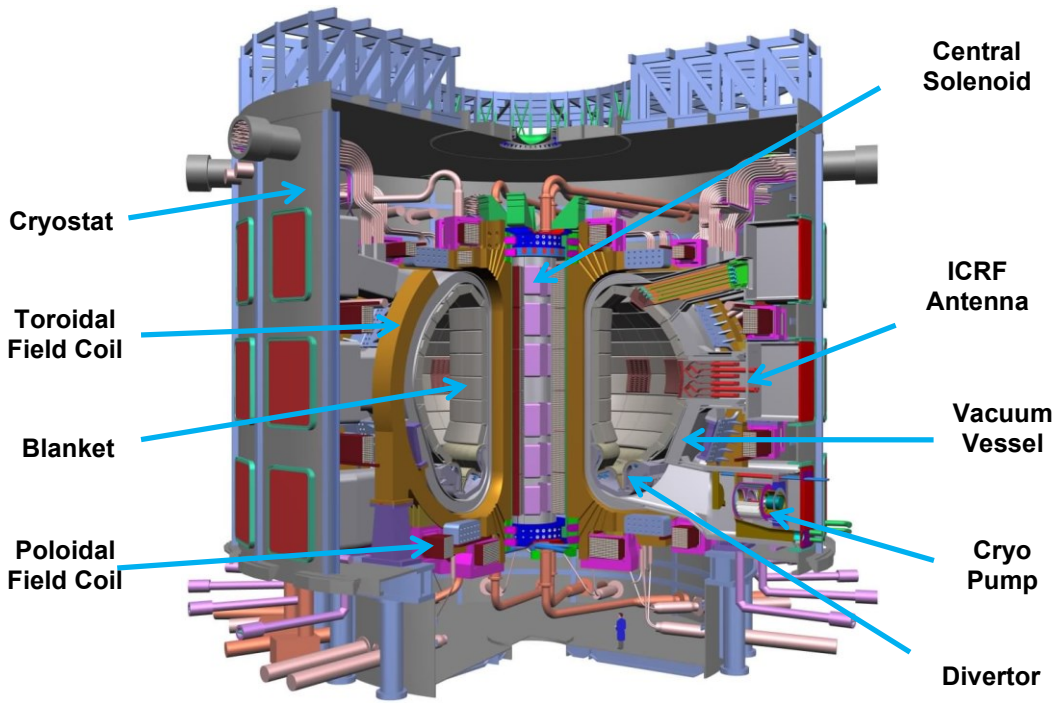

Figure 1.4: 3D cutaway model of ITER

substantial current through it. This current flow results in the creation of a corresponding magnetic field in the poloidal direction. This plasma current will additionally heat the plasma by ohmic heating, according to $P_{Ohm} = \eta j^2$, where η is the resistivity and j the current density. Nonetheless, it's important to note that plasma resistivity decreases as temperature rises ($\eta \propto T^{-\frac{3}{2}}$). This decrease in resistivity limits the efficiency of ohmic heating, which alone can only achieve a maximum plasma temperature of approximately 3 keV under typical reactor conditions. To achieve higher temperatures, auxiliary heating systems are required to bridge this temperature gap.

2. **Radiofrequency heating**: the first auxiliary heating system involves radiating electromagnetic waves into the plasma. By carefully selecting the frequency of the generator to match a characteristic frequency of the plasma, the electromagnetic power radiated into the plasma is absorbed by the charged particles. These energized particles subsequently collide with other plasma particles, effectively raising the overall temperature of the plasma.
3. **Neutral Beam Injection (NBI)**: this method relies on injecting high-energy neutral particles into the plasma. Once inside, these neutral particles become ionized and, as part of the thermalization process, transfer their energy to the plasma, raising its temperature. Importantly, the injected particles must initially be neutral to effectively penetrate the magnetic fields before entering the plasma..

Considering where this work of thesis was carried out, NBI will be described a little more in details.

A NB injector comprises four main components: an ion source, an electrostatic accelerator, a neutralizer, and a residual ion dump. A calorimeter can be inserted for diagnostic purposes. The process of injecting neutrals into the plasma involves the following steps:

1. **Ion generation**: in order to inject neutrals into the plasma, NBI systems can generate positive or negative ions within an ion source;
2. **Ion acceleration**: the generated ions are then accelerated through the ion beam using a strong electric field created by different grids within an electrostatic accelerator;
3. **Neutralization**: ions are neutralized in charge exchange processes with a neutral gas stripper. This process takes place inside a component called Neutralizer and Electron Dump (NED);

4. **Ion filtering**: following neutralization, the neutral beam is filtered to remove any ions that did not undergo complete neutralization. This filtration process is achieved by applying a strong magnetic field within a component known as an Electrostatic Residual Ion dump (ERID);
5. **Plasma interaction**: once the neutral beam is appropriately neutralized and filtered, it is directed toward the tokamak chamber. As the neutral particles enter the plasma, they rapidly ionize due to the high temperatures and become trapped by the magnetic field of the device, contributing to the plasma heating.

It's important to note that the ions created in the ion source can be either positively or negatively charged. While most existing NB systems accelerate positive ions, ITER, in particular, requires high-energy beams, which can only be produced using negative ion sources, as depicted in Figure 1.5 [11].

Indeed, ITER, with its substantial plasma volume, necessitates the use of particles that can travel at sufficiently high speeds to penetrate deep into the plasma. The deposition of beam power needs to occur within the region known as the *H-mode* barrier, which is typically located between $0.9 < r/a < 1$, where r is the distance from the plasma centre and a is the minor radius of the plasma. In the case of ITER, this implies that the ions in the neutral beams must possess energies exceeding 300 keV, which qualifies as high energy.

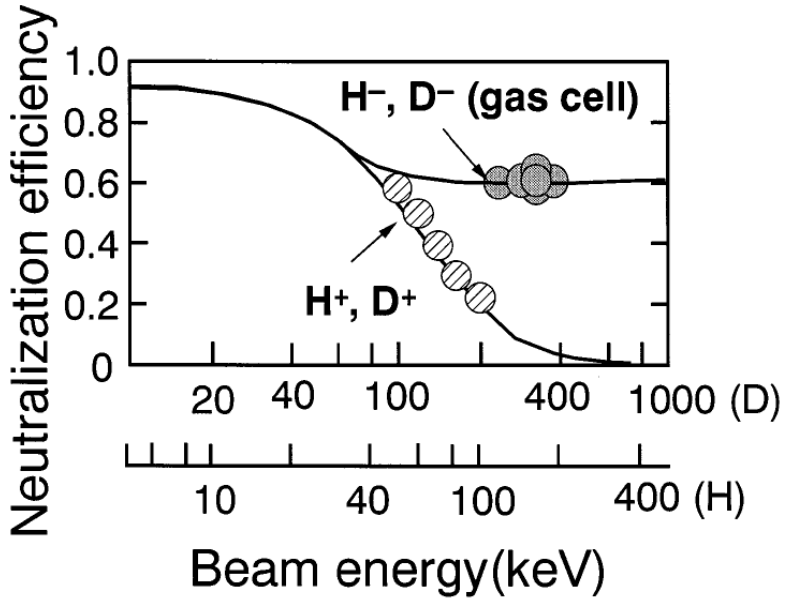

Figure 1.5: Hydrogen ions neutralisation efficiency as a function of energy, measured in the NBIs at JT-60U, adapted from [11]

ITER will use two NBIs to inject 33 MW of either 1 MeV deuterium (D) or 870 keV Hydrogen (H) into the plasma. A third heating beam may be added later. A different neutral beam will be used for diagnostic purposes (DNB).

1.4 PRIMA Test Facility

Within the framework of research and development activities planned by the ITER Organization for Neutral Beam Injectors (NBIs), a test facility called PRIMA (Padova Research on ITER Megavolt Accelerator) was established at the Consorzio RFX in Padova. PRIMA encompasses two distinct experiments:

1. **SPIDER (Source for Productions of Ions of Deuterium Extracted from a Radio-frequency plasma)**: it is the full-size negative ion source with low voltage extraction of 100 keV;
2. **MITICA (Megavolt ITER Injector and Concept Advancement)**: it is the full scale prototype for the ITER heating neutral beam injector operating at full beam power with voltages of up to 1 MV.

The project insists on an area of 17500 m^2 and the floors covered by the building are approximately 7000 m^2 (Figure 1.6). The SPIDER and MITICA facilities are situated in the primary room referred to as "Building 1". The auxiliary systems, including those for cooling, cryogenics, and vacuum, are housed in "Building 2". Building 6 is dedicated to housing the electric power supplies (PS), transformers, switchboards, and diagnostic and control systems

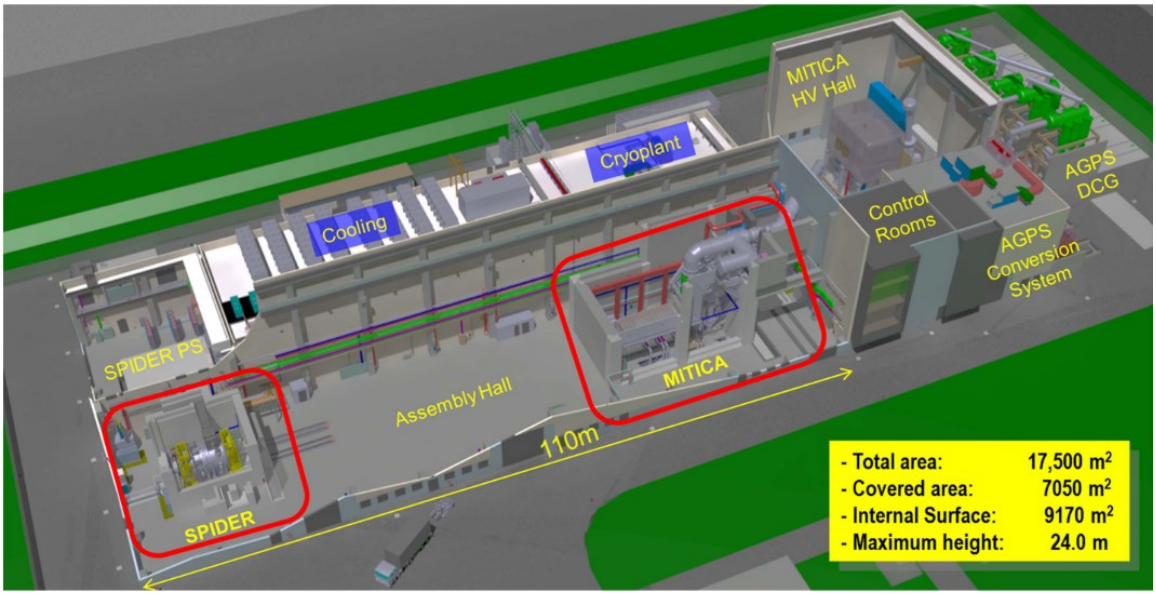

Figure 1.6: 3D-CADview of the PRIMA facility [12]

specifically designed for SPIDER (referred to as SPIDER PS in Figure 1.6). The MITICA High Voltage (HV) Hall features the -1 MV shielded deck, which accommodates the power supply systems for MITICA. Additional electric supply systems for MITICA, operating at reduced voltage, are located in the "AGPS Conversion System". In the external area there are the MITICA acceleration grid power supply (AGPS DCG) (five transformers from -200 to -1000 kV), the underground -1 MV transmission line, and two underground water basins for the cooling plant.

1.4.1 SPIDER

SPIDER serves as the full-scale test-bed for the negative ion source of ITER Neutral NBIs. Its primary purpose is to evaluate and optimize the performance of the ion sources designed for ITER. SPIDER is designed to extract and accelerate both H^- and D^- ions up to 100 keV with a maximum extraction current density of 355 A/m² for hydrogen and 285 A/m² for deuterium. It operates with a beam source filling pressure of 0.3 Pa and has a pulse length of 3600 s[13], [14]. An overview of the device is given in Figure 1.7.

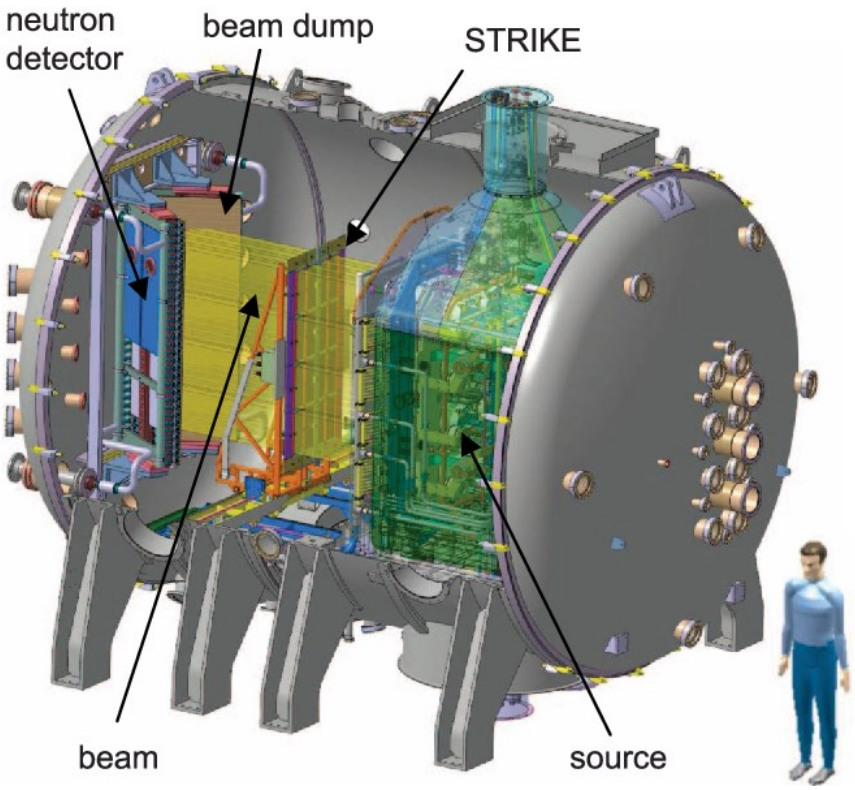

Figure 1.7: Overview of SPIDER experiment

Negative ions are generated in an inductively coupled plasma produced by 8 coils powered in pairs by 4 radiofrequency (RF) generators providing up to 200 kW each. The SPIDER extraction and acceleration system is composed of three grids: the Plasma Grid (PG), Extraction Grid (EG) and Grounded Grid (GG) plus a Bias Plate (BP) (Figure 1.8). The BP, placed upstream of the PG, reduces the co-extracted electron current. Each grid features 1280 apertures, through which the ion beamlets are extracted from the ion source and accelerated up to 100 keV energy. The EG is biased at 10 kV with respect to the PG. The grounded grid (GG), further downstream, will provide the ions with the last acceleration step of 90 kV. The PG, directly facing the plasma is required to operate at a temperature of about 150 °C in order to enhance the caesium effect for negative ion surface generation. All the grids are constructed by electro-deposition of pure copper onto a copper base plate. The BP and PG are covered by a molybdenum layer, a refractory metal with a low sputtering yield [15], [16], of about 100 μm thickness to prevent copper sputtering due to the impact of the plasma.

SPIDER commenced its operations in 2018, and over the course of more than three years, it has been a valuable testing platform. However, in December 2021, a major shutdown was initiated to address several issues and implement improvements and modifications. These included concerns related to excessive gas pressure in the vessel, challenges with RF-

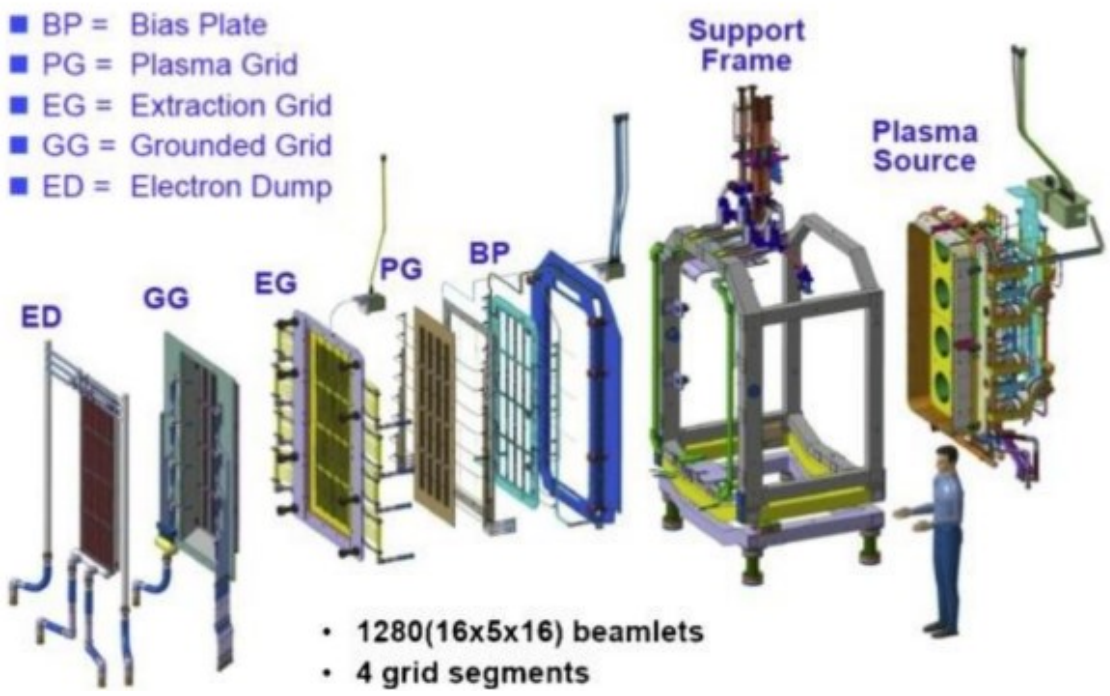

Figure 1.8: Exploded view of SPIDER Beam Source

plasma coupling, the identification of a vacuum leak in one segment of the grounded grid, and an incorrect orientation of the magnets within the grounded grid.

Following this significant shutdown period, the plan is for SPIDER to resume its experiments at the end of 2023. The objective is to continue its activities without the previously known limitations, with operations aimed at achieving the expected nominal performances as outlined in the general plan for the development of ITER NBIs. These improvements and adjustments are crucial for ensuring SPIDER's effectiveness as a test-bed for ITER NBIs [14], [17].

1.4.2 MITICA

MITICA is the full scale prototype for the ITER heating neutral beam injector. MITICA will take direct advantage of the R&D and design optimization carried out for the SPIDER full-size ion source. The primary focus of MITICA's work is centred on the 1 MeV beam.

The composition of the ions source and the accelerator is called Beam Source (BS). The other beamline components are: the neutralizer electron dump (NED) the Electrostatic Residual Ion Dump (ERID) and the Calorimeter (Figure 1.9), as listed in Section 1.3.

The Beam Source is composed of an RF negative ion source, closely resembling the one used in SPIDER, for generating negative ions. It also features a five-step electrostatic accelerator with multi-aperture grids (MAMuG) for accelerating the negative ions. The ion source is held at –1 MV. The negative ions generated in the plasma source are extracted across the gap between the PG and the EG, and accelerated toward the GG across five 200 kV acceleration steps defined by the potential of four intermediate acceleration grids (AG1 to AG4, from−800 kV to−200 kV), thus producing a negative ion beam of 46 A H^- (or a 40 A D^-).

The NED has four vertical beam channels where the collision of negative ions with a cloud of hydrogen/deuterium gas results in the formation of neutral particles, positive ions, and negative ions through processes like electron stripping, double stripping, and re-ionization. The deposited power on the neutralizer to be removed is about 5MW.

The ERID comprises five vertical dump walls with four channels crossed by the particle beam. Inside the channels, an electric field deflects the partially positive and partially negative residual ions. The deposited power on the ERID is up to 19MW.

The last component is the Calorimeter, constituted by two panels in a V shape, onto which the neutral beam impinges. The here deposited power is 18MW [12]

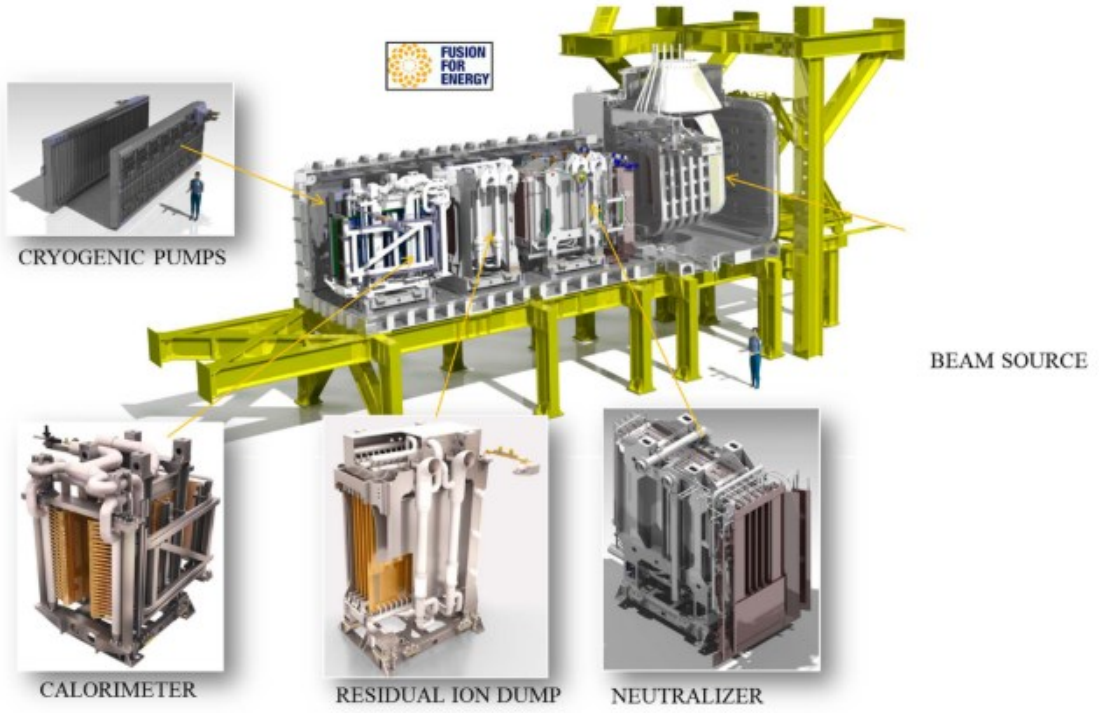

Figure 1.9: View of the MITICA injector with in-vessel components

As of the current status, several critical components of MITICA have been installed, including the vessel, the cooling plant, the gas and vacuum system, and the cryogenic plant. However, the in-vessel components, which encompass the ion source/accelerator and the beamline components, are still under construction. [14], [17].

1.4.3 Primary Confinement for Tritium and Activated Corrosion Products

Nuclear reactors are designed with a multi-loop flow and heat transfer arrangement to establish protective barriers for the confinement of radioactive materials. In the case of magnetic confinement fusion, the hot fuel is encircled by a breeder blanket that contains lithium along with a neutron multiplier like beryllium or lead. The nuclear energy is converted into heat within the blanket and subsequently removed by a coolant.

The steam produced in the steam generator is then conveyed by the secondary system to the main turbine generator, where it is transformed into electrical power. The primary purpose of the primary system, also known as the reactor coolant system, is to transfer the heat from the fuel or blanket to the steam generators. Additionally, the primary system serves a secondary role of containing any nuclear byproducts. A diagram illustrating the primary and secondary heat transfer systems for a fusion reactor is included below in Figure 1.10.

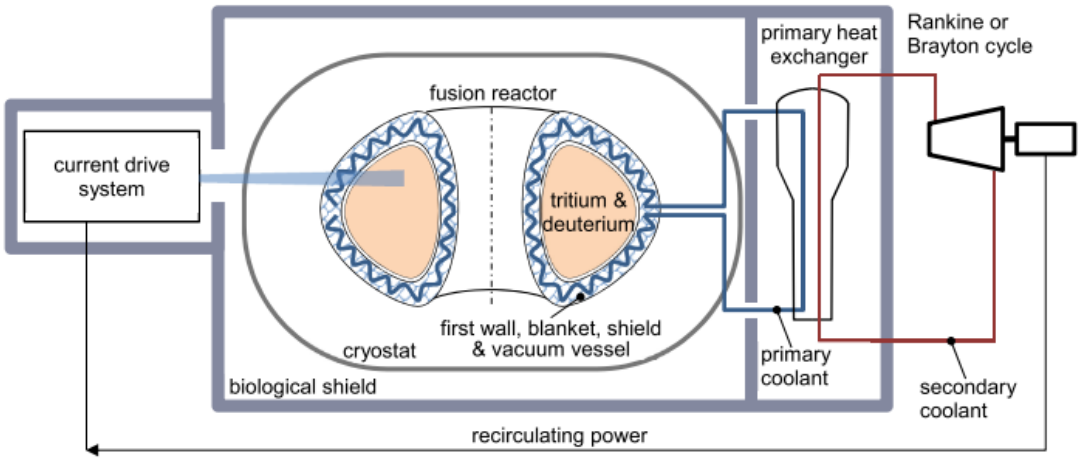

Figure 1.10: Schematic of the primary and secondary heat transfer systems in a possible tokamak fusion power plant

In a Pressurized Water Reactor (PWR), similar to other nuclear reactors, it is essential for both the reactor and the primary heat exchanger to be enclosed within a biological shield. This precaution is necessary because the reactor emits a significant number of neutrons, and the coolant carries activation products as well as tritium. The primary coolant plays a crucial role in extracting heat from various components, each subjected to varying power densities and levels of radiation. Starting from the plasma and moving outward, these components include the "first wall" (the surface facing the plasma), the blanket, the radiation shield (which provides protection for the vacuum vessel), and the vacuum vessel itself. Furthermore, a structure called a divertor is required to capture ions that escape from the plasma. Most of the research and focus have been on indirect cycles that involve both primary and secondary coolants, primarily due to the high tritium concentration expected in the primary coolant.

1.4.4 NBTF Cooling Plant

PRIMA facility hosts also the cooling plant (Figure 1.11) designed to thermally control by remove heat loads generated during beam operations from both SPIDER and MITICA and characterized by over 5.5 km tubes. The total power to be removed by the Cooling Plant (CP) from both the experiments and the auxiliary systems is up to 70MW, specifically 11.1 MW for SPIDER and 58.4 MW for MITICA.

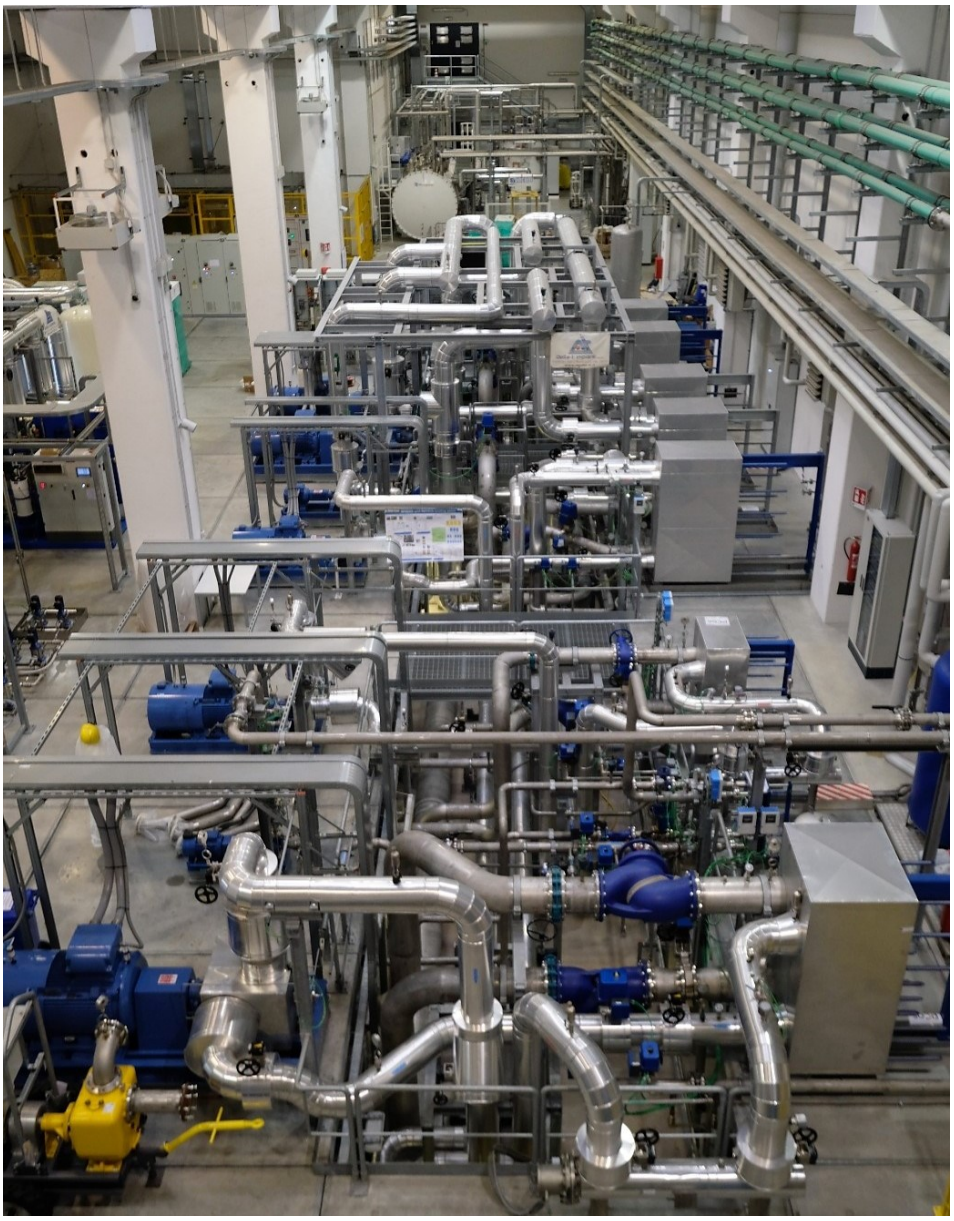

Figure 1.11: Photo of the PRIMA cooling plant

The cooling plant [18] is characterized by three main heat transfer systems (Figure 1.12):

- **Primary Circuits (PCs),** directly connected to the test facilities to remove the experiments' thermal power. Each primary circuit is a closed hydraulic loop with one heat exchanger, a pump, a pressurizer, valves and other instruments;

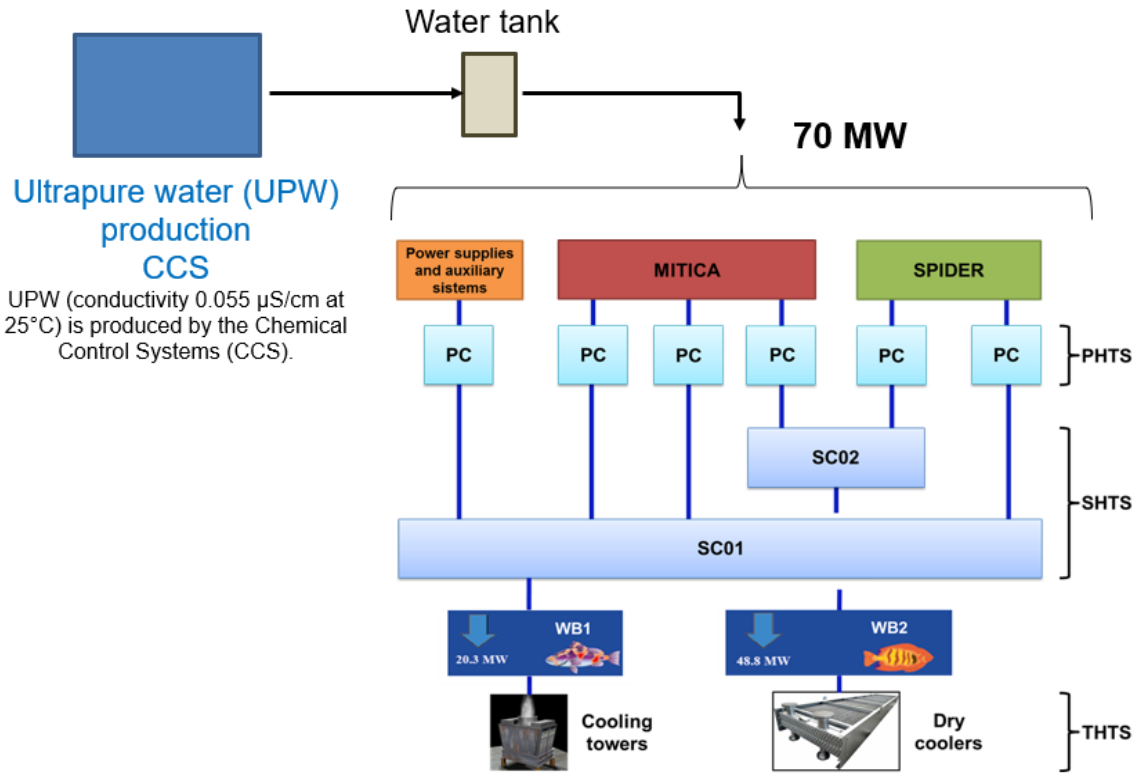

Figure 1.12: Sketch of the PRIMA cooling plant

- **Secondary Circuits (SCs),** aiming to transfer the absorbed heat from PCs to two different Water Basins (WBs), used to store the thermal energy;
- **Tertiary Circuits (TCs),** open circuits that transfer the thermal power from the basins to the environment via cooling towers and air coolers.

The cooling plant has been designed to accommodate varying heat loads while maintaining a constant inlet temperature of the coolant. This level of control is achieved through the implementation of variable-speed pumps and two-way valves to regulate flow rates.

As mentioned before, two water basins (WB) are present in the cooling plant to store large amount of thermal energy. WB1 has a capacity of 315 m^3 and it is connected to cooling towers, while WB2 can hold up to 545 m^3 and it is connected to air coolers. These basins play a crucial role in significantly reducing the required active power for heat rejection. Specifically, they contribute to a reduction from 6 MW in cooling tower power and 17 MW in air cooler power, as compared to the total thermal loads of 70 MW, which encompass 11 MW from SPIDER and 58.4 MW from MITICA [18].

The cooling plant has been designed taking in account two different operative scenarios[18]:

1. **ITER-like Scenario**: in this scenario, designed to test the full performance of the Neutral Beam Injector (NBI), two long pulses of 3600 seconds are foreseen. During these pulses, only MITICA is in operation, and it operates at its maximum power (as illustrated in Figure 1.13a);
2. **Standard Experimental Scenario**: in this scenario, both MITICA and SPIDER operate in parallel, and the experimental setup involves ten pulses of 300 seconds each throughout the entire day (as depicted in Figure 1.13b)

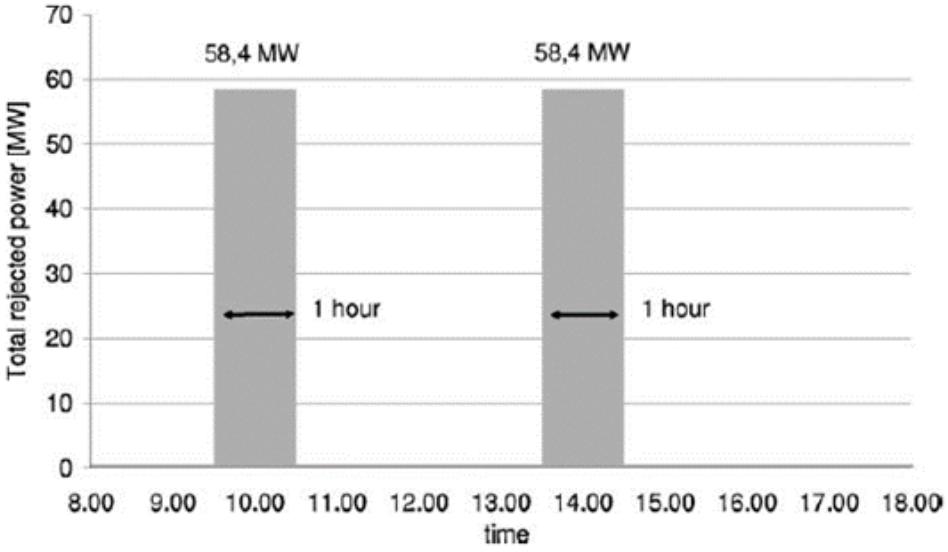

a)

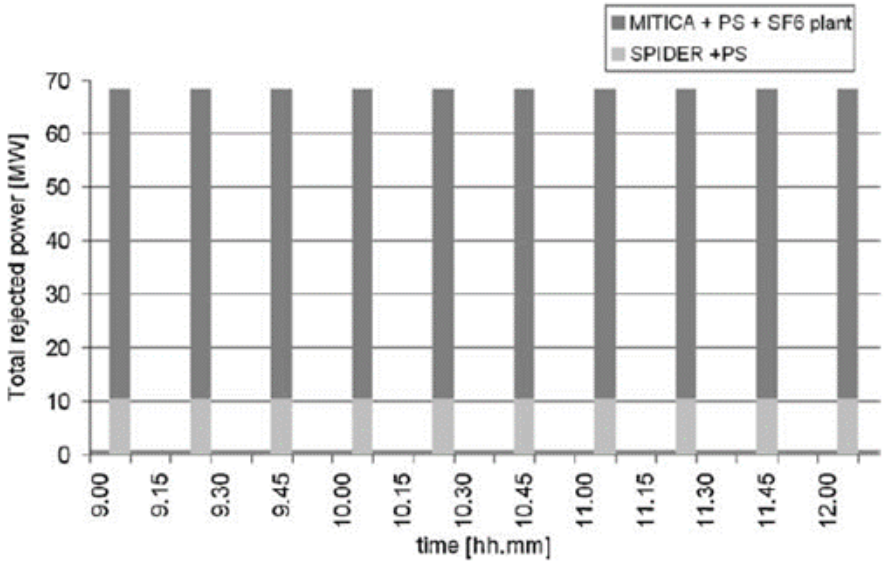

b)

Figure 1.13: a) MITICA full power long pulses; b) SPIDER and MITICA simultaneous operations

1.4.5 Water Quality in NBTF Cooling Plant

Ultrapure water (UPW) is used as coolant in NBTF PCs (Table 1.2) to allow electrical insulation of in-vessel components posed at different voltage levels by limiting the leakage current. The ultrapure water is produced by a dedicated system named Chemical Control System (CCS) that supplies two types of water at different grades:

1. **W-I**, with resistivity of 5.0 - 10 MΩ·cm at 25 °C;
2. **DW**, with resistivity of 0.05 – 0.1 MΩ·cm at 25 °C.

These water quality levels are obtained after pre-chlorination, ultrafiltration, softening, dichlorination, microfiltration, reverse osmosis, oxygen stripping and electro-deionization steps.

Two more types of water can be produced by mixing the abovementioned waters:

3. **W-II**, with resistivity of 1.0 - 2.0 MΩ·cm at 25 °C, obtained by mixing 96% W-I and 4% DW;
4. **W-III,** with resistivity of 3.3 - 5 MΩ·cm at 25 °C, obtained by mixing 99% W-I and 1 % DW.

Currently, only W-I water type is produced by the CCS and stored in tanks (Figure 1.14).

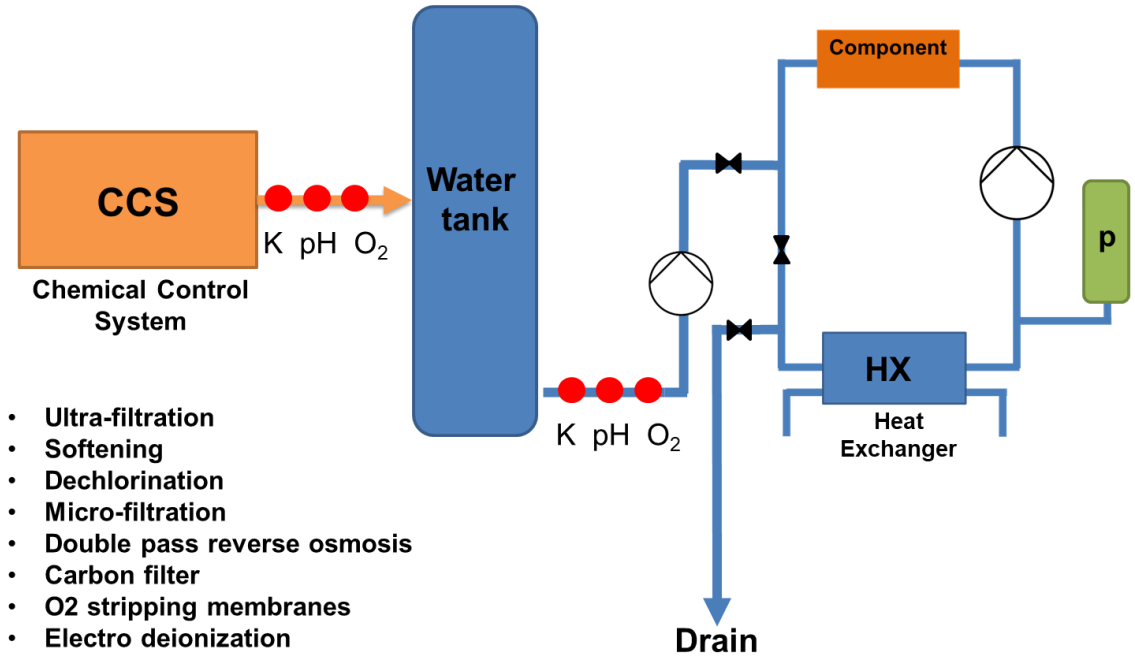

Figure 1.14: Sketch of CCS, tank storage, sensors in NBTF cooling system

The water named W-I to be used as coolant in SPIDER and MITICA primary circuits should have the following characteristics:

- Resistivity: 5 ÷ 10 MΩ · cm at 25°C;
- Conductivity: 0.2 ÷ 0.1 μS/cm;
- pH: 6.5 ÷ 7.5;
- Dissolved oxygen: < 50 ppb (parts per billion).

When comparing the specifications for NBTF water W-I with the standards outlined in ASTM D-1193 - 99[19] for Type I water, it becomes evident that the maximum allowable conductivity values specified for NBTF water W-I are more in line with the specifications for Type III ASTM water (see Table 1.2).

ASTM D-1193 - 99 specifies that Type I water has a maximum allowable conductivity of 0.0555 μS/cm at 25 °C, which corresponds to the conductivity of what is commonly referred to as ultrapure water (UPW) [20]–[22]. In this thesis, we will use the term "UPW" to describe water of this quality. ASTM [2]. For Type III water according to ASTM standards, the maximum allowable conductivity is 0.25 μS/cm, while for Type II water, it is 1 μS/cm at 25 °C. These conductivity values align with the requirements for the Type W—II and W-III needed in SPIDER and MITICA PCs.

Another difference between ASTM water specifications and PCs cooling water specifications are the contaminants admissible contents. No maximum admissible values for

Table 1.2: Comparison between ASTM water [19] and NBTF cooling water

Type water	Conductivity (μS/cm) maximum	Resistivity (MΩ cm) minimum	pH (μg/L)	TOC (μg/L)	Sodium (μg/L) max	Chloride (μg/L) max	Total silica (μg/L)	Dissolved O_2 max (ppb)
SPIDER water								
W-I	0.1 – 0.2	5-10	6.5-7.5	N.A.	N.A.	N.A.	N.A.	50
W-II	0.5 - 1	1-2	6.5-7.5	N.A.	N.A.	N.A.	N.A.	50
W-III	0.2 – 0.3	3.3-5	6.5-7.5	N.A.	N.A.	N.A.	N.A.	50
ASTM water								
I	0.0555	18	-	50	1	1	3	N.A.
II	1	1	-	50	5	5	3	N.A.
III	0.25	4	-	200	10	10	500	N.A.

total organic carbon (TOC), sodium, chloride or total silica are specified for SPIDER and MITICA cooling water.

NBTF cooling water specifications specify a neutral pH (between 6.5 and 7.5) and maximum 50 ppb of dissolved oxygen.

To ensure that the water generated by CCS-1 complies the rigorous specifications established for NBTF power converters, the cooling plant incorporates in-line sensors. These sensors, including conductivity (k), pH (pH), and dissolved oxygen (O_2) sensors, are strategically placed in various locations. They are positioned immediately after the water production site within the CCS-1 skid, following the electrodeionization module, which represents the final step in water purification, and after the pressurized tanks designed for storing water used to refill primary circuits (as illustrated in Figure 1.14). In the primary water circuits of SPIDER and MITICA, there are no O_2 or pH sensors installed. Instead, the water quality is monitored and controlled solely based on its conductivity. Conductivity sensors are incorporated into each PCs of both SPIDER and MITICA for this purpose.

With respect to NBTF, ITER will be distinguished by its tokamak cooling water system (TCWS). This system is engineered to extract up to 1 GW of thermal power from various components, including the vacuum vessel (VV), in-vacuum vessel components, and NBIs. Additionally, the TCWS incorporates the Chemical and Volume Control System (CVCS) to manage water chemistry and adjust water volume in response to temperature fluctuations. The CVCS continuously monitors water quality online to safeguard the piping system against corrosion and erosion [23]. In the NBTF, the CCS exclusively produces ultrapure water, and the water volume is regulated through online pressurizers. As previously mentioned, there are currently no online pH and O_2 sensors or resins in place for monitoring and regulating water quality. The quality of the water is solely assessed based on the conductivity parameter.

When water achieves the maximum allowable value of conductivity in PCs, the circuits must be stopped to allow a complete (or partial) replacement of the coolant. The conductivity requirements for W-II and W-III waters are obtained by partial refilling the degraded water of cooling circuits with W-I water; pH or dissolved oxygen of the water in the circuits are not verified. Since the water re-filling takes place through this offline system, it is essential to minimize the conductivity degradation as much as possible in order to maximize the experimental time.

1.4.6 Thermo-Hydraulic Requirements for SPIDER and MITICA PCs

SPIDER components are actively cooled by four Primary Circuits (PCs). Currently, only the first three (PC01, PC02 and PC03) are working, whereas the fourth one (PC04), which is designed to cool the Beam Dump, is going to be connected and exploited in the next months.

MITICA components are cooled down by six PCs. Each PC cools down a different and specific component as shown in Table 1.3 and Table 1.4. In this latter are also shown the required water mass flow rate, inlet temperature and pressure at the nominal rejected power.

Table 1.3: Thermo-hydraulic requirements for SPIDER components

	Components	Max rejected power [kW]	Mass flow rate [kg/s]	T_{in} [°C] (±2°C)	ΔP at max flow [kPa]	Volume [m^3]	Fluid	Raw materials
PC01	HVD (ISEPS + TL)*	615	18.8 (ISEPS 18.5; TL 0.3)	20 - 35	700	1.1	W	SS + Cu + PP
	AGPS	100	3	20 - 35	700			
	Total	715	21.8					
PC02	RF Coils	25	0.5	20 - 45	680	3.7	W-II	SS + Cu
	Extraction Grid	1000	11 (4 pipes x 2.75)	20 - 45	700			
	Grounded Grid	700	8.0 (4 pipes x 2.0)	20 - 45	700			
	Electron Dump	1000	31	20 - 45	400			
	Total	2725	50.5					
PC03	Faraday Shield Lateral Wall 1	240	2.5	35 - 45	300	1.7	W-II	SS + Cu + CuCrZr
	Faraday Shield Lateral Wall 2	240	2.5	35 - 45	300			
	Faraday Shield Back Plates	73	2	35 - 45	250			
	Driver Plates	160	3	35 - 45	700			
	Source Case Lateral Wall	100	2	35 - 45	700			
	Bias Plate	10 + 40 (+)	0.125	35 - 150	50			
	Plasma Grid	20 + 80 (+)	0.125 (4 pipes * 0.031)	35 - 150	200			
	Total	963	12.25					
PC04	Beam Dump	6100	64	20 - 55	150	4.4	W-II	SS + CuCrZr
	Total	6100	64					

Table 1.4: Thermo-hydraulic requirements for MITICA components

	Components	Max rejected power [kW]	Mass flow rate [kg/s]	T_{in} [°C] (±2°C)	ΔP at max flow [kPa]	Volume [m^3]	Fluid	Raw materials
PC05	Grid 1 MAMuG (-800 kV)	2000	19.5	25÷45	1000 - 1400	12.1	W-I	SS + Cu
	Grid 2 MAMuG (-600 kV)	2000	19.5	25÷45	1000 – 1400			
	Grid 3 MAMuG (-400 kV)	2000	19.5	25÷45	1000 – 1400			
	Grid 4 MAMuG (-200 kV)	2000	19.5	25÷45	1000 – 1400			
	Grounded grid + frame)	2000	19.5	25÷45	900-1200			
	Total	10000	97.5					
PC06	RF Coils, Faraday Shields Source Case, Extraction Grid	2595	33	35÷45	600 – 800	4.1	W-I	SS + Cu + CuCrZr
	Plasma Grid, Bias Plate	30 + 120 (+)	0.25	35÷150	200 - 300			
	Total	2745	33.25					
PC07	Neutraliser, Electron Dump	6000	80	20÷55	240	17.9	W-II	SS + Cu + CuCrZr
	ERID	17200	100	20÷55	600			
	Calorimeter	19460	100	20÷55	600			
	Total	42660	280					
PC08	AGPS	200	8.0	20÷35	600	5.6	W-III	SS, Cu, plastics
	ISEPS	600	18.3	20÷35	600			
Total		800	26.3					
PC09	AGPS	1200	29.3	20÷35	600	Not estimated	W-II	SS, Cu
	GRPS	60	1.8	20÷35	600			
	Total	1260	31.1					
PC10	SF6 plant (9 heat exch.)	230	7.7	20÷35	600	3	DW	SS, Cu
	Total	230	7.7					

Chapter 2
Water Degradation

Water typically contains a diverse array of dissolved and undissolved components in varying concentrations. These components encompass metal ions, colloids, gases, and particulate matter. Some of these constituents exert a significant impact on the interplay between water and materials.

This chapter provides a brief overview of the significance of water quality in nuclear power plants and fusion facilities. Additionally, chemistry of water is presented with a focus on the prime parameters and processes that are relevant for the interaction between water and reactor components. The focus is on the processes that take place or could take place in the primary cooling system. It is worth noting that these processes hold relevance for both nuclear reactors and fusion facilities.

2.1 Importance of Water Quality in Nuclear Reactor and Fusion Facilities

Water serves as the most common medium for dissipating the heat generated in both nuclear reactors and fusion facilities. The key to preventing the degradation of structural components lies in maintaining high-quality water.

In nuclear power plants, water plays multiple vital roles, serving as:

1. **Cooling fluid**: Water's primary function is to extract the heat generated by the fission reaction and transport it to the heat exchanger system;
2. **Moderator**: Water acts as a moderator by slowing down the high-energy neutrons produced in the fission process, rendering them suitable for triggering new fission reactions required to sustain the chain reaction;
3. **Radiological shielding**: Water serves as a radiological shield, attenuating the radiation emanating from the reactor core to ensure a safe environment for reactor operators.

Although water efficiently fulfils these three crucial functions, it can lead to undesirable conditions if its quality is compromised. Impurities dispersed within the water may become activated due to neutron flux as it circulates through the reactor core. Elevated levels of impurities can result in increased radiation levels, an outcome that is unfavourable and potentially hazardous [24]. Furthermore, low-quality water can contribute to the

accumulation of crud, which, in turn, diminishes thermal conductivity. This reduction in thermal conductivity can result in elevated fuel temperatures, expediting the oxidation of cladding and further reducing thermal conductivity. This forms a detrimental cycle that can ultimately lead to fuel failure.

Conversely, when water chemical purity is ensured, only its core components, such as deuterium in heavy water, are available for activation. This scenario promotes efficient heat transfer from the fuel to the coolant, maintains low electrical conductivity in the coolant, and establishes an environment with minimal corrosion rates for both fuel and structural materials within the reactor system.

The maintenance of exceptionally high-quality water is of utmost importance because water serves as the primary medium in contact with fuel elements and plays a key role in preventing the deterioration of fuel cladding and structural components within a nuclear reactor. Several factors can contribute to the degradation of water quality in a nuclear reactor, including the use of low-quality water sources for makeup, the introduction of environmental contaminants, biological activity, and corrosion within the primary circuit.

Given the intricate nature of water chemistry and its critical importance, significant efforts have been dedicated to advancing and enhancing water chemistry technologies in commercial Boiling Water Reactors (BWRs) and Pressurized Water Reactors (PWRs). These efforts have culminated in the development of comprehensive water chemistry guidelines aimed at ensuring the integrity and optimal performance of nuclear reactor systems.

In contrast, the determination of an appropriate water chemistry for cooling systems in fusion facilities remains a subject of ongoing debate [25]. The complexity of this task is related to the different requirements needed for each experimental fusion reactor under construction, like the International Thermonuclear Experimental Reactor (ITER), the Divertor Tokamak Test (DTT) or JT60 Super Advanced (JT-60A) as well as those in the design stage aimed to demonstrate power generation, such as the DEMOnstration power plant (DEMO) [26]. These fusion facilities and reactors will operate either in steady state (e.g., DEMO) or in pulsed mode (ITER, JT-60SA, and DTT), where there is a cyclic transition between oxidizing and reducing conditions.

The interaction of the ionizing radiation with the coolant (water) results in the generation of a variety of oxidizing corrosive species such as O_2, H_2O_2, and OH. Consequently, cyclic operation in fusion reactors significantly affects water chemistry, with the pulsed mode creating an oxidizing environment due to the effects of gamma and neutron irradiation on water radiolysis. This oxidizing phase during the pulse alternates with a reducing environment, which is preferable for both copper alloys and stainless steels [27], [28].

To address this challenge, a large amount of hydrogen in the range of 25 to 35 cm^3 kg^{-1} is added to Pressurized Water Reactor (PWR) primary coolant circuits and Boiling Water Reactor (BWR) cooling loops, operating under Hydrogen Water Chemistry. This addition serves to suppress the radiolytic generation of oxidizing species and/or to shift the corrosion potential of structural components in the coolant circuits in a negative direction. The addition of hydrogen is also anticipated in future fusion facilities to control and mitigate oxygen concentration resulting from water radiolysis [29].

Water has a certain potential to interact with materials found in components that come into contact with it. The nature and degree of this interaction are influenced by various factors, including the physical state and composition of the water, as well as environmental parameters such as temperature and pressure to which the materials are exposed.

2.2 Water Parameters to Monitor in a Fusion Reactor

Water is primarily composed of H_2O molecules. Approximately, one out of every 6500 water molecules is composed of deuterium instead of regular hydrogen, and water in its liquid state can undergo dissociation (ionization) into H^+ and OH^- ions, a process that depends on temperature. Besides H_2O, water can become impure due to the presence of various compounds, even if present in small amounts. Some of these compounds can significantly affect the properties of water within a research reactor.

The composition and concentration of impurities result from a series of reactions and interactions between the water and its surrounding environment. In systems with forced water circulation, the kinetic energy of the water flow can cause erosion of pipes and components within the system. This erosion leads to the mechanical release of tiny fractions of these components, which can take the form of particles. These particles can either settle as sediments or dissolve in ionic form, becoming cations like Na^+, Ca_2^+, K^+, or anions like Cl^-, CO_3^{2-} and SO_4^{2-}. It's important to note that water has a limited capacity for dissolving these species in a solution and when the 'solubility limit' of a particular compound is exceeded, that compound will precipitate.

Furthermore, there is a continuous interaction between the water and the atmosphere which can lead to the dissolution in water of certain species like O_2 and CO_2.These dissolved gaseous species have an impact on the composition and the chemical reactions that occur within the water. Another critical factor to take into account is temperature, as it significantly accelerates these reactions while also increasing the water's capacity to dissolve various species.

The primary goal of cooling water management is to preserve the water's purity by minimizing the presence of non-H_2O species. However, it's important to acknowledge that

interactions between the water, the materials it contacts, and the surrounding atmosphere cannot be completely avoided. By applying the fundamental principles of water chemistry, it is possible to model these interactions and quantify their contributions to the composition of the cooling water.

2.2.1 Conductivity

Conductivity is a very important parameter related to corrosion of metals in an aqueous medium. By definition, conductivity is simply a measure of the ability of a medium to carry an electric current. In the case of water, this ability is attributed to the presence of dissolved ionic species: the more anions and cations contained in water, the more electricity is carried, and the higher the conductivity.

The conductivity of water is expressed in S/cm (S = siemens), or more usually, in μS/cm, where siemens is the inverse of the resistance; 1 S = 1/Ohm. At room temperature (25 °C), the conductivity of pure water at 25°C is 0.0548 μS/cm.

It is understood that even in purified water it is impossible to avoid some degree of impurities. Notable sources of impurities in cooling systems include the corrosion of system components, which can release metallic impurities into the piping, as well as the presence of dust, interactions with air, aerosols, and the inclusion of detergents. Each of these ions introduced into the aqueous solution contributes to the overall conductivity. The conductivity of an ionic solution, k, is determined by:

$$k\left(\frac{\mu S}{cm}\right) = 1000 \cdot \sum \Lambda_i \cdot C_i \qquad \text{Eq. 2.1}$$

where:

Λ_i = The molar conductance of species i [mho cm^2 mol^{-1}] or [S cm^2 mol^{-1}]

C_i = The molar concentration of species i [mol L^{-1}] [20].

2.2.2 pH

In the context of managing water-cooled systems, pH and conductivity stand out as two of the foremost parameters employed to evaluate water quality. This importance arises from the fact that the pH of water significantly influences its interactions with metals. Therefore, ensuring precise and meticulous determination of pH is of paramount significance. The slight conduction of electric current implies the existence of ions, which are charged particles, within water. It becomes apparent that a fraction of water undergoes dissociation, transforming into H^+ and OH^- ions. In reaction form:

$$H_2O \Leftrightarrow H^+ + OH^- \quad \text{Eq. 2.2}$$

The ⇔ symbol indicates that this reaction is an equilibrium reaction, which means that the reaction is reversible. As for any equilibrium reaction, an 'equilibrium constant' K is defined, and for this specific reaction K is:

$$K_w = [H^+] * [OH^-] \quad \text{Eq 2.3}$$

K is, therefore, the mathematical product of $[H^+]$ and $[OH^-]$. At T = 25°C, K_w is equal to 10^{-14}, a constant for any aqueous solution at 25°C. As with any equilibrium reaction, the dissociation reaction of water is temperature dependent.

The value of pH is defined as the negative 'log' of the H^+ concentration when expressed in moles per litres:

$$pH = -\log [H^+] \quad \text{Eq. 2.4}$$

A solution with a pH value of 7 is 'neutral'; solutions with a pH value less than 7 are termed 'acidic'; and those with pH between 7 and 14, 'basic'. In acidic solutions, H^+ is dominant over OH^-, whereas in basic solutions, the opposite is the case. Perfectly pure water has a pH value of 7 [30], [31].

The relation between resistivity (the reciprocal of conductivity) and the pH of water is illustrated in 2.1.

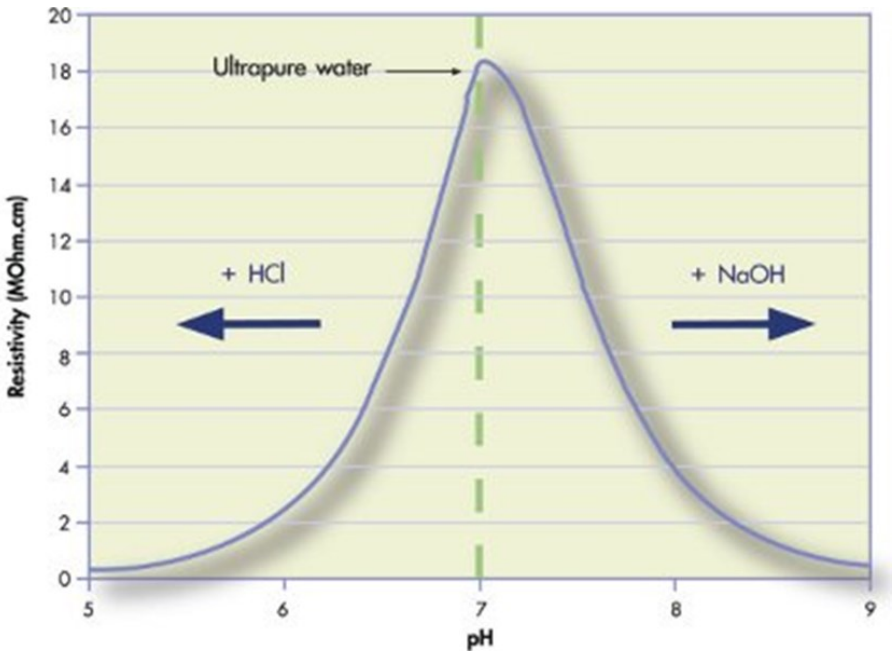

Figure 2.1: Ultrapure water resistivity vs pH [30]

2.2.3 Oxygen and Carbon Dioxide

In the equilibrium between gas and water, there is gas and water vapor in the gas phase, and dissolved gas and liquid water in the aqueous phase. The dissolution of the gas in the water is governed by Henry's law:

$$H = \frac{x}{p} \quad \text{Eq. 2.5}$$

where x is the fraction of the gas in the aqueous phase in mol kg-1, and p the partial pressure of the gas in the gas phase in bar.

When UPW enters in contact with air, it readily absorbs CO_2 which forms carbonic acid (Eq. 2.6, Eq. 2.7 and Eq. 2.8). This latter may lose protons to form bicarbonate (HCO_3^-) and carbonate (CO_3^{2-}). In this case, the hydronium ion (H_3O^+) is liberated to the water, decreasing pH.

$$CO_2 + H_2O \Leftrightarrow H_2CO_3 \quad \text{Eq. 2.6}$$

$$H_2CO_3 + H_2O \Leftrightarrow H_3O^+ + HCO_3^- \quad \text{Eq. 2.7}$$

$$HCO_3^- + H_2O \Leftrightarrow H_3O^+ + CO_3^{2-} \quad \text{Eq. 2.8}$$

Given that, upon exposure to the atmosphere, both CO_2 and oxygen are absorbed, monitoring oxygen levels plays a crucial role in assessing whether the system operates within its designated parameters and detecting any potential ingress of air into the circuit. A continuous on-line instrument is a good investment for detecting some types of adverse situations [30], [32], [33].

Pure water at 25°C in equilibrium with air with a CO_2 concentration of 338 ppm has a pH of 5.7, assuming that the air is in equilibrium with the water. The case of CO_2 uptake is a good illustration of an interaction between water and its environment. Regarding oxygen, at 25°C in equilibrium with air 8.24 ppm are dissolved in water. The amount of oxygen dissolved has a direct influence on material corrosion phenomena, as described in Chapter 3.39

The pH parameter monitoring and control can help reestablish equilibrium following a disturbance. For instance, if the pH decreases, counter reactions need to elevate the pH to return to the previous equilibrium state. The final pH level is the result of a series of reactions, with the number of reactions depending on the number of species present. The system's ability to regain equilibrium is often described as its "buffering capacity" [33].

With regards to oxygen, it plays a pivotal role in the corrosion processes occurring within nuclear power plants, impacting both fission and fusion reactor facilities. In fission

reactors, such as Boiling Water Reactors (BWR) and Pressurized Water Reactors (PWR), managing Dissolved Oxygen (DO) levels is critical to prevent stress corrosion cracking of stainless steels, which could compromise the integrity of reactor components The recommended DO levels vary between reactor types, with BWR coolant aiming for 200-300 ppb and PWR maintaining a level of 100 ppb. [34]. Similarly, in fusion reactor facilities like ITER, where copper components are prevalent, the presence of DO poses a risk of oxidizing copper surfaces. To address this, stringent measures are implemented to maintain very low DO levels, such as 10 ppb due to pronounced radiolysis issues associated with strong radiation fields [35]. Analysis of the interaction between Dissolved Oxygen and material surfaces will be presented in detail in Chapter 3.

2.2.4 Temperature

With regards of the effect of temperature on the UPW characteristics, an increase in temperature will determine an increase in the mobility of the ions in solution and an increase in the number of ions in solution due to dissociation molecules. Therefore, a rise in temperature leads to a higher conductivity value [21]. UPW has a very low electrical conductivity which indicates the electrochemical mobility of the hydrogen and hydroxide ions and it can be expressed as [21], [22]:

$$k\left(\frac{S}{cm}\right) = \rho^{-1} = 10^{-3} d K_w^{\frac{1}{2}} (\lambda_H^+ + \lambda_{OH}^-) \qquad \text{Eq. 2.9}$$

where d is the water density (g/cm^3), λ_H^+ and λ_{OH}^- are the specific conductances of H^+ and OH^- (S-cm^2/mol) and K_w the water dissociation constant. At 25°C, the accepted values with their uncertainties for conductivity, k, and its reciprocal, resistivity, ρ, are:

$$k\left(\frac{S}{cm}\right) = 0.05501 \pm 0.0001 \frac{\mu S}{cm} at\ 25°C \qquad \text{Eq. 2.10}$$

$$\rho = 18.18 \pm 0.03\ M\Omega cm\ at\ 25°C \qquad \text{Eq. 2.11}$$

Deviation from this value is a measure of trace ionic impurities [21], [22], [36].

A particular important property of pure water is its unique resistivity/temperature dependency. The sensitivity is referred as S_T and it can be defined as:

$$S_T = 100 \left(\frac{\partial \rho}{\partial T}\right)\Big|_T \left(\frac{1}{\rho}\right)\Big|_T \qquad \text{Eq. 2.12}$$

The sensitivity or temperature coefficient of ultrapure water varies considerably from 0-100°C and decreases dramatically as the temperature increases as shown in Figure 2.2.

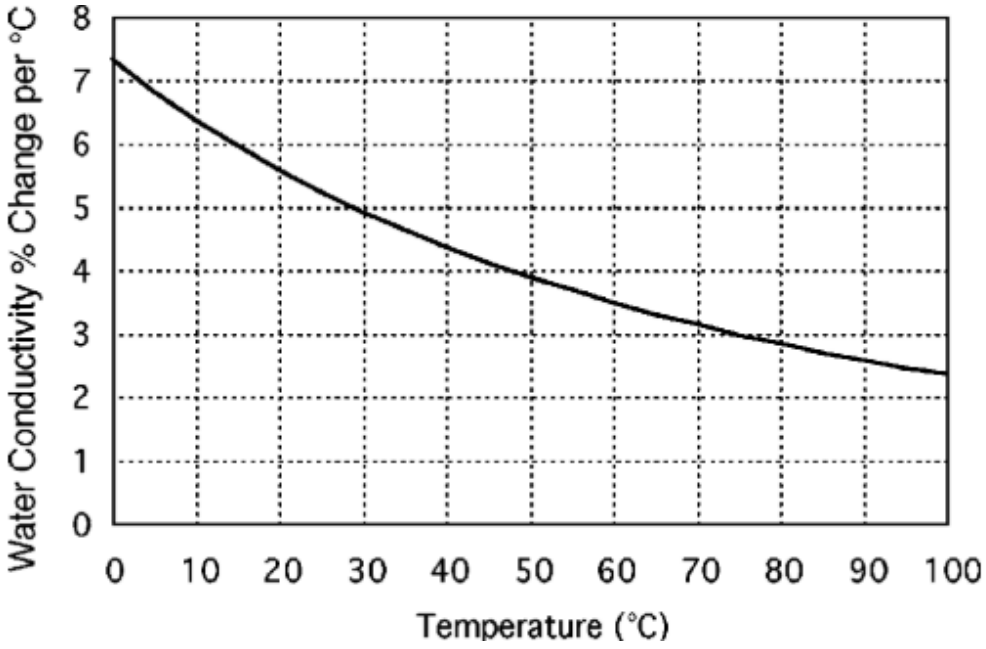

Figure 2.2: Sensitivity of pure water conductivity to changes in temperature [21]

Furthermore, temperature is a significant factor in pH measurements, and it can influence the pH of a solution. Generally, as the temperature of a solution rises, molecular activity and ionization increase, leading to the formation of more hydrogen ions (H^+). Consequently, the pH tends to decrease with higher temperatures.

2.2.5 Chemical Additives

Chemical additives are widely employed in nuclear power plants, both in Boiling Water Reactors (BWRs) and Pressurized Water Reactors (PWRs), to monitor and regulate water quality, ensuring the safe and efficient operation of these critical facilities.

BWRs were originally designed to operate with high purity water at natural pH of almost theoretical conductivity with radiolytically produced dissolved oxygen (100-300 ppb) and hydrogen (12-38 ppb) as reactor coolant. However, as these reactors operate, impurities accumulate due to the ingress of soluble and insoluble metallic species through the feedwater system. Some common impurities include iron, copper, and zinc, with the latter two often originating from brass condenser tubing. Stress corrosion cracking (SCC) of stainless steel components is a significant operational challenge in BWRs, and impurities in the water can exacerbate this issue.

The water impurities that can promote cracking are of two general sorts: oxidizing and ionic. Oxidizing impurities include dissolved oxygen in particular with 100-300 ppb. Oxidizing impurities increase the potential for intergranular stress corrosion cracking in

sensitized austenitic stainless steel piping and other structural components. Ionic impurities, such as chloride and sulphate, increase the conductance of the water, which increases corrosion rates. Chloride, in particular, can attack the passive film that protects stainless steel from corrosion [37], [38].

To address these challenges and maintain safe operation, BWR water chemistry has evolved over the years, resulting in several critical chemistry changes:

- **Hydrogen addition**: hydrogen is added to the feedwater to control the electrochemical corrosion potential (ECP) of reactor internal components and suppress oxygen generation due to radiolysis of the primary coolant;
- **Zinc addition:** injecting zinc into the feedwater helps reduce drywell dose rates by stabilizing radioactive cobalt. Cobalt is contained in some reactor internal components like control rod blade pins and rollers. The issue arises because cobalt, when released from these surfaces due to corrosion, becomes activated in the reactor core, transforming into radioactive cobalt-60 (60Co). This isotope emits high-energy gamma radiation and has a long half-life. As a result, radioactive 60Co deposits on out-of-core piping surfaces, including the recirculation piping, leading to an increase in drywell dose rates In the initial years of operation, plants managed to control drywell dose rates by frequently decontaminating the affected piping surfaces. However, as experience and research advanced, a more effective solution was found in the form of zinc oxide to the feedwater. Zinc helps in reducing 60Co incorporation on piping surfaces due to the greater thermodynamic stability of zinc ferrite and zinc chromite as opposed to their cobalt counterparts;
- **Noble metal chemical addition**: noble metals are added to mitigate stress corrosion cracking of structural components made from steels and nickel-based alloys [29], [37], [39].

On the other hand, the Pressurized Water Reactors (PWR) has three main water circuits: the primary water circuit, the water-steam cycle, and the cooling water system. The primary water circuit is characterized by an alkaline solution supplemented with different chemical additives:

- **Boric acid**: boric acid is added to control core reactivity. However, it results in an acidic environment that can increase the formation and transport of corrosion products on fuel rod surfaces;
- **Lithium:** lithium is added to maintain pH levels and enhance corrosion resistance. Operation at higher pH levels reduces the risk of crud deposition associated with fuel reliability issues;

- **Hydrogen**: hydrogen is injected into the primary coolant to maintain an appropriate concentration that suppresses oxygen generation by radiolysis. Oxygen can play a significant role in corrosion processes in PWRs. On one hand, the intake of oxygen from makeup water must be avoided, which can be achieved through makeup water degassing. On the other hand, radiolytically formed oxygen, produced by the radiochemical decomposition of water in the radiation field of the reactor core, needs to be suppressed. Reactive radicals generated by radiolysis can undergo chemical reactions with materials in the primary circuit, potentially causing material damage. Adding an excess of dissolved hydrogen to the coolant ensures the recombination of radiolytically formed oxygen into water without causing unacceptable corrosion of fuel cladding material;
- **Zinc-addition**: From BWR chemistry, a recent research program has also shown the feasibility of zinc addition to the primary coolant of PWRs, resulting in a noticeable reduction of the existing radiation fields [40], [41].

Regarding the steam-water cycle, water conditions have to be chosen to minimize corrosion that in the previous years have yield to costly repairs, power reductions, and steam generator replacements. Even small quantities of dissolved oxygen in boiler water are capable of causing severe pitting in boilers of all pressures, and will reduce the boiler life dramatically. Hydrazine is used in secondary water chemistry for combatting the detrimental effects of oxygen which is known to accelerate stress corrosion cracking of nickel alloys and stainless steel [42], [43].

Regarding fusion reactor facilities, the determination of an appropriate water chemistry for cooling systems in fusion facilities remains a subject of ongoing debate and depends on the different requirements needed for each experimental fusion reactor.

In fusion reactor facilities like JT-60SA, DTT, and ITER, the use of borated water serves a different primary function compared to nuclear fission reactors. In fusion reactors, the borated water is primarily used as a neutron shield to protect the superconducting coils and other reactor components from the high-energy neutrons generated during fusion reactions.

In ITER, the primary cooling system is called Tokamak Cooling Water System (TCWS) and it will use UPW as the heat cooling media, taking into advantage of the good experience from BWRs. To prevent corrosion and erosion of the piping system in ITER, strict water quality control measures are implemented using the CVCS. To control radiolysis, hydrogen injection into is planned to produce a reducing environment as a part of chemistry control to minimize corrosion problems. ITER faces distinct conditions compared to conventional nuclear reactors, including a higher irradiation intensity of 1.4 Mrad/s, as

opposed to 0.3-0.9 Mrad/s in BWRs and PWRs. Additionally, the working temperature in ITER is lower. These factors necessitate ongoing studies to assess corrosion data and determine the optimal water quality conditions to suppress water radiolysis and corrosion phenomena effectively.

In summary, fusion reactor facilities are characterized by unique operational requirements and challenges, and the selection of appropriate water chemistry and additives is a dynamic process that continues to evolve as research and experience accumulate. If additives are used, they should also be regularly monitored.

2.2.6 Oxidation-Reduction Reaction

Oxidation-reduction reactions are among the most prominent type of reactions in chemistry. The basic principle behind these reactions is that most elements (R) have a tendency to donate part of their electrons to elements (Ox) with a larger affinity to accept electrons:

$$Ox_1 + R_2 \leftrightarrow R_1 + Ox_2 \qquad \text{Eq. 2.13}$$

The tendency of a metal to donate electrons is largely determined by the distribution of electrons within the metal atom. The process of metal oxidation, also known as corrosion, results from a chemical reaction that leads to the deterioration of the metal's properties. Corrosion rates in a water environment can be significantly influenced when metals come into contact with each other, resulting in a specific type of electrochemical reaction known as "galvanic corrosion." Galvanic corrosion occurs in a water environment when two different metals with distinct electrochemical potentials are coupled together. If the potential difference between these metals is significant, the metal with the higher potential will donate electrons, while the other metal will act as an electron acceptor. In other words, one metal can cause corrosion of the other. Water plays a crucial role in these electrochemical reactions, serving as the medium for transporting the aqueous species involved in the reactions and facilitating the flow of electric current.

2.2.7 Fluid Velocity

Some material losses caused by flowing liquids under high velocity conditions can be related to the occurrence of a mechanical effect on materials. Flow velocity can have an effect of material erosion and in the solubility limit of the dissolving ionic species in the process water. The flow velocity provides a fresh solution (process water) to the metal surface that has a large capacity to take in the soluble ions (as it is far below its solubility limit value) thereby increasing the corrosion rate with velocity. The increase of wall shear stress caused

by the high flow velocity leads to the rupture of passive films and the exposure of fresh metal in the corrosive media, which causes the increase of corrosion rate. Fluid velocity can also influence the Flow Accelerated Corrosion (FAC). Flow accelerated corrosion (FAC) is distinct from erosion and is primarily an electrochemical corrosion process aided by chemical dissolution and mass transfer. Flow accelerated corrosion (FAC) causes wall thinning (metal thickness loss) of carbon steel piping, tubing and vessels exposed to flowing water or wet steam. When the thickness of the component reaches values lower than the critical thickness required for supporting the operating stresses, it results in ductile failure of the component [44], [45].

Chapter 3
Degradation of Materials in Water

The degradation of materials when immersed in water is a highly intricate process. It varies depending on the type of material and the composition of the water, leading to various chemical reactions that result in the formation of either soluble or insoluble compounds. Different material degradation processes (i.e. corrosion, erosion, cavitation, liquid droplet impingement, flow accelerated corrosion, etc.), can occur in flowing water and can lead to wall thinning of pipes or components in power plants.

With regards to corrosion, because water is a potent polar solvent, metallic materials have a tendency to dissolve, a phenomenon known as corrosion, when exposed to water and water-based solutions. This corrosion occurs through electrochemical reactions involving several commonly present dissolved species, namely:

1. Hydrogen ions (H^+ or protons), which are generated from the dissociation of water.
2. Oxygen, originating from the air and dissolving in water as O_2.
3. Dissolved impurity ions (i.e. halogens).

During erosion, very small fractions of these components are mechanically released in the form of particles that are transported downstream, to be deposited as sediments, or dissolved in the form of charged particles. In one-phase flow, erosion is the phenomenon that leads to a mechanical surface destruction of the material mainly due to high liquid flow velocities. The shear stress (which relates the near-wall conditions of flows), pressure drop (which can be converted in terms of additional shear stress), and variations in the fluid velocity are the main factors which can induce erosion. In two-phase flow (wet steam), liquid droplet impingement-induced erosion or liquid impact-induced erosion are the processes that are caused by flowing gases or vapours containing liquid droplets. On circuits with forced circulation, the kinetic energy of the water stream causes erosion of pipes and components of the circuit.

Cavitation is the name given to the repeated growth and collapse of bubbles in a fluid due to local pressure fluctuations. If the pressure in a flowing liquid falls below its vapor pressure, because of sharp changes in flow geometry for example, vapor containing cavities is nucleated. These cavities are transported downstream of the flow singularity. When they reach a region of higher pressure, they grow and collapse violently and may cause erosion of any solid in their vicinity by formation of a micro jet. Thus, the phenomenon is for the most part mechanical in nature: shock wave emission and jet formation with subsequent impact by

collapse of the individual cavities are the fundamental factors responsible for cavitation-induced erosion.

Flow accelerated corrosion (FAC) is distinct from erosion and is primarily an electrochemical corrosion process aided by chemical dissolution and mass transfer. When the thickness of the component reaches values lower than the critical thickness required for supporting the operating stresses, it results in ductile failure of the component. If undetected, the degraded components can suddenly rupture, releasing high temperature steam or water.

The careful selection of appropriate materials for any functional component that comes into contact with water is of paramount importance. This is because the interaction between the water and the component can have a significant impact on the chemical and mechanical properties of the component itself. Prolonged interactions may result in degradation, often in the form of corrosion, leading to a loss of structural integrity in the component. Therefore, material selection is typically limited to those materials known to exhibit minimal interaction with water during extended exposure under a range of conditions.

In experimental or research reactors, various metallic materials are commonly employed. Specifically, in the primary circuit of nuclear reactors, structural components are often constructed using stainless steels. In the case of the NBTF experiments, the primary materials include stainless steel (304L for piping and 316L for components inside the vacuum vessel) and copper and copper alloys, predominantly used for actively cooled components. Welding is present in all systems, including welding between copper alloys and stainless steel. The connection between SS 316L and copper is achieved through a Vacuum Tight Threaded Junction (VTTJ), where the two metals are mechanically screwed together, creating a metallic seal. A detailed description of this junction can be found in the work of P. Agostinetti et al.[46].

In this chapter, the various modes and mechanisms of material degradation within reactor water systems will be explored, with a specific focus on materials commonly utilized in SPIDER and MITICA. The fundamental principles of water chemistry and its impact on materials, introduced in Chapter 3 , will be further elaborated upon. The objective of this detailed exploration is to identify specific water quality conditions that can result in degradation in these materials.

3.1 Stainless Steel

The formation of a protective oxide layer on stainless steels is typically observed under all water temperature and pH conditions during reactor service. This oxide layer, referred to as a passive film, plays a critical role in inhibiting corrosion processes by acting as a diffusion barrier. The characteristics of this oxide layer are influenced by the specific

environment and process conditions. In water environments, austenitic steels, for instance, develop a thin passive oxide layer.

The structure, composition, and thickness of this passive film are contingent upon the chemical composition of the alloy and the exposure conditions. Typically, on SS304L/SS316L type steels exposed to pressurized waters, a dual-layer oxide structure forms. This structure consists of an inner layer enriched with chromium ($FeCr_2O_4$) and an outer layer composed of spinel magnetite (Fe_3O_4). In environments with elevated temperatures (approximately 150-200°C), the oxide layers are significantly thicker than those formed at ambient temperatures. Conversely, at lower temperatures, the passive film is notably thinner, often measuring only a few nanometres in thickness. The formation of these oxide films is facilitated by the diffusion of iron (Fe) to the outer layer, with chromium (Cr) and nickel (Ni) exhibiting slower diffusion rates and consequently accumulating in the inner layer [47], [48].

The chromium oxide layer, situated at the surface of the stainless steel, serves as a robust barrier against ongoing oxidation and corrosion. Consequently, the rates of uniform corrosion for stainless steel in reactor systems are negligible [49]. However, the passivation layer on the stainless steel surface can become compromised due to various factors, including the presence of specific chemical species (e.g., chloride ions), a depletion of oxygen, or chromium depletion at grain boundaries, a phenomenon referred to as sensitization.

According to Molander [50], one of the primary concerns associated with the interaction of Stainless Steel with pure water in fusion devices like ITER is the occurrence of Stress Corrosion Cracking (SCC). SCC in stainless steel is typically the result of three simultaneous factors:

1. A sensitized microstructure characterized by the precipitation of chromium carbides at grain boundaries.
2. An aggressive water environment.
3. Tensile stresses.

A sensitized microstructure, often accompanied by weld residual stresses, can develop in the heat-affected zone adjacent to welds in austenitic stainless steel. If this condition exists within a system, the only easily modifiable factor is the water environment itself. In fusion reactor devices, particularly in ITER, two primary methods are considered to mitigate SCC.

The first method involves the addition of hydrogen. The introduction of hydrogen into the water serves to reduce the radiolysis decomposition of water, consequently lowering the concentration of oxidants in the reactor water. This, in turn, reduces the corrosion potential.

The second method entails the use of low carbon stainless steels. The introduction of these L-grade materials was expected to significantly reduce the likelihood of future cracking incidents. However, more recently, instances of cracking in L-grade stainless steel have been reported in U.S. and Japanese Boiling Water Reactors (BWRs), and to some extent, in Swedish BWRs as well. In Japanese BWRs, in particular, a substantial number of failures were documented, leading to extended outages [51]. In many cases, it appears that cracking is promoted by a cold-deformed and hardened surface layer resulting from processes such as grinding or other machining methods. Additionally, it seems that high local tensile stresses at the base of the weld, in contact with the reactor water, could have played a role in initiating the cracks. Consequently, for fusion reactors, notably ITER, cold working and post-weld treatments are considered crucial unresolved issues due to the intricate nature of manufacturing procedures.

Stainless steel is susceptible to crevice corrosion when certain ions, with chloride being the most significant, compete for a location and deteriorate the protective oxide film on the stainless steel's surface. Once a pit is initiated, the depletion of oxygen at the bottom of the pit can impede the reformation of the stainless steel's passive layer, allowing crevice corrosion to persist. It's important to note that crevices can expedite crack initiation in any environment, whether the material is sensitized or non-sensitized. However, sensitized steels tend to experience faster attacks, and higher conductivity is required to induce cracking in non-sensitized steel.

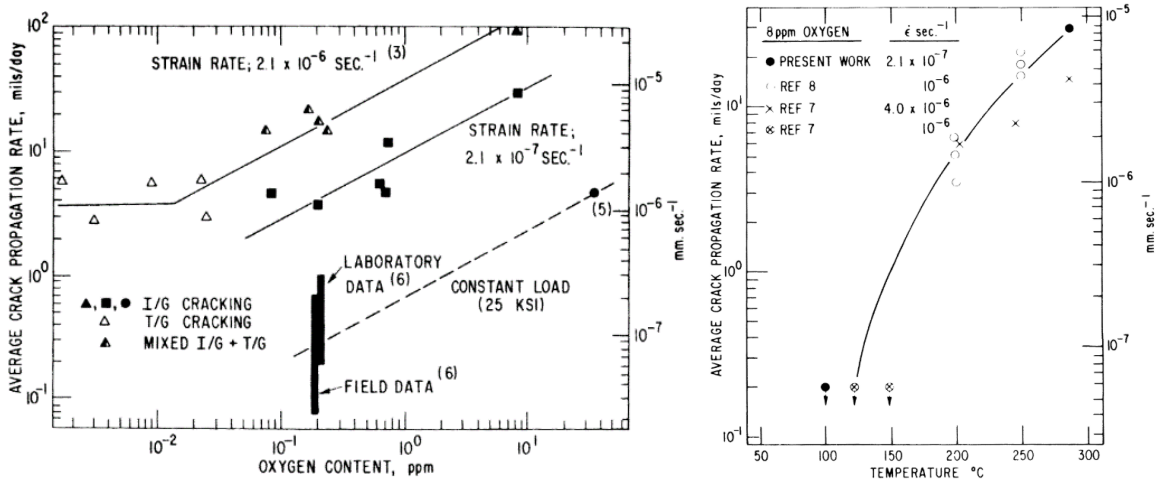

Figure 3.1: a) Relation between average crack propagation rate for SS304 and dissolved oxygen in ultrapure water, b) Relation between average crack propagation rate for SS304 and temperature in ultrapure water, with 8 ppb of dissolved oxygen

Ford and Povich [52] have illustrated the relationship between stress corrosion susceptibility and the morphology of cracking concerning the concentration of oxygen (Figure 3.1a) and temperature (Figure 3.1b) in High Purity Water (conductivity <0.4 μS/cm). Minimizing the combination of oxygen concentration and temperature is essential to mitigate the propagation of stress corrosion cracks.

Molander [35] reports the general corrosion rate of austenitic steels in a medium-low temperature regime, between 130 °C and 200 °C (Figure 3.2). Figure 3.2 was used to retrieve corrosion rates for SS in SPIDER operating conditions which will be described in Section 6.1.

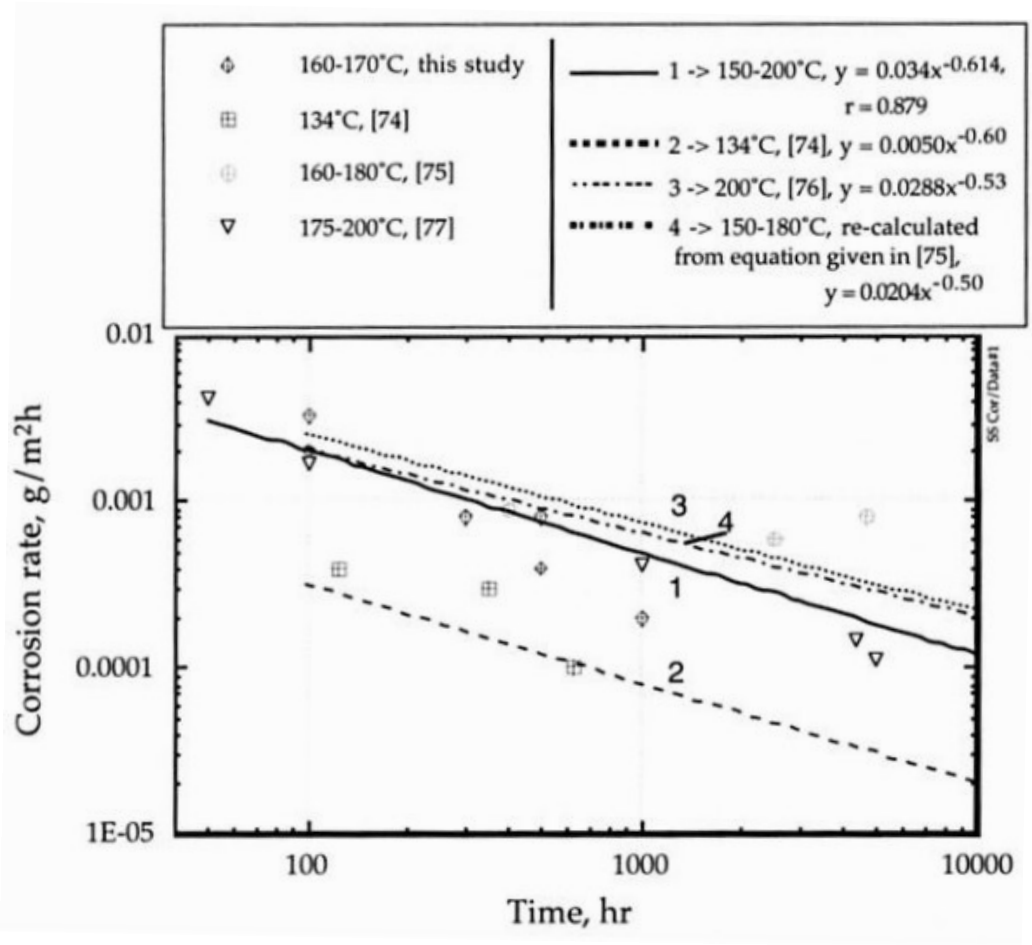

Figure 3.2: General corrosion rate of austenitic steels in the temperature range 134-200°C [50]

3.2 Copper

Copper is considered to be generally stable in pure water [31][53]. However, when oxygen (O_2) and carbon dioxide (CO_2) are introduced into the water through interactions with the atmosphere, an oxide layer (either copper (I) or copper (II)) forms on the surface of the metal.

Examples of copper corrosion/erosion phenomena are the failure of five backplates in JET and the obstruction of the coolant passages in the Wiggler magnets of the DaΘne Main Rings. DaΘne is an electron-positron collider at the INFN Frascati National Laboratory in Frascati

In JET, five backplates have failed in operation on JET, representing more than 50% of all the failures / unavailability periods on the neutral beam system in general [54].

Demineralized cooling water circulating within the PINI loop reacted with the internal copper surfaces of the backplate. The PINI cooling water system is nominally a closed loop system, which would in theory mean that there is only a finite amount of dissolved O_2 and CO_2 available for reaction with copper (the expansion tank is membrane sealed from the atmosphere). The reality is that over the lifetime of JET, there have been numerous interventions that have resulted in draining down and re-filling of the PINI loop, and in each of these interventions, fresh dissolved O_2 and CO_2 will have been introduced into

a)

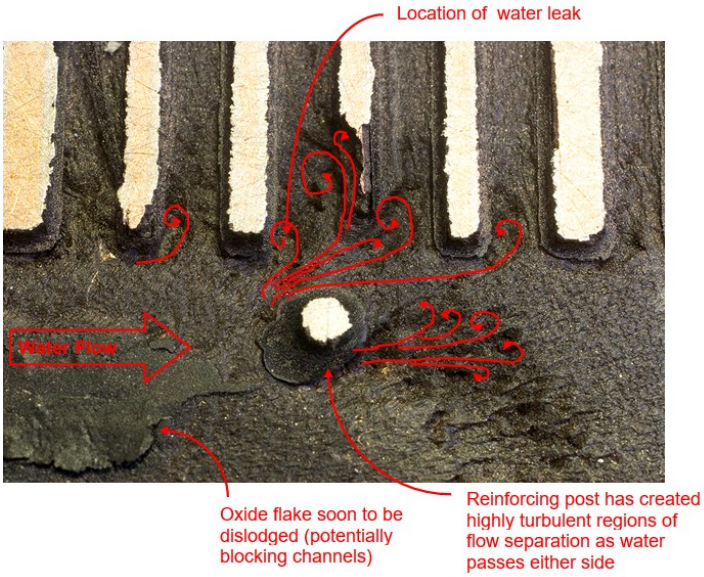

b)

Figure 3.3: a) JET backplate cross-section; b) Backplate photograph with corrosion / erosion phenomena [53]

the system. Notably, the demineralization plant lacks a deaeration facility, and no dosing of oxygen scavenger is implemented.

DaΘne experienced repeated failures due to obstruction of the coolant passages in the Wiggler magnets of the DaΘne Main Ring. . The coils are made of OFHC copper. The material of obstruction was analysed by SEM microscopy with EDS spectrometer. The conclusion was that the relatively high conductivity, the relevant dissolved oxygen contents of cooling water and the high electric potential of some coils with respect to the grounded piping yield the production of copper oxides and their migration according to the potential difference. Probably,, showing copper and copper oxides [55].

These examples underline the importance of monitoring all water parameters that can influence copper corrosion.

3.2.1 Influence of pH

As previously explained, when carbon dioxide (CO_2) is absorbed by water, it leads to the formation of carbonic acid, followed by the generation of bicarbonate and hydrogen ions. Notably, the presence of carbon dioxide has the effect of shifting the pH level of the cooling water towards lower values. The pH level significantly influences the corrosion rate, as depicted in Figure 3.4 [56]. The corrosion rate is minimized when the pH approaches values around 8.5 and higher.

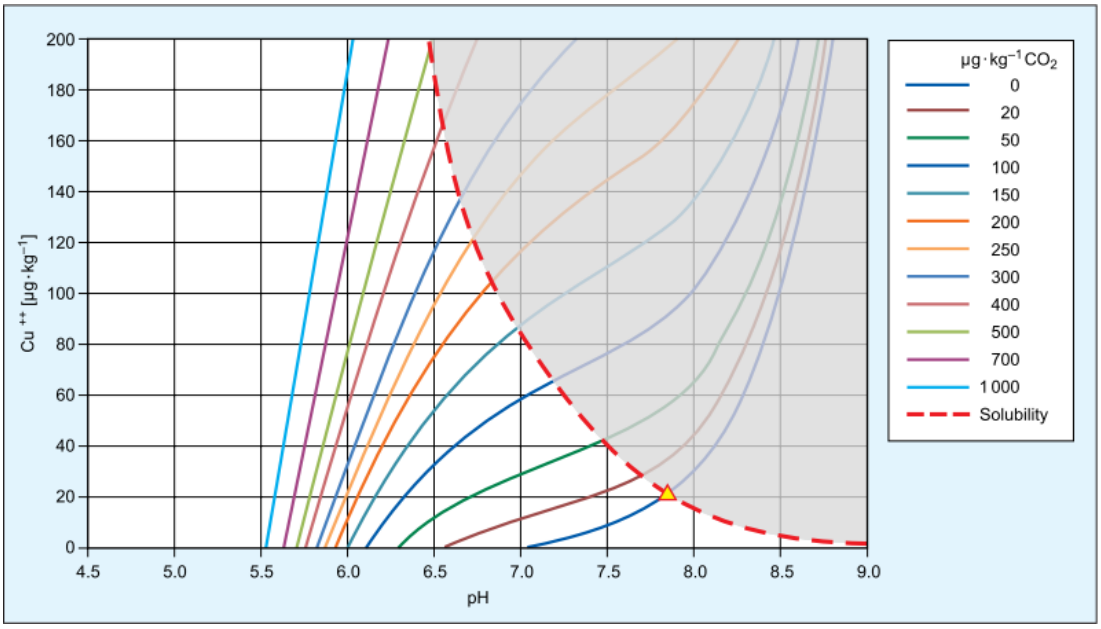

Figure 3.4: : Relation of Cu^{2+} and CO^2 to pH at 25 °C [56]

Furthermore, the Pourbaix diagram in Figure 3.5[57] illustrates the stable forms of copper in aqueous solutions based on pH and metal potential. For pH values below 7.0, copper ions remain stable in the solution. The formation these ions occurs when the pH is just slightly below 7.0, as a result of the reaction between H^+ ions and the oxygen within the oxide. On the other hand, for pH values above 7.0, the preferred form of the metal is the oxide. In this range, the replacement of oxygen in the oxide occurs less readily, which slows down the corrosion process [31].

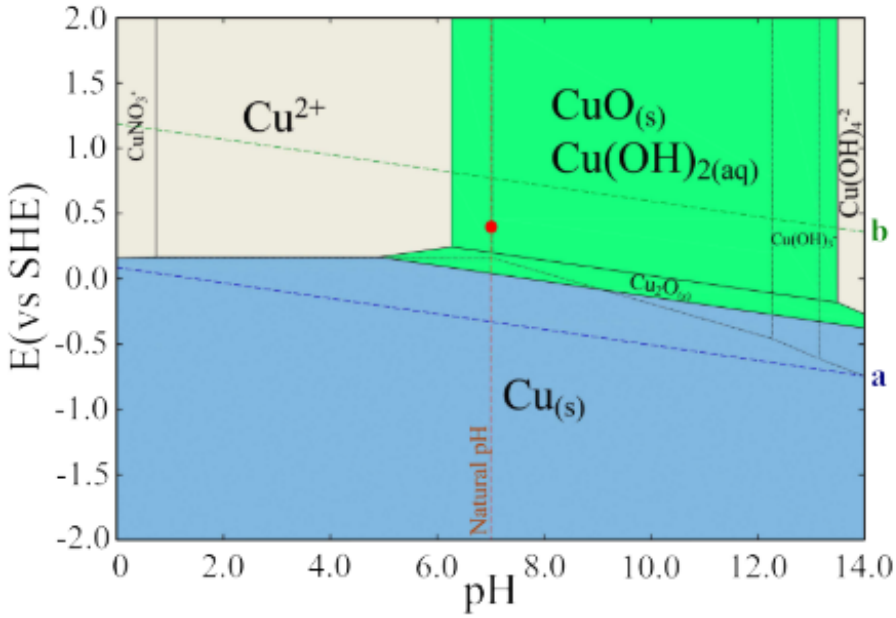

Figure 3.5: Calculated potential-pH (Pourbaix) diagram for copper in deionized water.[57]

3.2.2 Influence of Dissolved Oxygen

Oxygen (O_2) and carbon dioxide (CO_2) become naturally present in water as a result of interactions with the atmosphere. In the absence of other factors, these interactions lead to the formation of an oxide layer on the metal surface, which typically remains stable. However, the presence of CO_2 in the water initiates the creation of carbonic acid (H_2CO_3), which subsequently dissociates into bicarbonate (HCO_3) and hydrogen ions (H^+). These hydrogen ions have a strong attraction to the oxygen atoms within the oxide layer, readily forming water. As a consequence, the copper on the surface transforms into its ionic form and readily dissolves. With the oxide layer no longer providing protection, the metal surface is once again exposed to water, dissolved oxygen (DO), and H^+, allowing the corrosion process to repeat itself [32], [58].

The corrosion rate of copper in water, as influenced by the levels of dissolved oxygen and pH, is depicted in Figure 3.6. Notably, under neutral pH conditions, a high corrosion rate is observed when water contains 200-300 ppb of dissolved oxygen [31].

The oxides that form on copper surfaces are typically a mixture of Cu_2O and CuO. Cu_2O tends to dominate in low-oxygen systems, while CuO becomes prevalent in high-oxygen environments. There are two primary approaches to control copper oxidation, as indicated in Figure 3.6:

1. **Low-oxygen system**: this approach aims to minimize copper oxidation by maintaining extremely low oxygen levels within the system. Under such conditions, all incoming oxygen is consumed by the copper surfaces, leading to the predominant formation of cuprous oxide (Cu_2O);
2. **High-oxygen system**: In this scenario, the system allows for the formation of an oxide layer, primarily composed of cupric oxide (CuO) [59].

Cuprite and tenorite are formed by the following reactions:

$$2Cu + O_2 + H_2O \rightarrow 2CuO + H_2O \quad \text{Eq. 3.1}$$

$$4Cu + O_2 + H_2O \rightarrow 2Cu_2O + H_2O \quad \text{Eq. 3.2}$$

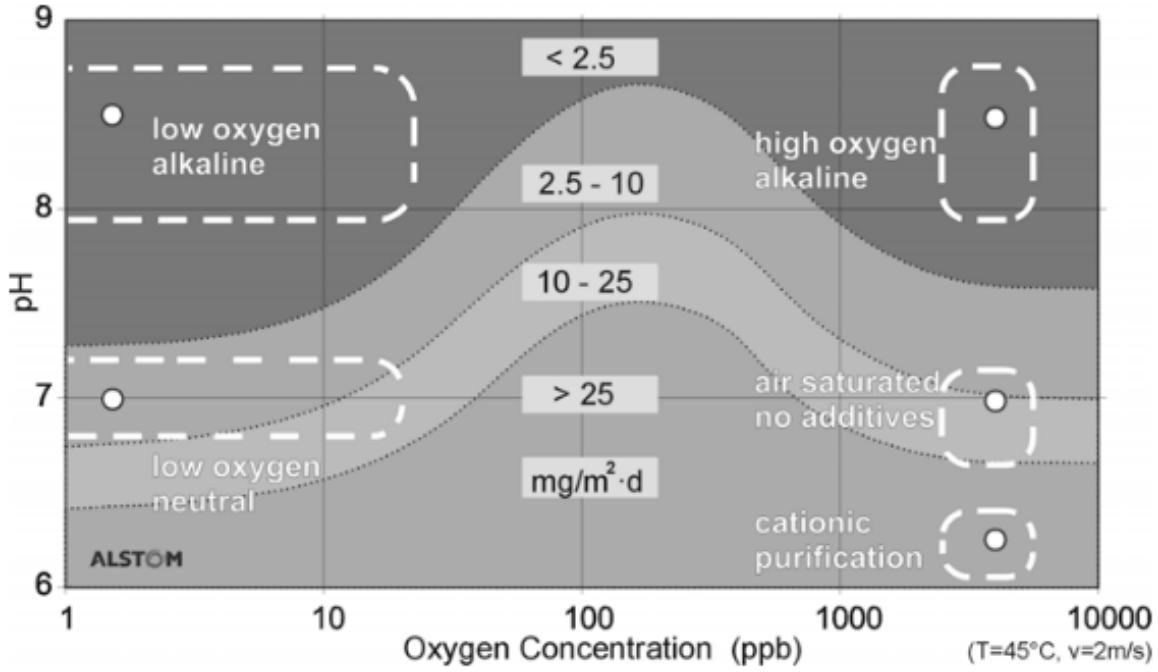

Figure 3.6: Corrosion rate vs DO and pH [31]

These oxide layers are typically quite thin. However, if these deposits are released into the water and subsequently redeposited at specific sites, they can lead to the impairment and even plugging of tubes with small cross-sections.

The process of flow restriction growth can be divided into four steps:

1. **Oxidation of copper surfaces**: Copper surfaces undergo oxidation;
2. **Release of oxidized copper**: The oxidized copper is released into the water;
3. **Migration of released copper**: The released copper moves within the water;
4. **Re-deposition of migrating copper**: Copper re-deposits at various locations, potentially leading to flow restrictions or blockages in the system [60].

The release rate can be described by:

$$\frac{dm}{dt} = k(C_B - C_w) \quad \text{Eq. 3.3}$$

The term *dm/dt* is the release rate and k is the mass transfer coefficient and it is affected by water velocity, turbulence and flow geometry. C_B is the copper concentration in the oxide/boundary layer, which depends on chemical and thermodynamic parameters, and C_w the copper concentration in the bulk liquid. Therefore, the copper release rate is function of water chemistry and thermodynamic parameters, like velocity and temperature.

After copper is released into the water, it circulates within the system until it finds a location for absorption. Studies on oxide deposits have revealed that the re-deposition of copper tends to occur preferentially at the inlets and outlets of hollow conductors, as well as at points within the hollow conductors where there are flow disturbances. These areas, characterized by elevated turbulence, are particularly prone to copper re-deposition [61].

3.2.3 Influence of Temperature

Figure 3.7 illustrates how copper solubility changes with temperature across different pH levels. Notably, when the pH drops below 7.0, temperature becomes a more significant factor and provides an explanation for water flow restrictions that occur at the outlet ends of copper components subjected to high heat fluxes.

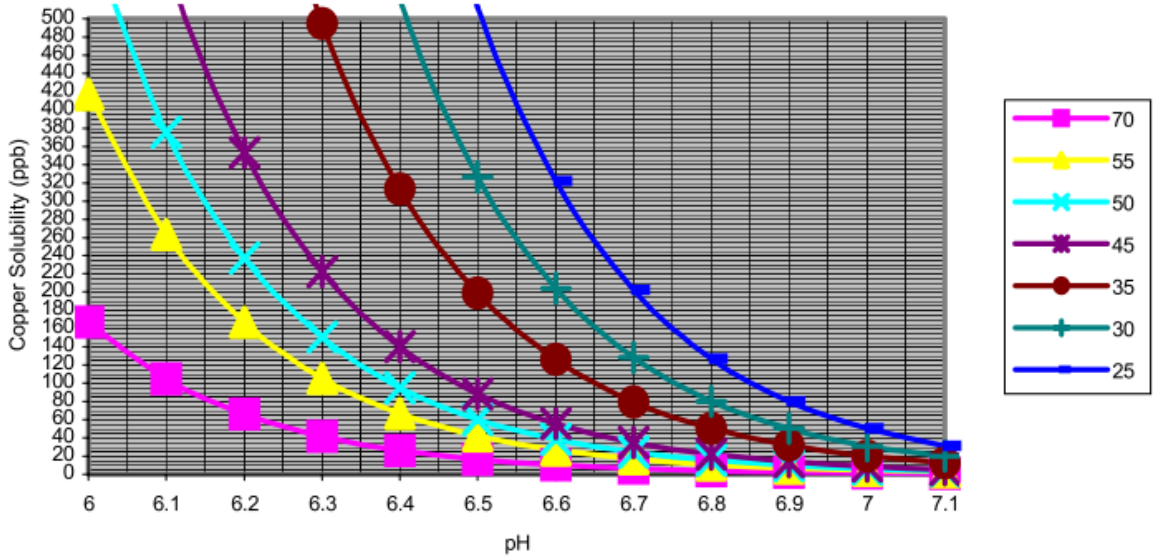

Figure 3.7: Copper solubility vs pH [62]

Chapter 4
Basics of Characterization Techniques

The aim of this chapter is to give an overview of the experimental techniques used in this thesis. All material analyses were conducted in various laboratories situated in Padua, distinct from the Consorzio RFX. Section 4.1 introduces the SEM: Scanning Electron Microscope (SEM); Section 4.2 the X-Ray Diffraction (XRD); Section 4.3 the Stylus Profilometer; Section 4.4 the ICP-MS: Inductively Coupled Plasma-Mass Spectrometry and Section 4.5 the Calotest Instrument.

4.1 SEM: Scanning Electron Microscope

Scanning electron microscopy (SEM) is a powerful imaging technique that produces highly detailed and magnified images of an object's surface. It achieves this by scanning the object's surface with a focused beam of high-energy electrons, which can be accelerated to speeds of up to 1000 keV. These high-energy electrons interact with the sample's surface, generating a wide range of signals, including electrons, X-rays, and photons. These signals, originating from the interactions between electrons and the sample, provide valuable information about the sample's external morphology (texture), chemical composition, and the crystalline structure and orientation of its constituent materials. In most SEM applications, data are collected over a selected area of the sample's surface, and this information is used to generate a two-dimensional image that visually represents spatial variations in these properties.

The SEM instrument typically begins with an electron gun that generates a beam of electrons at the top of the microscope. This electron beam then follows a vertical path within a vacuum environment. The vacuum conditions are crucial as they prevent molecules or atoms already present in the microscope column from interfering with the electron beam's path. As the electron beam traverses the microscope, it passes through electromagnetic fields and lenses, which serve to focus and direct the beam toward the sample. Upon striking the sample's surface, the interaction between the electron beam and the sample results in the emission of electrons and X-rays. These emissions contain valuable information about the sample's composition and structure, effectively revealing what the object is made of. Figure 4.1 illustrates the essential elements of this SEM.

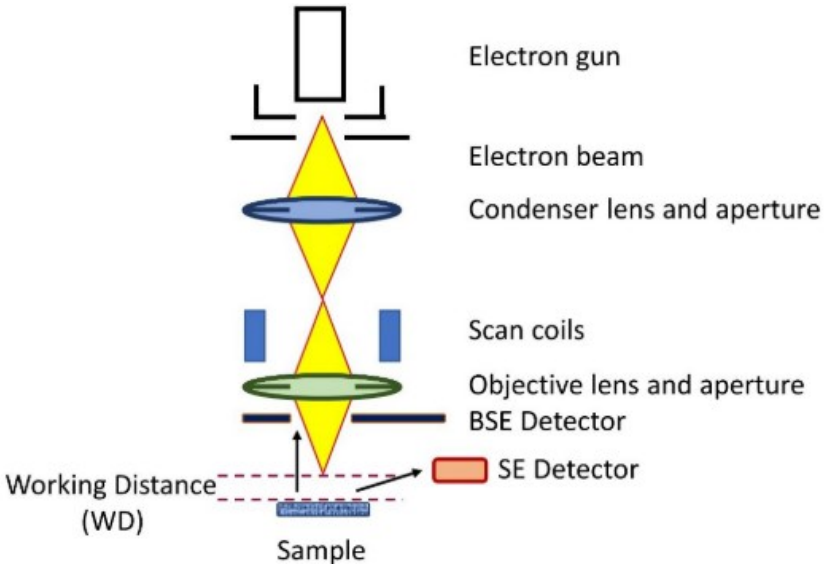

Figure 4.1: Schematic of a Scanning Electron Microscope

The signals commonly used when a sample is analysed under SEM are:

- **Secondary Electrons (SE):** these electrons are emitted from the sample after being escaped from their atomic orbitals by the incident high-energy electron beam. They typically have energies below 50 eV. SE imaging (SEI) is primarily used to provide topographical information, revealing the surface's three-dimensional structure. While SEI is mainly employed for topography, it may also offer some compositional contrast as the detector can collect some backscattered electrons;
- **Backscattered electrons (BSE):** these are incident electrons that scatter backward into the detector after interacting with the atoms in the sample. While there are fewer BSE compared to SE, they possess higher energy, roughly on the same order of magnitude as the incident electrons. The resolution achieved with BSE is lower than that of SE because the probability of nuclear interactions is relatively low. This means that BSE tend to interact with a larger volume of material before scattering back into the detector from deeper within the material. BSE provide compositional information: brighter areas correspond to elements with a larger atomic mass, as the chance of backscattering increases with the increase of atomic number, whilst dark areas indicate light elements;
- **X-rays:** X-rays are generated when a high energy electron knocks an electron from an atom’s inner shell, causing an electron from a higher energy shell to move into the empty orbit in a series of energy jumps. The energy difference

is emitted in the form of high-energy electromagnetic radiation, specifically X-rays. Measurement of the energy of the X-rays obtained provides information about the elements present in the sample, as each element emits characteristic X-rays, usually in the range of 0 to 10 keV. Different elements have characteristic arrangements of electrons in well-defined energy states, and the energy of the emitted X-rays depends on the energy differences between these states.

Two types of detectors are available for analysis of the characteristic X-ray spectra: Energy Dispersive X- ray Spectroscopy (EDS or EDX), which sorts the X-rays on the base of their energy; Wavelength Dispersive X-ray Spectroscopy (WDS or WDX, which sort the X-rays based on their wavelengths.

The resolution of a SEI can be improved by choosing an appropriate sample working distance (see Figure 4.1), beam current, accelerating voltage and spot size.

The SEMs used for the investigations described in this thesis were FEI QUANTA 200 (FEI, Hillsboro, OR, USA) and COXEM EM3AX Plus (COXEM Co., Daejeon, Korea) microscopes, shown in Figure 4.2a and Figure 4.2b respectively. The SEM included and X-ray detector EDAX Element-C2B. Both SEM microscopes worked with a W-filament source and with an accelerating voltage of 20 kV. SEM analyses were performed at the Centro di Analisi e Servizi Per la Certificazione (CEASC) laboratory.

a)

b)

Figure 4.2: SEM-EDS used for investigations. a)FEI QUANTA 200; b) COXEM EM3AX Plus

4.2 XRD: X- Ray Diffraction

X-ray Diffraction (XRD) is a powerful analytical technique used to determine the crystallographic structure, phase composition, and microstructural properties of crystalline materials. This non-destructive technique relies on the scattering of X-rays by the atomic planes within a crystalline sample, providing valuable insights into its atomic arrangement.

The X−rays are generated by a cathode ray tube, where they are meticulously filtered to yield monochromatic radiation. Subsequently, these rays are precisely collimated and concentrated, then directed towards the sample. As these incident rays interact with the specimen, they give rise to constructive interference, resulting in the formation of a diffracted ray. This phenomenon adheres to the principles outlined in Bragg's Law, denoted as:

$$n\lambda = 2\mathrm{d} \cdot \sin\theta \qquad \text{Eq. 4.1}$$

Bragg's Law describes the relationship between the angle of incidence (θ), the wavelength of X-rays (λ), and the spacing between atomic planes (d) in a crystal lattice. According to Bragg's Law, constructive interference of X-rays occurs when 2d sin(θ) equals an integer multiple of the X-ray wavelength (nλ).

The main XRD components are:

1. **X-ray Source:** X-rays are generated in a cathode ray tube by heating a filament to produce electrons, accelerating the electrons toward a target by applying a voltage, and bombarding the target material with electrons. When electrons have sufficient energy to dislodge inner shell electrons of the target material, characteristic X-ray spectra are produced. These spectra consist of several components, the most common being Kα and Kβ. Kα consists, in part, of Kα1 and Kα2. Kα1 has a slightly shorter wavelength and twice the intensity as Kα2. The specific wavelengths are characteristic of the target material (Cu, Fe, Mo and Cr). Filtering, by foils or crystal monochrometers, is required to produce monochromatic X-rays needed for diffraction. Kα1and Kα2 are sufficiently close in wavelength such that a weighted average of the two is used. These X-rays are collimated and directed onto the sample;
2. **Sample Holder:** The crystalline sample is finely ground or powdered and loaded onto a sample holder. Thin films or single crystals can also be analysed;
3. **Goniometer:** A goniometer allows precise control of the angle of incidence (θ) and the angle of detection to explore a wide range of diffraction angles. As the sample and detector are rotated, the intensity of the reflected X-rays is recorded. When the geometry of the incident X-rays impinging the sample

satisfies the Bragg Equation, constructive interference occurs and a peak in intensity occurs;

4. **Detector:** The diffracted X-rays are collected by a detector, typically a scintillation counter or a solid-state detector. The detector records the intensity of X-rays at different angles and converts the signal to a count rate which is then output to a device such as a printer or computer monitor. The resulting diffraction pattern consists of peaks at specific θ angles. The positions of these peaks correspond to the d-spacing of the atomic planes within the crystal. The pattern is compared to a database of known crystal structures to identify the phases present in the sample. Peak widths and intensities are analysed to determine crystallite size, microstrain, and other structural information.

XRD analyses conducted hereafter were done using Panalytical XPert 3 Powder (Malvern Panalytical Ltd., Malvern, UK). The instrument, shown in Figure 4.3, consisted of a Cu-anode X-ray tube and solid-state detector PixCel. XRD analyses were conducted by the Centro di Analisi e Servizi Per la Certificazione (CEASC) laboratory.

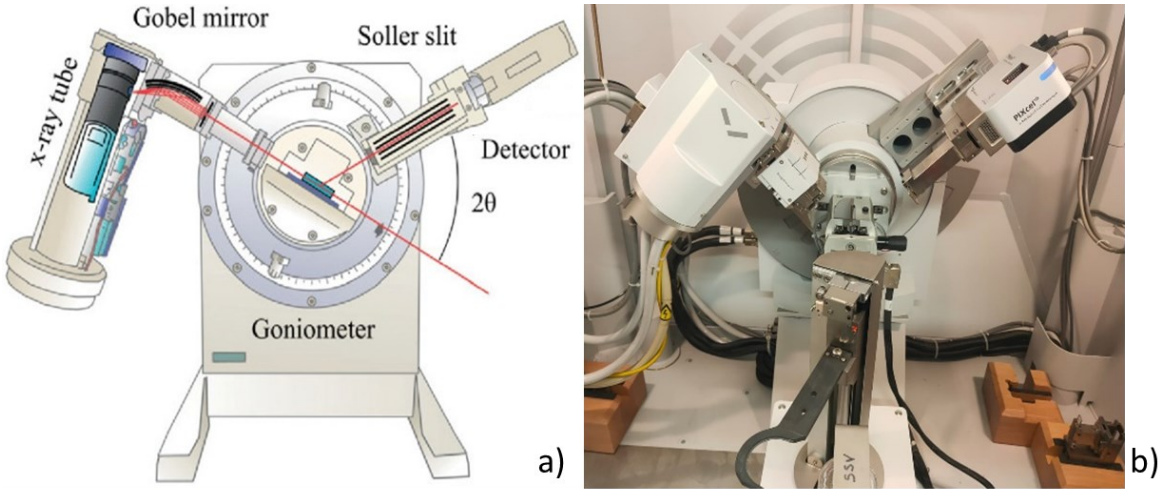

Figure 4.3: a) X-Ray diffractometer and its components, b) Photo of the XRD used for the investigations

4.3 Stylus Profilometer

In this work of thesis, roughness was measured using a stylus profilometer (DektakXT®, Bruker, Germany) and shown in Figure 4.4b. Profilometer analyses were conducted at the Instituto di Chimica della Materia Condensata e di Tecnologie per l'Energia (ICMATE) laboratory

Stylus profilometers use a probe to detect the surface, physically moving a probe along the surface in order to acquire the surface height. This process involves mechanical movement and utilizes a feedback loop to monitor the force exerted by the sample against the probe as it scans across the surface. A feedback mechanism is employed to maintain a specific torque on the arm, referred to as the 'setpoint.' The changes in the vertical (Z) position of the arm holder are then used to reconstruct the surface topography.

Due to the physical movement required in the X, Y, and Z directions, coupled with continuous contact with the surface, stylus profilometry tends to be slower when compared to non-contact measurement techniques. The size and shape of the stylus tip, as depicted in Figure 4.4a, can also have an impact on the measurements and may impose limitations on lateral resolution.

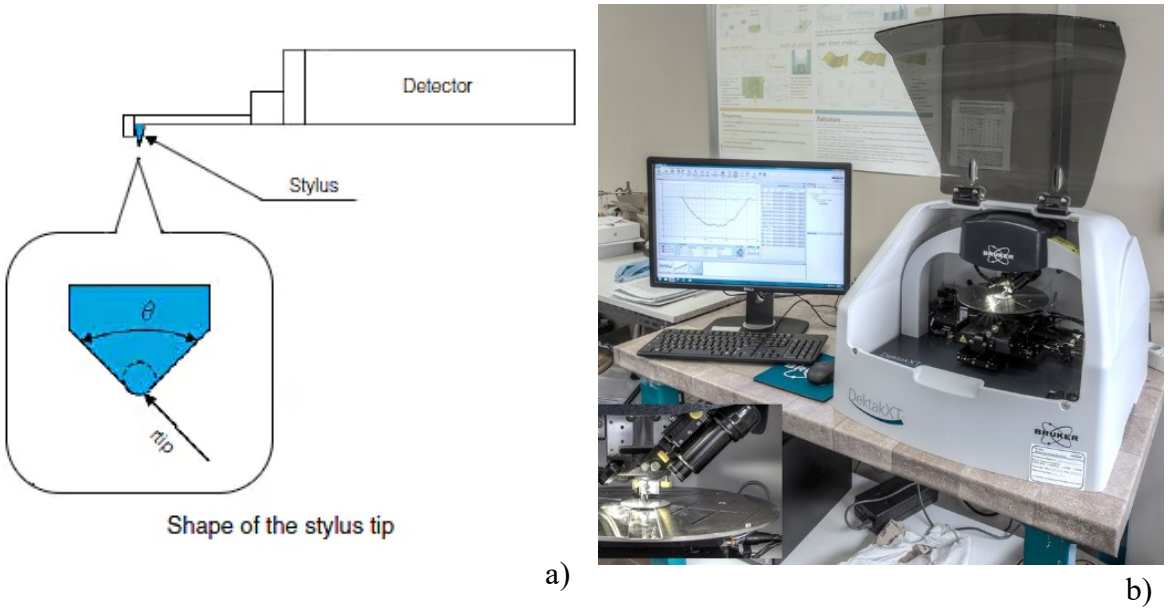

Figure 4.4: a)Stylus tip of the profilometer; b) Profilometer used at ICMATE Laboratory

4.4 ICP-MS: Inductively Coupled Plasma-Mass Spectrometry

Inductively coupled plasma mass spectrometry (ICP-MS) is an analytical technique utilized for the precise measurement of trace elements in fluid samples. It operates by employing an argon (Ar) plasma, known as the ICP, to convert the sample into ions, which are subsequently quantified using a mass spectrometer, referred to as the MS. In contrast to inductively coupled plasma optical emission spectroscopy (ICP-OES), where the emitted light from elements passing through the plasma is measured, ICP-MS directly quantifies ions.

ICP-MS comprises six essential components: the sample introduction system, the ion source (ICP), the interface, ion optics, the mass analyser (typically a scanning quadrupole mass filter), and the detector.

The process begins with liquid samples being nebulized within the sample introduction system, creating a fine aerosol that is then transported into the argon plasma. In the high-temperature plasma, the sample is atomized and ionized, resulting in the generation of ions. These ions are subsequently extracted through the interface region and directed into a series of electrostatic lenses, known as the ion optics. The ion optics serve the purpose of focusing and guiding the ion beam into the quadrupole mass analyser. Within the mass analyser, ions are separated based on their mass-to-charge ratio (m/z), and these ions are subsequently quantified at the detector.

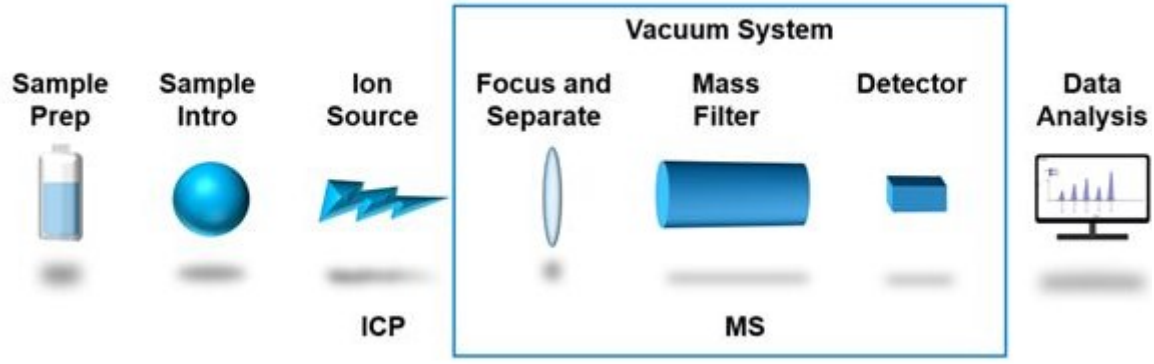

Figure 4.5: The main components of an ICP-MS instrument

In this work of thesis, trace metal analysis was performed using an inductively coupled plasma-mass spectrometry (ICP-MS) Agilent Technologies 7700x system (Agilent Technologies International, Santa Clara, CA, USA), a high performance single quadrupole ICP-MS and shown in Figure 4.6. ICP-MS analyses were conducted by the Chemical Science laboratory of Padua University. The main components (Figure 4.5) of a single quadrupole ICP-MS are following described:

1. **Samples introduction:** liquid samples are delivered to a nebulizer where they are transformed into a fine aerosol mist by a stream of argon gas. Larger droplets are removed in a spray chamber, while the smaller droplets are carried by the argon gas flow into the ICP plasma torch;
2. **ICP plasma ion source:** the plasma, primarily composed of argon, flows through a quartz tube. A Radio Frequency (RF) generator provides energy to the argon gas through a coil wrapped around the exterior of the quartz tube, generating the plasma;
3. **Vacuum interface:** The plasma ion source and the quadrupole mass spectrometer are separated by a vacuum interface. This component facilitates the transfer of ions from the plasma to the mass spectrometer. It typically comprises a series of cooled metal plates or "cones" with small openings that permit ion passage;
4. **Ion focusing and separation:** After passing through the interface cones, ions are focused into a narrow beam using an ion lens. The lens consists of multiple metal plates with adjustable voltages applied to them. Positively charged ions are repelled by positively charged plates, while negatively charged plates attract ions. Various voltage combinations on these lens plates steer and focus the ions. The ion lens also separates ions from neutral particles and photons emitted from the plasma, preventing background signal interference. Neutrals and photons are in this way removed from the ion beam;
5. **Collision-reaction cell (CRC):** spectral overlaps caused by unwanted ions that have the same mass as the ions targeted for analysis in ICP-MS. Commonly, molecular ions contribute to spectral overlaps in ICP-MS. The CRC is composed of an ion guide that can be pressurized using a gas. The strategy for eliminating interferences depends on the specific gas introduced into the cell and falls into two main categories: collision and reaction modes;
6. **Mass spectrometer (MS):** the ICP-MS Agilent 7700x is equipped with a quadrupole mass spectrometer that filters ions based on their mass-to-charge ratio (m/z). This component consists of two pairs of rods with opposite pairs connected to separate electrical supplies. An electric field is applied between the rods, defining the "set mass" of ions that can stably pass through the mass filter. Electric fields alternating between the rods disrupt the trajectories of ions with masses other than the set mass, effectively rejecting them from the ion beam;
7. **Electron multiplier (EM) detector:** the EM detector can detect individual ions, enabling the detection of ultra-low concentrations. It utilizes a high-

voltage electrode (dynode) positioned so that ions emerging from the quadrupole collide with the dynode. Each ion striking the first dynode releases one or more electrons from its surface. These electrons then strike subsequent dynodes, releasing more electrons until a cascade of electrons accumulates sufficiently to be recorded as a pulse or "count" by the EM electronics. The EM detector offers an extremely wide dynamic range, spanning around 10 or 11 orders of magnitude;

8. **Data processing:** The detector records counts for each measured mass, and the data analysis software on the instrument control workstation computer processes these counts. For standard quantitative analysis, the software calculates the concentration of each element in unknown samples by comparing the measured counts to those in reference solutions with known concentrations. Typically, several reference solutions or "standards" are measured to generate a calibration plot of counts versus known concentration for each element.

Liquid samples were provided to be analysed by ICP-MS. The instrument was calibrated every time by using ultrapure water spilled from the Chemical Control System at NBTF.

Figure 4.6: ICP-MS instrument employed by UNIPD laboratories

4.5 Calotest Instrument

The Calotest instruments is used to provide quick, simple and inexpensive determination of coating thicknesses. A small crater is ground into a coating with a ball of known geometry. An optical microscope is used to take two measurements across the crater after the Calotest and the coating thickness is calculated using a simple geometrical equation.

$$t = \frac{xy}{d} \qquad \text{Eq. 4.2}$$

where t is the coating thickness, d is the diameter of the sphere, x is the difference between the radius of the crater and radius of the part of the crater at the bottom of the coating and y is the diameter of the crater. In this way Calotest instruments measure the thickness of coatings in a very short time of just 1 to 2 minutes.

For this thesis, Calotest Industrial (CAT²i) – Anton Paar GmbH – Graz – Austria was used.

4.6 Microcapillary Test Method

Microcapillary electrochemical techniques have emerged as a valuable solution to overcome the limitations associated with conventional methods for studying corrosion behaviour. These advanced techniques involve the analysis of significantly smaller surface areas, making them particularly well-suited for in-depth investigations into the mechanisms underlying corrosion. By reducing the area subjected to analysis, microcapillary methods enable the detection of even the slightest disturbances in the passive layer of materials, a critical factor in comprehending the processes involved in corrosion.

The microcapillary method has gained recognition as a prominent approach for conducting studies on Stress Corrosion Cracking (SCC), as exemplified by its implementation by Breimesser et al. [63]. The advantages of employing the microcapillary method can be summarized as follows:

1. **Enhanced Sensitivity**: Microcapillary methods provide heightened sensitivity due to their analysis of smaller surface areas. This increased sensitivity allows for the early detection of corrosion initiation, a phase that is often the most time-consuming and critical aspect in SCC studies. Traditional electrochemical techniques used in SCC research face the challenge of a large surface area in contact with the corrosive solution. In reality, since SCC typically occurs in extremely localized sites during the incubation/initiation phase, detecting and further analysing such sites for a detailed understanding of the SCC initiation mechanism can be quite challenging. Therefore,

reducing the size of the surface area under investigation can significantly improve the early detection of SCC initiation sites compared to conventional testing methods;

2. **Focus on Mechanisms**: In comparison to conventional electrochemical techniques with their larger surface coverage, microcapillary methods place a specific emphasis on the critical crack initiation phase. This specialized focus facilitates a more profound exploration of the mechanisms responsible for SCC, allowing for a more comprehensive understanding of the processes involved;
3. **Native Oxide Layers:** Microcapillary techniques prove particularly effective when studying materials that possess native oxide layers on their surfaces. These oxide layers wield considerable influence over corrosion behaviour, and microcapillary methods enable researchers to closely examine their interactions with the surrounding environment.

In summary, microcapillary electrochemical technique offers a powerful approach for investigating the corrosion behaviour and SCC of materials. Its effectiveness lies in the reduction of the surface area under scrutiny, leading to heightened sensitivity and the ability to detect corrosion and crack initiation at their nascent stages. This precision empowers researchers to gain insights into the mechanisms responsible for these phenomena, which is essential for developing materials with improved corrosion resistance and durability. As a result, microcapillary electrochemical techniques have become the method of choice for mechanistic studies in the field of materials science and corrosion analysis.

The microcapillary facility employed for electrochemical polarization experiments is shown schematically in Figure 4.7. It is characterized with a capillary diameter of 500 µm employing Gamry interface 1010 potentiostat unit. Microcapillary electrochemical polarization measurements were conducted utilizing the standard three-electrode method with the calomel reference electrode (SCE) as the reference and platinum wire with a diameter of 500 µm as the counter electrode. With the aim of eliminating the ohmic drop during the experiments, the distance of the counter electrode was maintained at 5 mm from the surface under test for all experiments. Moreover, to eliminate the risk of crevice corrosion and possible false detections during the electrochemical polarization experiments, silicone-based adhesive was applied to the tip of the capillary and all polarization experiments were conducted after holding the test area in contact with the solution for 30 min [64], [65]. Microcapillary tests were performed by the Industrial Engineering Department at Padua University.

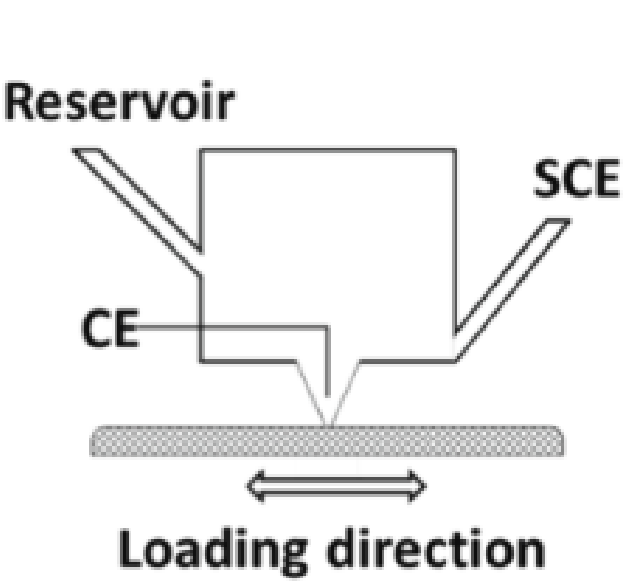

a)

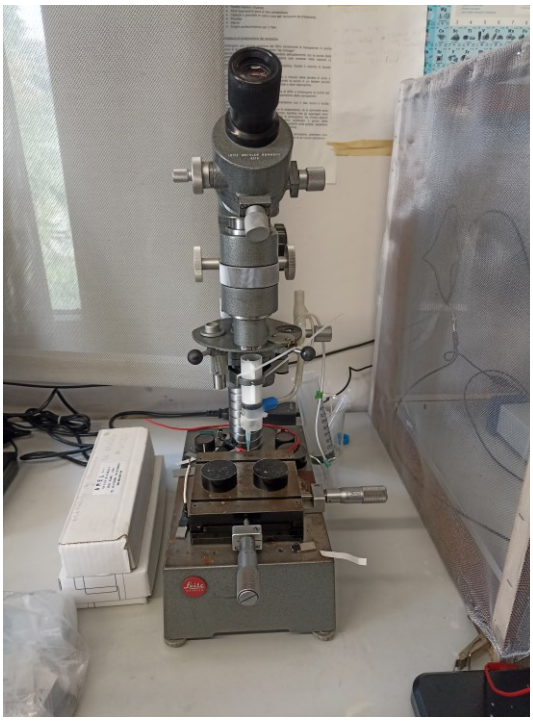

b)

Figure 4.7: a)Schematic view of the microcapillary test setup [64]; b) Photo of the set up

Chapter 5
Metal Release Experiments

The materials employed in the NBTF experiments include stainless steel (304L for piping and 316L for components installed within the vacuum vessel) and copper, primarily utilized for actively cooled components. The connection between SS 316L and copper is achieved through a Vacuum Tight Threaded Junction (VTTJ) where the two metals are threaded into each other using mechanical friction, resulting in the formation of a metallic seal. For a more comprehensive description of this junction, detailed information can be found in the work by P. Agostinetti et al. [46], [66] Additionally, examples of VTTJ mock-ups are provided in Figure 5.1.

This chapter encompasses experiments aimed at gathering empirical data regarding the release rate behaviour of these two metals under two main experimental conditions:

- **Experiment type n.1**: SS and Cu samples exposed individually and coupled (as in VTTJ) in oxidising conditions;
- **Experiment type n.2**: SS and Cu samples exposed individually in both high and reducing environments.

The first set of experiments was exclusively conducted in a high oxygen environment, as this condition is considered the most challenging for both metals, as discussed in Chapter

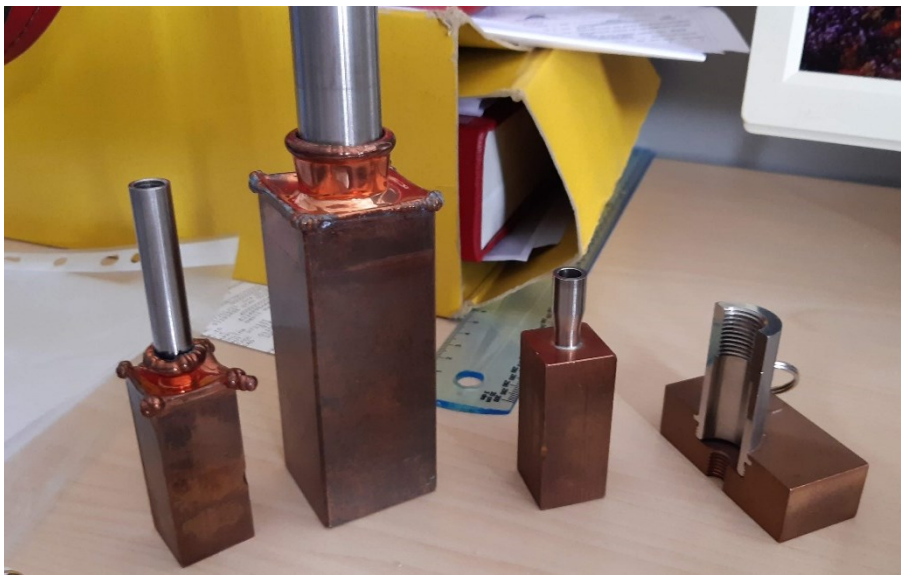

Figure 5.1: VTTJ mock-ups

3: Degradation of Materials in Water. It's crucial to note that galvanic corrosion necessitates different corrosion potentials between the metals in the system, a conductive connection between them, and an electrically conductive electrolyte connecting both metals [67]. The second requirement is met within the VTTJ since Cu and SS are in direct contact. Concerning the first requirement, as stated by the European Stainless Steel Development Association [68], the standard potential of metals merely serves as an indicator of whether corrosion risk needs consideration, whereas the actual potential difference under real operational conditions must be evaluated. Unfortunately, there is no available literature data regarding the corrosion potentials of Cu and SS when immersed in UPW at ambient temperature and under high oxygen conditions. Yahia [69] estimated the Open Circuit Potential (OCP) of SS 316L in demineralized water to be around -41.8 mV, while Rios et al. [70] determined the OCP of copper at 23°C in drinking tap water to be -10 mV. All the OCP were calculated vs. Saturated Calomel Electrode (SCE). Given that the environments in which the metals were exposed during the metal release experiments are closed to the ones stated in the previous articles of Yahia [69] and Rios [70], it is reasonable to assume that copper and stainless steel have very similar corrosion potentials, even in ultrapure water. However, this rough data can only provide a general idea of the galvanic potential risk and whether preventive measures should be considered. Regarding the electrolyte, UPW is a resistive medium. These conditions suggest that galvanic corrosion between copper and stainless steel is not a substantial risk. Unfortunately, prior metal release experiments have demonstrated that both metals experience general corrosion in stagnant and resistive media like UPW [58], [71]. The released ions from exposed metals increase water conductivity, altering the electrolyte characteristics. Molander highlights that galvanic corrosion between copper and stainless steel cannot be ruled out in ITER systems [50].

As for the second set of experiments, the investigation into two specific environments, namely the oxidizing atmosphere referred to as "High Oxygen" (HO) and the oxygen-free atmosphere termed "Low Oxygen" (LO), was motivated by the fact that oxygen is one of the most critical factors influencing corrosion and the release of metallic ions into the water. The operation of NBTF PCs had revealed the presence of air within the cooling circuits, leading to the exceeding of oxygen concentration limits (see Section 6.5). Specifically, the nominal operating conditions of the system were expected to maintain oxygen concentration levels below 50 ppb, although this value is exceeded during normal operations.

In this chapter, an investigation into the general corrosion behaviour of copper and stainless steel in ultrapure water is presented. Metal release tests were conducted under the experimental conditions as previously outlined. Additionally, preliminary tests for Stress Corrosion Cracking initiation are outlined to confirm the findings obtained from the metal release tests. These latter tests were executed using the microcapillary technique.

5.1 Materials and Methods

5.1.1 Materials

In both previously mentioned experimental conditions, stainless steel and copper were used.

Stainless steel plates of type 316L were kindly provided by Westinghouse - Mangiarotti S.p.S. Monfalcone (GO) and the metal bulk composition is reported in Table 5.1. These stainless steel plates were used to cut SS samples exposed alone in Experiment type n.1 and Experiment type n.2.

Oxygen Free High Conductivity Copper samples (99.9%) were chosen for this experiment as they are the same type of material used to make the VTTJ mock-ups.

VTTJ samples were cut from the VTTJ mock-ups already available at Consorzio RFX and shown in Figure 5.1. Regrettably, the material datasheet originally provided by the suppliers was no longer accessible for the SS side of the VTTJ. Previous correspondences with the supplier indicated the usage of SS316L for the VTTJ mock-ups.

Ultrapure Water was collected from the Chemical Control System I (CCS-I) that supplies UPW for SPIDER and MITICA PCs. Water characteristics at tapping are:

- Conductivity of 0.055 [µS·cm-1],
- pH of 6.5 – 7.5,
- Dissolved oxygen of ≤ 50 ppb.

Table 5.1: Nominal bulk alloy composition of stainless steel grade 316L based on supplier information (wt %)

C	***Si***	***Mn***	***P***	***S***	***Cr***	***Ni***	***Mo***	***Cu***	***Co***	***Nb***	***N***
≤0.035	≤0.90	≤2.50	≤0.025	≤0.025	18.00 – 20.00	12.00 – 14.00	2.00 – 3.00	≤0.2	≤0.10	≤0.1	≤0.1

5.1.2 Methods

ISO 17294-1 and ASTM D4453-17 standards were used to prepare samples and clean all the equipment.

5.1.2.1 ASTM D4453-17: Handling UPW Vessels and Vials Procedure

The ASTM D4453-17 for handling high purity water samples was used to handle and prepare all ultrapure water vessels and vials used for all the experiments. This procedure comprises:

1. Filling vials with diluted HCl at 50% dilution
2. After 2 days, wash the vials with UPW one time
3. Fill vials with diluted HNO3 at 50% dilution
4. After 2 days, wash one time with UPS at full level
5. Wash the vials with UPW other two times at 1/3 of their volume
6. Fill vials with water

Store them in the fridge

5.1.2.2 ISO 17294-1: Sampling Procedure

The water sampling process between consecutive time intervals proceeded as follows: after immersing the samples for the designated duration, 10 ml water samples were collected using Falcon tubes. These samples were then analysed using ICP-MS to determine the concentration of released metallic ions. Subsequently, the water in which the samples had been immersed, and the one used for the blank, were removed from the vessels. The vessels were then refilled with 50 ml of clean ultrapure water for the same immersion duration as the next scheduled interval. This described procedure was carried out for each of the specified time intervals.

The adopted sampling procedure adhered to the standards ISO 17294-1 outlined in reference [72] from the bibliography. According to this reference, 0.5 ml of a 10% dilute HNO_3 solution was added to each 10 ml water sample for sample stabilization.

5.2 Sample Preparation and Experimental Conditions

5.2.1 Samples Preparation

In order to have surface-water volume ratio, in the two type of experiments, samples were cut with different dimensions.

- **Experiment type n.1: Coupling of Copper and Stainless Steel in Oxidizing Environment**

Stainless steel samples (Figure 5.2a) were crafted to dimensions of 9.7 x 2 x 12 cm, resulting in a total surface area of approximately 3.2 cm^2. Similarly, the copper samples (Figure 5.2b) were cut with a size of 2 x 2.22 x 0.5 cm (total surface area of approx. 13.1 cm^2). Samples measuring 5.7 x 34 x 7 mm were cut from the VTTJ mock-ups (Figure 3.6) to ensure that they had an equivalent surface area of copper and stainless steel exposed to water, matching the surface area for both metals of the previous samples (Figure 5.2c). The S/V ratio was kept constant for both the metals in all vessels, specifically 6.39 1/m for stainless steel and 26.2 1/m for copper, in order to better compare the release of the metals.

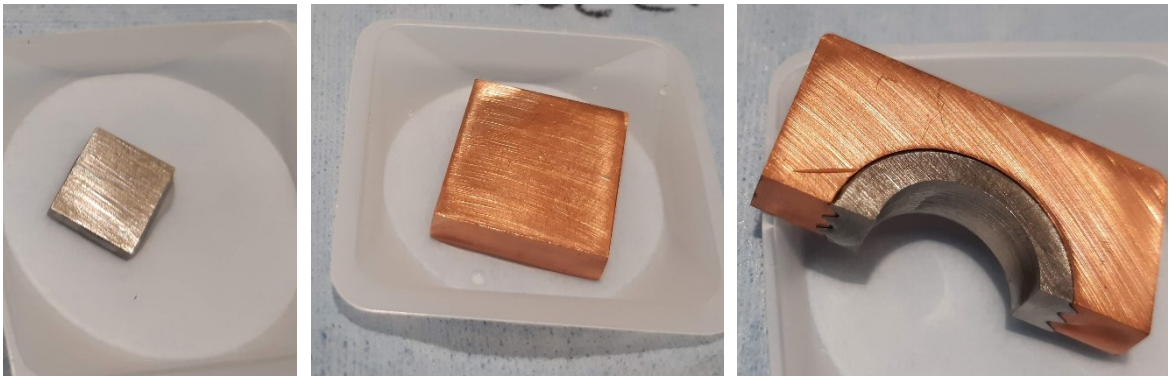

a) b) c)

Figure 5.2: Experiment type n.1 samples a) SS sample; b) Copper sample; c) VTTJ sample before to the immersion test

- **Experiment type n.2: Copper and Stainless Steel Exposed Alone in Oxidizing and Reducing Environment**

Stainless steel samples (Figure 5.3a) were cut with a size of 2.7 x 0.85 x 1.2 cm (total surface area of approx. 13.1 cm^2). Copper samples (Figure 5.3b) were prepared with a size of 2 x 2.22 x 0.5 cm (total surface area of approx. 13.1 cm^2). The S/V ratio was kept constant for both the metals in all vessels, 26.2 1/m for copper and stainless steel, in order to better compare the release of the metals.

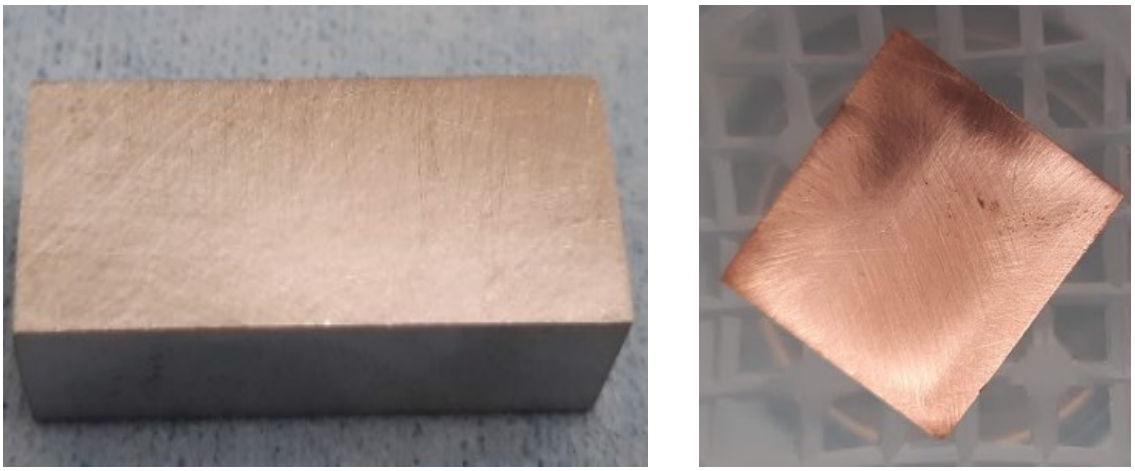

a) b)

Figure 5.3: Experiment type n.1 samples a) SS sample; b) Copper sample

In both types of experiments, grinding was conducted to attain a roughness level similar to that of actual water channel surfaces. This process involved standard metallographic preparation using SiC paper with a grit size of P120 for stainless steel and P600 for copper. The resulting average roughness value (Ra) for both metals was approximately 0.4 µm. Roughness measurements were performed using a stylus profilometer (DektakXT®, Bruker, Germany), described in (Section4.3).

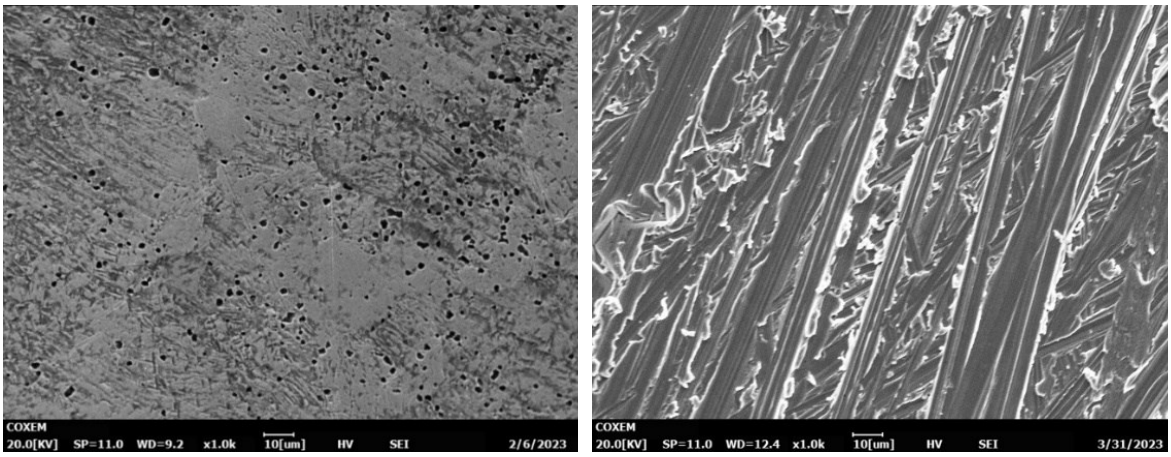

a) b)

Figure 5.4: SEM image of copper samples before and after grinding process

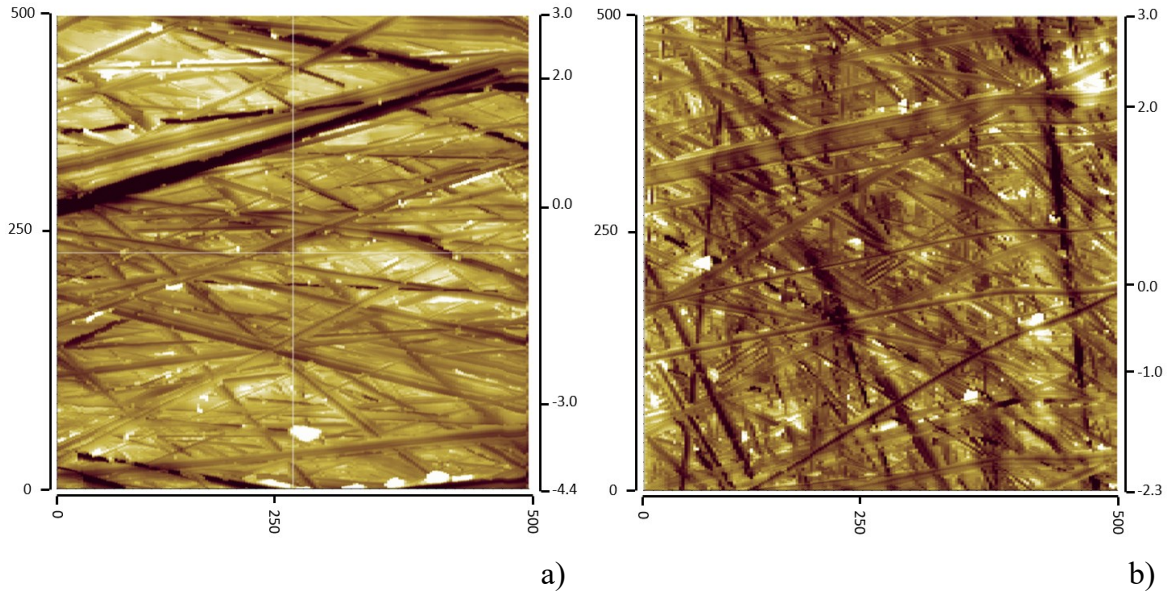

Figure 5.5: a) SS sample map roughness; b) Cu map roughness

5.2.2 Experimental Conditions

The experiments were conducted under room temperature conditions, approximately at T≅25 °C. The immersion of the test samples in ultrapure water was carried out under stationary conditions in both types of experiments. In the high oxygen environment, copper and stainless steel were exposed both alone and coupled, mimicking the VTTJ configuration, to investigate if coupling has an impact on the metal release process compared to individual base metals. These samples were subjected to the same experimental conditions. In the low oxygen environment, samples of the two materials were solely exposed individually.

Regarding temperature considerations for the experiments conducted at around T≅25 °C, it's worth noting that most primary circuits of the NBTF cooling system are designed to operate within a temperature range of 20 - 45 °C. [18].

The decision to conduct experiments under stagnant conditions is based on the discovery of an area within a VTTJ mock-up where water circulation is impeded (Figure 5.6).

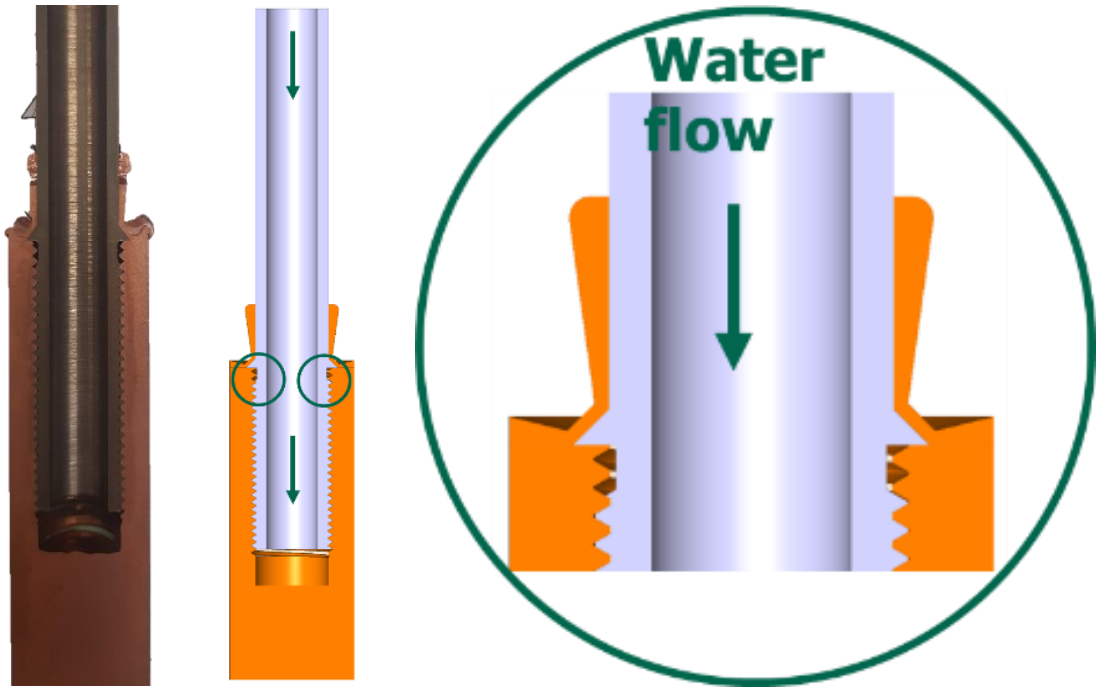

Figure 5.6: a) VTTJ section; b) VTTJ cad section; c) VTTJ zoom in the stagnation area

This finding was further investigated by creating a small hole (Figure 5.7a) in the vicinity of the empty nut screw zone (highlighted with two green circles in Figure 5.6b) beneath the mechanical interference region. VTTJ samples, which had previously passed the pressure and leak test as described in P. Agostinetti et al. [66], were connected to a manual water pump (Figure 5.7b). Water began to flow from the hole at 1.5 barg (Figure 5.7c), indicating that water can reach the empty zone by flowing up the screw even at very low pressure. It's important to note that NBTF cooling circuits are designed to operate under nominal conditions of up to 20 bar. Therefore, this zone can be considered a stagnant area where copper and stainless steel are coupled. It's reasonable to assume that similar stagnant regions may exist elsewhere in the NBTF circuit due to mechanical interference regions.

Prior to immersion, the samples underwent an ultrasonic cleaning process. They were first cleaned with acetone for 5 minutes, followed by a 5-minute cleaning with ethanol. After cleaning, the samples were dried before being placed in 50 ml of ultrapure water (UPW).

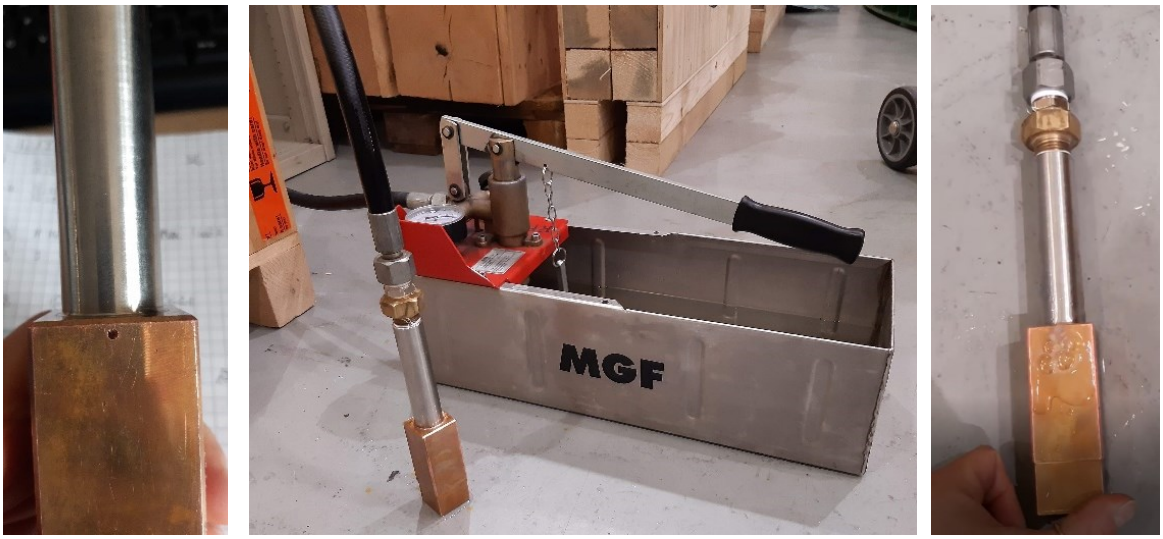

a) b) c)

Figure 5.7: a) Hole made on VTTJ Cu side to detect water stagnation area; b) Test set up; c) Water leak from the hole

Independent trials were conducted at different time intervals. In Experiment type 1, where Cu and SS were coupled, a longer exposure time was employed (3 hours, 24 hours, 1 week, 4 weeks, 5 weeks, and 6 weeks) to investigate prolonged exposure effects. For Experiment type 2, which involved samples exposed alone, shorter exposure durations (3 hours, 24 hours, 1 week, and 4 weeks) were considered. The water in the vessels was replaced at each sampling step to prevent any saturation effects from the ions released into the solution.

Metal releases in solution (µg/cm²) were calculated as follows:

$$released\ ions\ \left[\frac{\mu g}{cm^2}\right] = 10^{3\cdot}\frac{ions\ concentration\ [ppb] * water\ volume\ [cm^3]}{sample\ surface\ area\ [cm^2]} \qquad \text{Eq. 5.1}$$

Trace metal analysis of Cr, Mn, Fe, Co, Ni, Mo and Cu released were performed using the Inductively Coupled Plasma-Mass Spectrometry (ICP-MS) Agilent Technologies 7700x system (Agilent Technologies International, Santa Clara, CA, 95051, United States), described in Section 4.4.

The experiments conducted in an oxidizing atmosphere were carried out at the NBTF chemical laboratory. For environmental control, a molecular filtration chemical hood M900 (Figure 5.8a) was employed. This setup allowed the experiments to be conducted under the same oxygen conditions as typically found in the atmosphere. The measurement of Dissolved

Oxygen (DO) in water was not performed, as it was assumed to have reached saturation, approximately 8.3 mg/l, due to the experimental procedure conducted in ambient atmosphere.

Conversely, the reducing atmosphere conditions were achieved using the UNIlab LMF Glove Box (Figure 5.8b) at the ICMATE Institute. This glove box completely isolates the working environment, ensuring an oxygen and water content inside of less than 1 ppm. DO in water was measured by a fiber optic sensor connected to a pocket oxygen meter.

To prevent any potential contamination of the ultrapure water, the Falcon tubes used for the release experiments were cleaned using HCl, HNO_3, and UPW, following the ASTM D4453-1 standards as described in Section 5.1.2.1 The nitric acid used (67%–69% HNO_3) was SuperPure (SpA) quality purchased from Romil Ltd. (Romil Ltd., The source, Covent drive, Waterbeach, Cambridge, U.K.) to limit any trace metal cross contamination from the nitric acid.

ISO 17294-1 procedure was used to prepare the samples. The sampling procedure was described in Section 5.1.2.2.

a)

b)

Figure 5.8: The working environments in which the experiments were conducted (a) M900 chemical hood at NBTF used for experiments in HO, providing a controlled oxygen atmosphere.(b) UNIlab LMF Glove Box from the ICMATE Institute used for experiments in LO, enabling work in a controlled oxygen environment.

5.3 Experimental Results

Experimental results are going to compare SS and Cu when exposed alone and coupled in HO (Experiment type n.1, Section 5.3.1); and SS and Cu when exposed alone in both LO and HO conditions (Experiment type n., Section 5.3.2). A comparison of copper oxides formed in oxidizing and reducing conditions is presented in Section 5.3.3. Section 5.3.4 reports preliminary Stress Corrosion Cracking initiation tests performed on Cu and SS samples still exposed to both Experiment type n.1 and n.2 conditions. The intention is to establish a comparison with the results obtained from the metal release tests.

5.3.1 Experiment Type n.1: Coupling of Copper and Stainless Steel in Oxidizing Environment

Figure 5.9 illustrates the release rates in [$\mu g/cm^2$] for all metals in samples that were either exposed "alone" or "coupled" in VTTJ. In the case of SS samples, the release rates of Fe and Cr are higher when the samples are exposed alone compared to when they are coupled in VTTJ. However, when it comes to cobalt (Co) and manganese (Mn), their release rates are higher when samples are coupled in VTTJ. Ni, Co, Mn in VTTJ shows a peak at the 4-week mark of 0.037 $\mu g/cm^2$, 0.018 $\mu g/cm^2$ and 0.051 $\mu g/cm^2$. This unusual behaviour might be attributed to undetected factors such human errors during the sampling process, or the possibility of vessel movement leading to water mixing between the 2nd and 4th weeks of sampling. Up until this particular sampling point, the release patterns of Ni, Co, and Mn in SS samples when exposed alone and in VTTJ samples were nearly identical. Molybdenum (Mo) shows comparable trends for SS samples exposed alone or coupled.

To gain further insights into these differences in release rates, the scanning electron microscope (SEM) equipped with Energy Dispersive X-ray Spectroscopy (EDS), described in Section 4.1, was used to analyse the bulk microstructure of the steel. This analysis aimed to have a semi quantitative analyses of the bulk composition and determine if the variations in ICP-MS results could be attributed to differences in bulk composition in SS alone and SS in VTTJ samples. As detailed in Section 5.1 “Materials ”, VTTJ samples were derived from pre-existing VTTJ mock-ups, illustrated in Figure 5.1. Regrettably, the SS used for the mock-ups was not sourced from the same company that supplied the SS plates from which the SS "alone" samples were obtained.

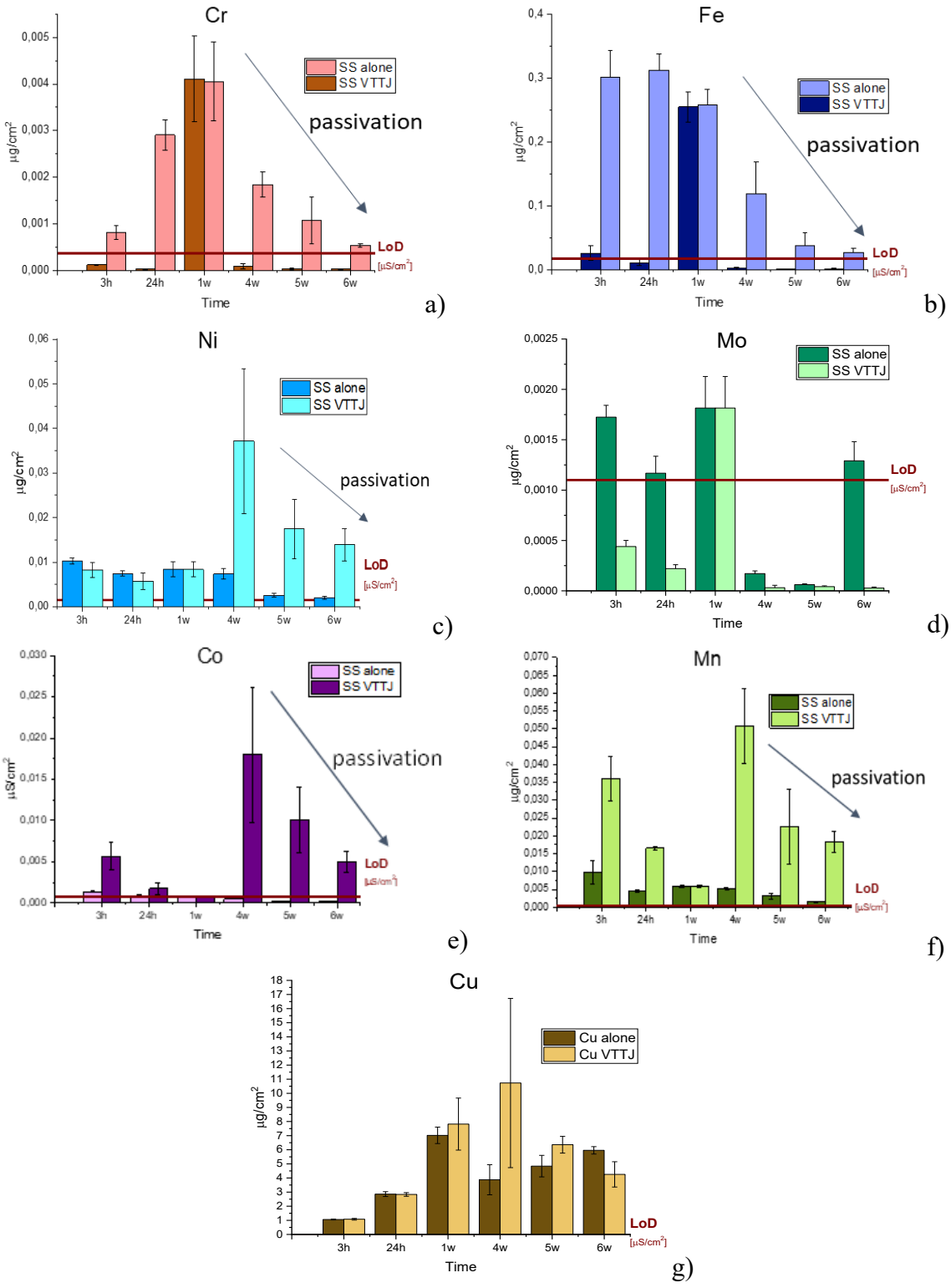

Figure 5.9: [µg/cm²] graph of Cr (a), Fe (b), Ni (c), Mo (d), Co (e), Mn (f), Cu (g) exposed alone and coupled in VTTJ samples

Table 5.2: SS bulk composition for 316L exposed alone and 316L in VTTJ samples. Composition measured with EDS points

	SS 316L "alone"		SS 316L in VTTJ	
Elements	*Weight %*	*St. Dev*	*Weight %*	*St. Dev*
SiK	0.50	0.08	0.37	0.05
MoL	1.37	0.11	0.34	0.02
CrK	20.59	0.10	18.57	0.24
MnK	1.18	0.06	1.42	0.07
NiK	9.56	0.53	7.09	0.04
FeK	70.65	0.55	68.23	0.11

The composition of stainless steel after P120 grinding is presented in Table 5.2, including weight percentages and weight standard deviations for SS exposed alone and SS in the VTTJ mock-ups. The metals with notably different compositions are Cr, Fe and Mo. SS 316L samples exposed "alone" exhibit a higher Mo content of approximately one percentage point, while SS 316L in "alone" samples contain a higher Fe and Cr content of about two percentage points. The higher Fe and Cr release in SS alone specimens can be linked to a bulk composition difference. Whereas, the elevated Mo content in SS 316L from Mangiarotti Spa may account for the slightly higher initial Mo release in the SS alone samples. However, it is important to emphasize that this release is in such proximity to the Limit of Detection (LoD) of the ICP-MS that any disparity in the release rate of Mo in SS samples when exposed individually can be considered negligible compared to the Mo release in SS specimens when they are exposed in conjunction with Cu. It is important to underscore that SEM-EDS analyses might have underestimated the Mo content in the SS VTTJ samples. The low Mo content could be attributed to measurement errors or the limitation of SEM-EDS analyses in providing precise quantitative data. Unfortunately, this was the only available analysis for obtaining a rough estimate of the element quantity.

Regarding copper, the metal release rates are comparable for both types of samples, highlighting that no significant adverse effects on metal release are observed due to the coupling of SS and Cu.

Summarizing, it appears that the SS alone sample is slightly more prone to releasing Cr and Fe, but further investigation is needed before drawing definitive conclusions.

5.3.1.1 Surface Passivation after Six Weeks Exposure

Throughout the experiment, Cu samples underwent a gradual transformation, becoming covered by a black oxide layer identified as tenorite through X-ray diffraction (XRD) analysis (refer to Figure 5.10). The XRD analyses are reported in Section 5.3.3. In contrast, no noticeable oxidation occurred on the surfaces of SS samples.

Figure 5.9 emphasizes that all SS elements, with the exception of molybdenum (Mo), exhibited a decreasing trend in release rates after a specific sampling time for both sample types. Conversely, copper showed an almost constant release trend after the first week of sampling. Molybdenum release consistently remained close to the limit of detection.

The influence of surface passivation on metal releases was examined by subjecting all these samples to UPW for an additional 3 hours following the completion of the 6-week sampling period. The decision to use a 3-hour exposure time was made in order to facilitate a comparison of the metal release data obtained during this post-exposure period with the data collected after the initial 3-hour immersion in UPW and reported in Figure 5.9. Metal releases after 3 hours with respect to the releases detected after the first 3 hours of exposure are reported in Figure 5.11.The quantities of SS alloy constituents released upon repeated exposure after 3-hours were reduced for both sample types (alone and in VTTJ). This reduction indicates surface passivation in UPW under these experimental conditions. These results align with literature findings for the 316L stainless steel grade, which demonstrate a reduction in metal release upon repeated exposures to UPW [71]. Metal releases value for first 3h and 3h after 6 weeks exposure are reported in Table 5.3 for SS and Cu elements exposed alone and in VTTJ.

In contrast, copper did not exhibit passivation behaviour, and metal release after repeated exposure remained comparable to the levels measured during the initial three-hour exposure. The oxide layer formed on the surface of copper did not prevent further release of metal ions.

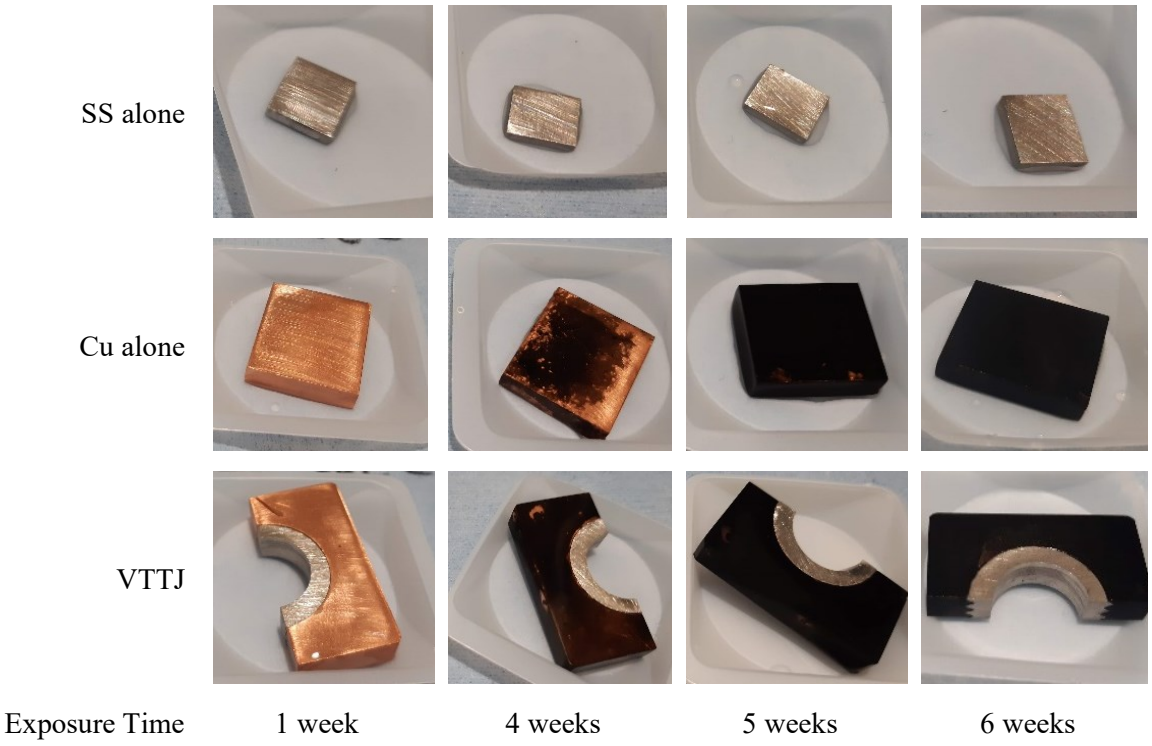

Figure 5.10: Time evolution of surface aspect during the sampling points

Table 5.3: Average metal releases expressed in [µg/cm^2] and St. Deviation of SS and Cu elements exposed alone and in VTTJ

	Samples "alone"				**Samples in VTTJ**			
Elements	*3 h*		*3 h after 6 w*		*3 h*		*3 h after 6 w*	
	Average [µg/cm^2]	St. Dev	Average [µg/cm2]	St. Dev	Average [µg/cm2]	St. Dev	Average [µg/cm2]	St. Dev
Cr	8.08E-4	1.51E-4	4.04E-4	2.73E-4	1.20E-4	1.15E-5	5.27E-5	3.46E-5
Mn	9.76E-3	3.28E-3	1.12E-3	5.01E-4	3.60E-2	6.08E-3	5.06E-4	9.03E-5
Co	1.27E-3	2.94E-4	2.69E-5	3.27E-5	5.67E-3	1.70E-3	3.50E-5	5.39E-6
Fe	3.00E-1	4.32E-2	7.52E-3	4.04E-3	2.59E-2	1.11E-2	4.52E-3	7.05E-3
Ni	1.03E-2	7.00E-4	5.00E-4	9.98E-5	8.27E-3	1.68E-3	8.76E-5	4.85E-5
Mo	1.72E-3	1.18E-4	3.2E-4	3.18E-7	4.39E-4	6.06-5	1.40E-4	1.81E-4
Cu	1.06	3.44E-2	1.56	1.21E-1	1.08	5.86E-2	1.61	2.69E-1

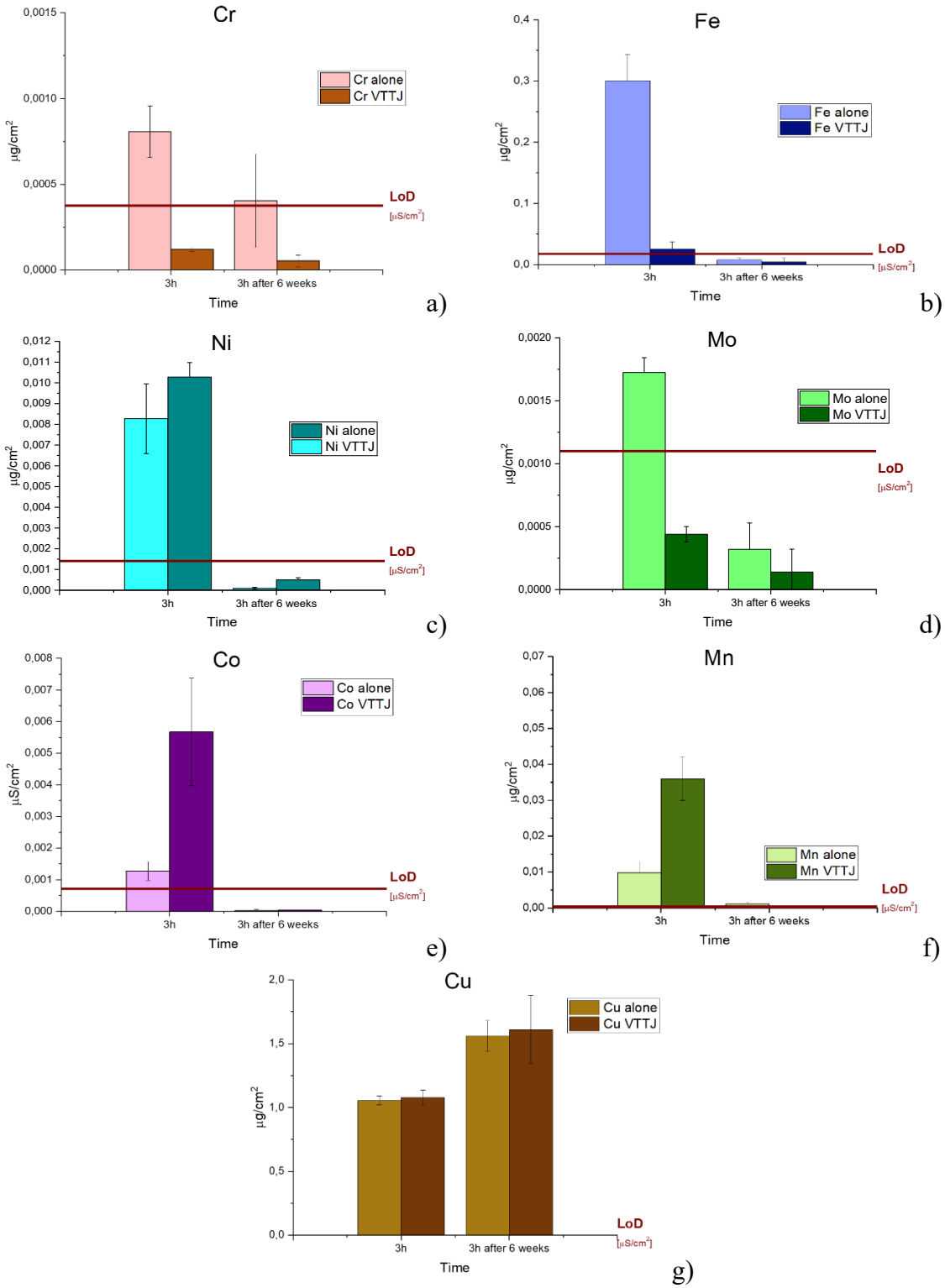

Figure 5.11: [µg/cm²] graph of Cr (a), Fe (b), Ni (c), Mo (d), Co (e), Mn (f), Cu (g) exposed alone and coupled in VTTJ samples after 3.5h of exposure compared to the first 3h of exposure

5.3.2 Experiment Type n.2: Copper and Stainless Steel Exposed Alone in Oxidizing and Reducing Environment

Figure 5.12 reports the metal ions released from stainless steel and copper samples in [µg/cm^2] in HO and LO conditions.

With regards to SS elements (Figure 5.12a, Figure 5.12b, Figure 5.12c, Figure 5.12d, Figure 5.12e and Figure 5.12f), it is clear that a passive layer is formed on metal surface in oxidizing environment: the release rate calculated after 3h of immersion decreases very fast for all the elements. Specifically, Mo concentrations go below the Limit of Detection (LoD) already after 1 week. The highest passivation rate is obtained for Mo and Fe, as observable in the release plots [µg/cm^2]:

After 3h of immersion:

- 1.24E-03 µg/cm^2 released or Mo
- 4.48E-01 µg/cm^2 released for Fe

After 4 weeks:

- 4.95E-05 µg/cm^2 for Mo
- 3.09E-02 µg/cm^2 for Fe.

In a reducing environment, the SS metal release rate does not decrease as the sampling points increase because in the absence of oxygen, the passivation layer is not formed, as shown in SCC results in Section 5.3.4. Further exploration into the release of ions from SS in a low oxygen (LO) environment will involve the examination of pre-passivated samples. This approach allows for a focused investigation into the effects of exposing SS samples to a reducing environment after they have developed a protective passivating layer on their surface. Currently, different procedures for pre-passivating the samples are under consideration, and guidance from ASTM A967/A967M-17 [73] will be valuable in identifying the most appropriate and effective pre-passivation method for the surface.

In the oxidizing atmosphere, Figure 5.12g illustrates an increasing trend in the release of copper ions into the water as the immersion time progresses, eventually reaching a peak release value of 6.69 µg cm^{-2}. From the trend of the results shown in the graph, it can be observed that the oxide formed on Cu during the immersion in UPW does not play a protective (passivating) role over time. In fact, as the immersion hours' progress, the release of copper ions into the water is continuous and increasing. Moreover, since the experiments were conducted at room temperature and atmospheric pressure, it is possible to calculate the concentration of dissolved oxygen ions in water at saturation, commonly referred to as "Dissolved Oxygen" (DO), which corresponds to the maximum achievable concentration of oxygen dissolved in water, estimated to be around 8.3 mg/l.

Conversely, in the reducing atmosphere (LO), the release of Cu ions (Figure 5.12g) does not show a decrease with prolonged immersion time, displaying a contrasting pattern compared to the HO atmosphere. The concentration of Cu ions, which were 0.20 μg cm^{-2} after 3 hours of immersion, remains relatively stable even at the fourth week, with a measured ion concentration of 0.13 μg cm^{-2}. These findings can be rationalized by considering that in an oxygen-depleted environment, the low oxygen concentrations effectively inhibit the oxidation reaction, establishing an environment less favourable to copper corrosion. This reduced propensity for copper oxidation in the LO environment is not only reflected in the low concentrations of Cu ions released into the water but is also evident from the surface photos of the samples taken at the conclusion of the immersion period (Figure 5.13).

Regarding the dissolved oxygen content in water, deoxygenation of the water was achieved by introducing a bottle of ultrapure water the day before each new immersion. Due to the concentration gradient of oxygen between the Glove Box and the ultrapure water, oxygen in the water disperses into the Glove Box atmosphere according to Henry's law (Eq. 2.5) and is subsequently removed from the environment through purification systems. DO was measured with a fiber optic sensor at every sampling time point at the end of the immersion and before immersing samples again in UPW for the next sampling time point. The dissolved oxygen concentration in the fresh UPW, before sample immersion, was below the nominal threshold of 50 ppb for each sampling time. During the samplings, new oxygen measurements were taken at the end of the immersion, noting that at 3 hours and 24 hours, the measured ppb values were above 500 ppb, while in subsequent samplings, the quantity remained below 50 ppb. The presence of oxygen in the initial samplings, despite the samples being immersed in deoxygenated water, was attributed to the oxygen trapped both on the sample surfaces and the vessel walls, which was subsequently released into the solution in the early stages of the experiment.

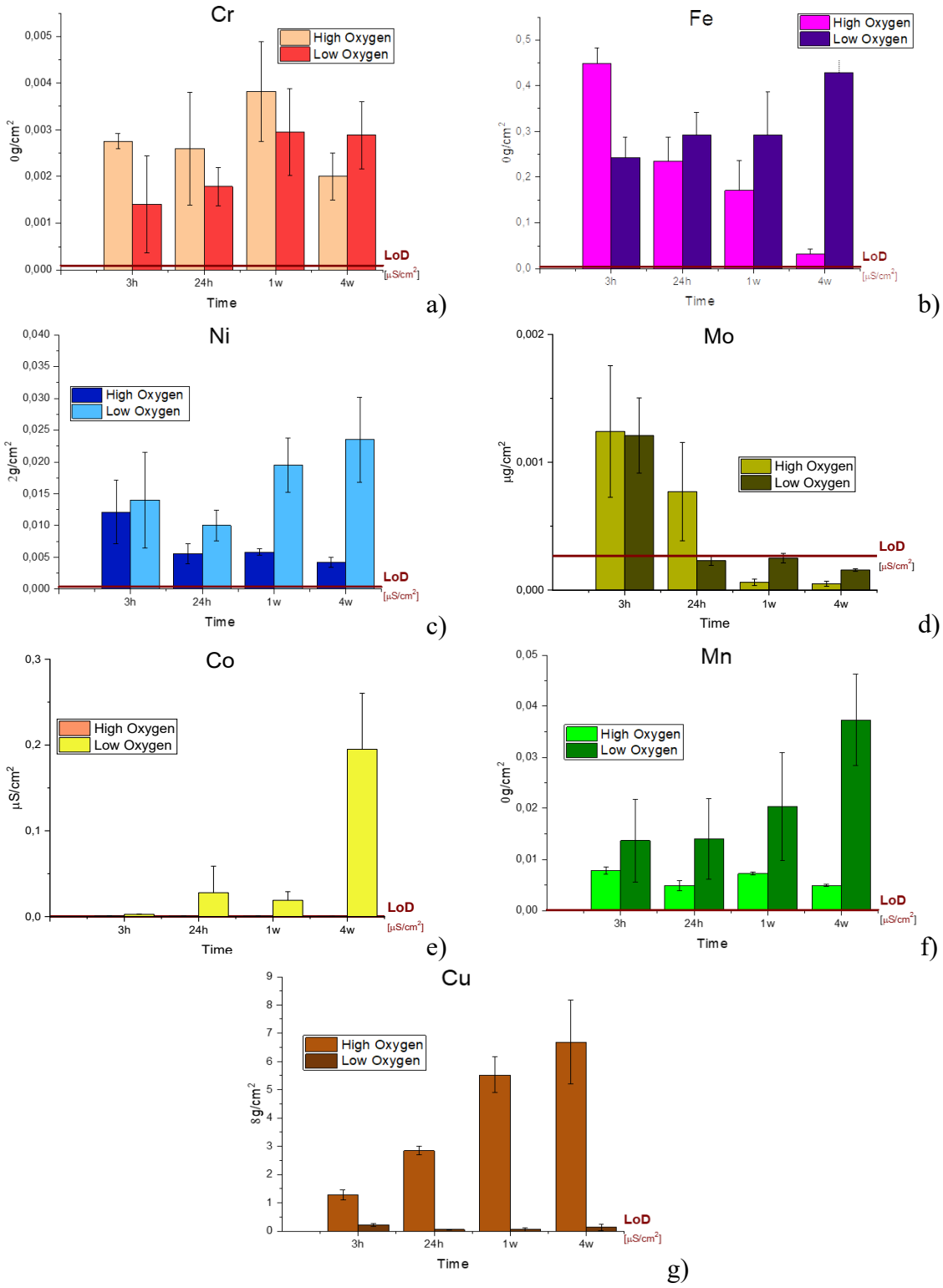

Figure 5.12: [µg/cm^2] graph of Cr (a), Fe (b), Ni (c), Mo (d), Co (e), Mn (f), Cu (g) exposed in LO

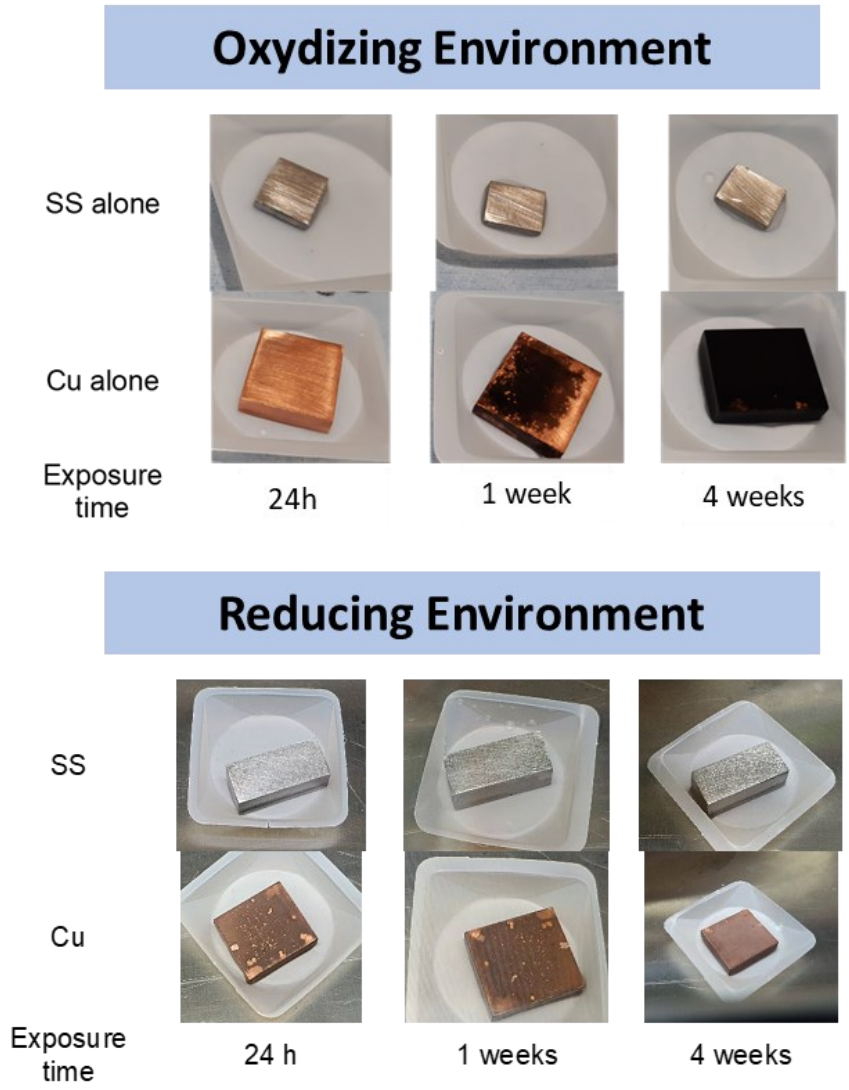

Figure 5.13: Cu and SS time evolution of surface aspect during the sampling points in HO and LO.

5.3.3 Copper Oxide Analyses

Various details and studies on Stainless Steel passivation in ultrapure water are discussed by C. Gasparrini [74], W. Niu [75], N. Mazinanian [76] and X. Dong .[77]. Consequently, the focus shifted to the examination of the surface passivation of copper when exposed to ultrapure water, as this subject has not received extensive treatment and development in the existing literature.

The quantity of dissolved oxygen, as illustrated in Figure 5.14, played a role in the development of various copper oxide types. In the presence of an oxidizing atmosphere, a

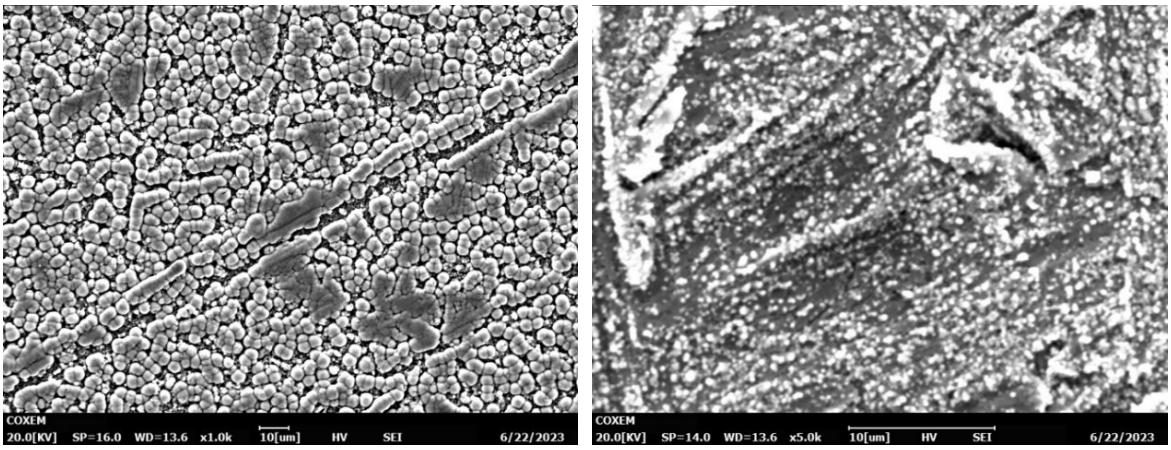

a) b)

Figure 5.14: SEM images of Cu oxides on a) HO environment, b) LO environment

dense, black oxide was generated. In contrast, when exposed to a reducing atmosphere, opaque brown deposits with a lighter coloration formed. SEM images that depict the morphological characteristics of copper's oxidized surfaces in both HO and LO environments are presented in Figure 5.14.

By comparing the SEM images obtained after the immersions (Figure 5.14) with those taken on the initial samples (Figure 5.4), where the streaks left by the lapping process were evident, it can be observed that over time, the corrosion of the sample's surface led to the formation of an irregular oxide layer characterized by a series of distinguishable agglomerates of more or less rounded shapes. Nevertheless, the imprints from the previous lapping process are still discernible after immersion, though to a lesser degree.

In HO environment, spherical microstructures were formed. The XRD analyses revealed that the oxide is mainly Copper (II) oxide, with the formula CuO (Figure 5.15).

In LO environment, the oxides formed are characterized by flower shaped-needles. This oxide microstructure can be related to the different environmental conditions to which the gasket was exposed: the gasket was located in a remote area with stagnant water and low oxygen. The XRD analyses revealed that the oxide is mainly Copper (I) oxide, with the formula Cu_2O (Figure 5.15). The solid deposits in the oxidizing environment are larger in size compared to those formed in the reducing environment.

The thickness of Cu oxide sample coating formed in oxidizing environment was determined to be 3 μm in the copper samples and it was measured with a Calotest series Industrial (CAT²i) – Anton Paar GmbH – Graz - Austria (Figure 5.16).

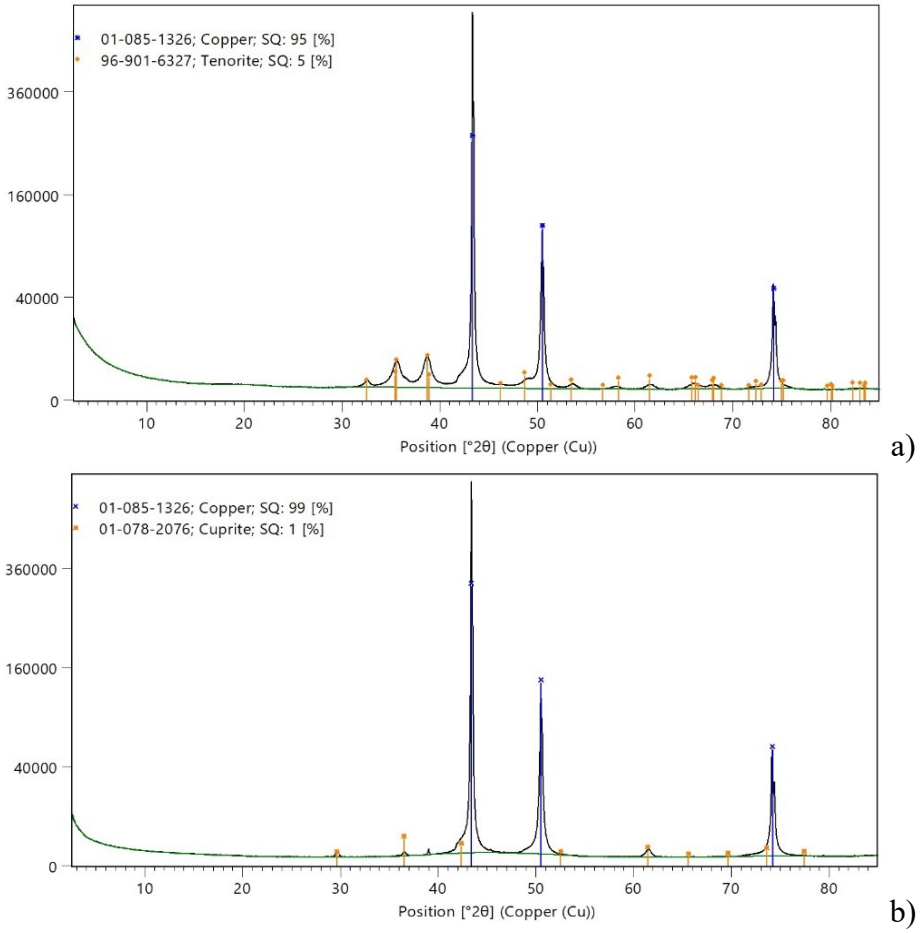

Figure 5.15: XRD analyses on Cu samples in a) HO, b) LO

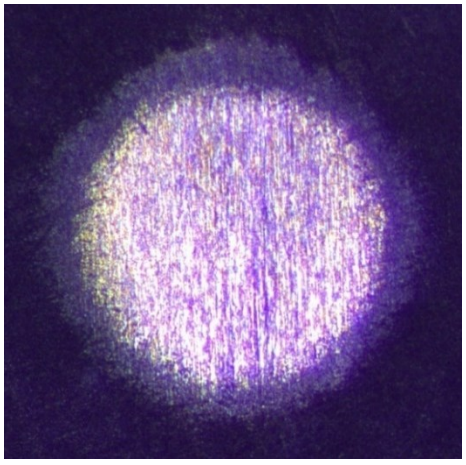

Figure 5.16: Crater on Cu oxide formed with the Calotester

5.3.4 Stress Corrosion Cracking Initiation

Electrochemical experiments were conducted at department of Industrial Engineering in Padua to compare the results of metal release tests with microcapillary tests for both Copper and Stainless Steel samples. The microcapillary facility used is the one described in Section 4.6. New samples, tailored for microcapillary testing, were prepared using the same procedure but with dimensions measuring 13.2 x 20 x 0.8 mm. Two sets of experiments, referred to as 'type n.1' and 'type n.2,' were carried out, mirroring the methodology used in the previous metal release tests, albeit without the collection of water samples. On both Experiment Type n.1 and Experiment Type n.2, a maximum exposure period of 4 weeks was utilized, with the following time step: 3 hours, 24 hours, 1 week and 4 weeks. As a standard practice, the water in the containers was replaced at each sampling interval to mitigate any potential saturation effects stemming from the ions released into the solution.

Copper and stainless steel samples underwent grinding to attain uniform "High Roughness," denoted as HR in the subsequent plots reported in Figure 5.17 and Figure 5.18, with a Ra value of around 0.4 μm.

Potentiodynamic polarization measurements were carried out over a range spanning from - 250 to 1500 mV relative to the open circuit potential, utilizing a scan rate of 1 mV sec^{-1}. Galvanostatic measurements were subsequently conducted, employing a current density set at 10% above the breakdown current density, which had been determined through the potentiodynamic polarization measurements.

Specimens were kept in contact with the test solution for 30 min prior to the start of the measurements and each measurement was performed for 30 min. All electrochemical polarization experiments were performed in a solution composed of 3.5% sodium chloride in distilled and deionized water. 3.5% NaCl is the most common contamination in coastal regions and it was used for comparative study. Additionally, prior to the measurements, the solution was purged with argon gas for 5 minutes. This step was taken to standardize the dissolved oxygen levels across all experiments, thereby enhancing the repeatability of the measurements within the controlled and sealed environment of the capillary test method.

Each electrochemical measurement was repeated three times at the centre of the specimens to maintain the same stress condition. All specimens were subjected to varying tensile stress (TS) levels under fixed displacement conditions, corresponding to a level 10% higher than the yield strength. This last value was derived from 316L stress-strain curves.

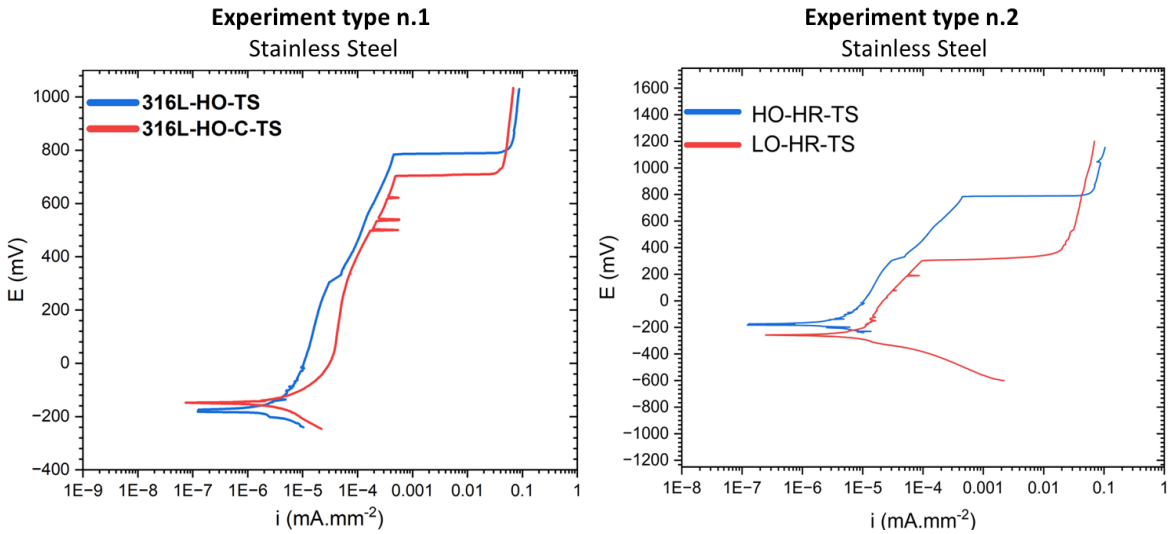

Figure 5.17: Potentiodynamic polarization results. a) SS samples exposed alone and coupled (C) with Cu in HO; b) SS samples exposed in HO and LO environments

Regarding the SS samples, the potentiodynamic polarization results reveal that, in a high-oxygen environment (Figure 5.17a), specimens exposed in isolation exhibited a slightly higher breakdown potential (E_{break}) compared to specimens exposed in conjunction with Cu, with a difference of approximately 80 mV_{SCE}. Therefore, SS samples exhibit a slightly reduced resistance to localized corrosion when coupled with Cu compared to SS exposed alone. However, this difference was not evaluated during the metal release tests. The findings suggest that metal release tests should be replicated using the same stainless steel from the same manufacturer, as done for the SCC tests. The evolution of the passive layer should be concurrently studied through SCC tests to assess potential galvanic coupling. The potentiodynamic polarization results are summarized in Table 5.4.

However, when we shift our focus to the comparison of SS samples exposed to HO and LO conditions (as shown in Figure 5.17b), it becomes evident that E_{break} significantly decreases for samples exposed to the reducing environment, with a reduction of approximately 480 mV_{SCE}. This result implies that SS samples exposed to LO conditions experience a significantly greater degree of localized corrosion attack on the surface due to a lower integrity of the passive layer compared to the HO samples.

It's worth noting that the potentiodynamic polarization method involves an extended testing duration with a gradual alteration of the potential. Nonetheless, this method may not provide sufficient insights into the evolution and kinetics of passive layer deterioration at specific critical potential or current density levels.

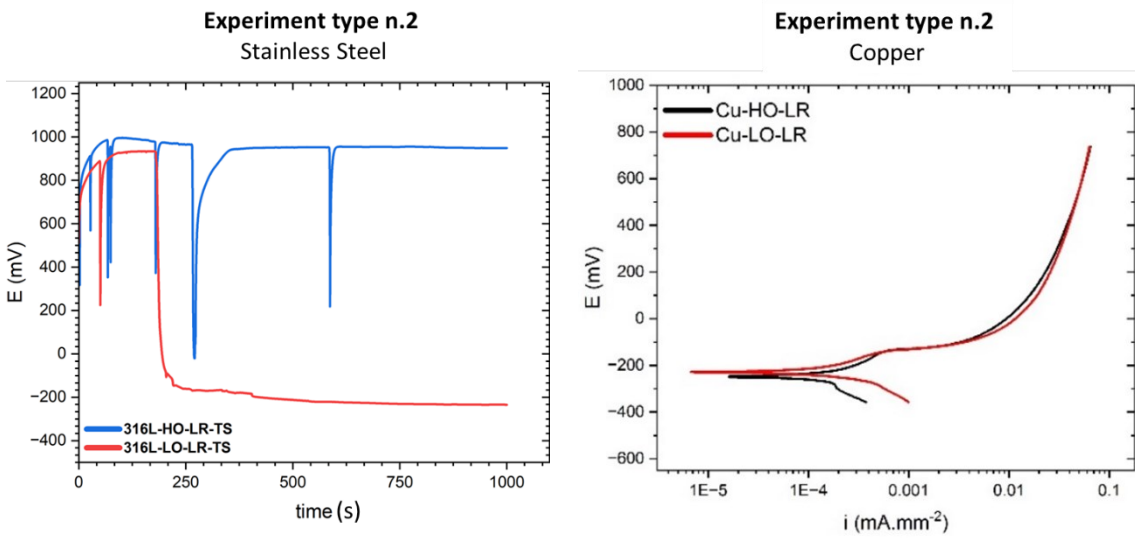

a) b)

Figure 5.18: a) Galvanostatic polarization results for SS samples exposed in HO and LO conditions; b) Potentiodynamic polarization results for Cu samples exposed in HO and LO conditions

Galvanostatic polarization measurements were employed to provide insights into the progression of the passive layer under a constant current density, a reliable method for assessing the integrity of the passive layer over the course of exposure. Figure 5.18a illustrates the galvanostatic results for SS samples exposed to both HO and LO conditions. It is evident from the graph that the protective oxidizing layer undergoes a continuous cycle of formation and rupture during the entire test duration for SS samples exposed to UPW in oxidizing environment. This observation highlights that the passive layer formed is resisting to corrosion. Local breakdown are occurring during the test performed in TS loading but recovering of the passive layer is occurring through the overall test. Conversely, for LO-exposed samples, a noticeable potential drop (E_{drop}) is clearly detectable in the graph and equal to 900 mVSCE. The passive layer has a bad integrity and it breaks irreparably during the test. This phenomenon helps to explain why, in potentiodynamic polarization plots, SS samples exposed to LO conditions appeared to exhibit a higher susceptibility to SCC initiation. It's noteworthy that SS samples were introduced into the glovebox immediately after the surface preparation process, without allowing time for the oxide layer to develop. To gain deeper insights into the genuine impact of low oxygen conditions, it is advisable to repeat this experiment with SS samples that have been pre-passivated and subsequently exposed to a reducing environment.

Regarding copper, the potentiodynamic polarization measurements presented in Figure 5.18b underscore that Cu samples exhibit similar behaviour in both HO and LO conditions. The tenorite layer formed on Cu samples in an oxidizing environment does not

Table 5.4: Potentiodynamic polarization results

Material and Experiment type	Stainless Steel Experiment type n.1		Stainless Steel Experiment type n.2		Copper Experiment type n.2	
Specimens	*HO-Alone*	*HO-C*	*HO*	*LO*	*HO*	*LO*
E_{corr} (mV_{SCE})	-192	-154	-187	-275	-228	-250
i_{corr} ($mA\ mm^{-2}$)	1.28E-7	7.82E-8	1.23E-7	2.51E-7	7.01E-6	1.70E-5
E_{break} (mV_{SCE})	783	702	772	294	-138	-138
i_{break} ($mA\ mm^{-2}$)	4.85E-4	5.17E-4	4.69E-4	9.82E-5	6.78E-4	6.78E-4

provide effective protection. Similarly, in LO conditions, the formation of cuprite oxide is observed, but it also fails to safeguard the samples. These findings align with the results from the metal release tests presented in Section 0 and in Section 5.3.2, underscoring the agreement between the different methods of assessment. Copper samples were also subjected to testing under HO conditions, both individually and in combination with stainless steel. However, the results did not reveal any significant disparities between the two conditions. Therefore, in this context, only the potentiodynamic results for copper samples exposed in Experiment type n.2 are presented here.

5.4 Discussion

The main objective of this work was to collect reference metal release data to be compared with the ones estimated for SPIDER and MITICA PCs and collect useful information regarding the behaviour of the main materials used in NBTF cooling plant.

Despite the cooling plant nominally working in the turbulent regime, some areas were identified where stagnant water is present, these being Cu/SS junctions. For this reason samples of Cu, stainless steel 316L and VTTJ were exposed to stagnant ultrapure water at ambient temperature. Two type of experiments were conducted: one in oxidizing environment to study the coupling of Cu and SS, and the second one was carried out in both HO and LO environments to study oxygen influence on metal releases rate.

The coupling of Cu and SS in VTTJ samples did not show a significant difference: a small increase was observed for Fe, Cr and Mo in SS samples exposed alone, and for Co and Mn in VTTJ samples. These variations were related to a bulk composition difference as the stainless steel used for the VTTJ samples was supplied by a different manufacturer compared to the SS used in all other tests. No difference was detected for Cu exposed alone or coupled with SS. Furthermore, repeated exposure of SS and Cu samples in UPW resulted in decreased amounts of SS released metals with time. This behaviour was not observed for copper that

seems not to passivate in UPW in the experimental conditions, despite the almost uniform CuO layer formed on top of the samples.

The tests conducted in both HO and LO environments highlighted that in the oxidizing atmosphere, there was an increase in the release of copper ions over the sampling time due to the presence of oxygen. Different results were obtained for the experiments conducted in the Glove Box, in reducing environment, where the low quantity of DO inhibited the release of copper ions. SS elements demonstrated the same release rate in both conditions.

The oxide morphology formed on copper samples exposed to low and high levels of oxygen was characterized. The oxygen present in the water heavily influences the type and morphology of copper oxides and their protectiveness.

Metal release tests were compared with preliminary Stress Corrosion Cracking (SCC) tests conducted using the microcapillary method. These tests showed that SS samples exposed individually to HO conditions have a slight higher resistance to localized corrosion with respect to SS coupled with copper. For SS samples exposed to both HO and LO conditions, the combination of potentiodynamic and galvanostatic results indicated that a passive layer does not form on the SS surface when DO levels are low. Consequently, the SCC behaviour worsens for SS samples exposed to LO conditions compared to HO conditions. The absence of an oxide layer also explains the similar metal release trends observed in SS alloy elements under both conditions.

Regarding copper, the potentiodynamic polarization results have substantiated that the tenorite formed on top of copper in oxidizing environment does not offer effective protection against further corrosion. These same results regrading oxide protectiveness were obtained in a reducing environment, characterized by low levels of DO, where the formation of cuprite occurred. This underscores the fact that neither tenorite nor cuprite serves as a reliable barrier to prevent ongoing corrosion of the metal.

Future work will be the study of pre-passivated SS samples in reducing environments to assess the behaviour of the protective oxide when exposed to UPW with a low oxygen content. Additionally, metal release tests should be replicated for SS samples coupled with copper using the same stainless steel provided by the same company. The study will also include investigating surface passivation during the immersion time using electrochemical techniques to assess oxide evolution over water exposure time. Moreover, analyses of the passive layer using surface techniques such as XPS will be conducted.

Chapter 6
SPIDER Cooling Plant Water Degradation

This chapter and the next Chapter 7 deals with the water degradation issue related to some of NBTF Primary Circuits (PCs), specifically the ones responsible for cooling down the power supplies, designated as PC01 for SPIDER and PC08 for MITICA. Addressing water degradation is of utmost importance to ensure it does not adversely affect the ongoing SPIDER operations and future MITICA operations. Failing to effectively manage and mitigate water degradation could lead to significant consequences, potentially endangering the performance and longevity of these critical systems. This chapter only deals with SPIDER water degradation. MITICA will be treated in the next Chapter 7.

SPIDER commenced operations in the middle of 2018 and fast water quality degradation was observed during the 2019 and 2020 experimental campaigns. This degradation of water quality has a notable impact on the operation of the SPIDER experimental campaigns, as the conductivity of the water had to be carefully controlled within narrow parameters to ensure the electrical insulation of components exposed to varying voltage levels. Specifically, in the PC01 circuit, which is a part of the SPIDER cooling plant, it is imperative to maintain water conductivity below 0.3 μS/cm at 25°C. However, it was observed that the water conductivity in PC01 rapidly exceeded this upper limit within just a few hours of operation. Notably, PC01 exhibited the most severe water degradation compared to the other primary circuits in SPIDER, namely PC02 and PC03, which are responsible for cooling the beam source (BS). When the upper limit of water conductivity is reached, it necessitates the suspension of SPIDER experiments to introduce fresh UltraPure Water (UPW) and restore the desired water conductivity. To address this issue, an initial analytical assessment of the water quality degradation across all SPIDER primary circuits was conducted. Following this, a dedicated experimental campaign was put forward to identify the causes of water degradation within the SPIDER cooling circuits.

The first part of the chapter is dedicated to the analytical estimation of water degradation occurring in the PCs that have been used from 2018, specifically PC01, PC02 and PC03. In the second and third part are reported the circulation experiments performed at constant temperature and flow rate using high-purity water in PC01 and PC03 to tackle the cause of SPIDER cooling circuit water degradation. PC03 was considered the “baseline” circuit for these analyses.

6.1 Analytical Estimation of Water Grade Degradation

SPIDER utilizes four Primary Circuits (PCs) for active cooling of its components, as described in Section 1.4.5, in Table 1.3: Thermo-hydraulic requirements for SPIDER components. Presently, only the first three circuits, namely PC01, PC02, and PC03, had been in operation. The fourth circuit, PC04, which is intended for cooling the Beam Dump, was connected towards the end of 2021 but has not yet been fully utilized.

To analyse these circuits, the primary hydraulic characteristics were computed for PC01, PC02 and PC03. Utilizing the available 3D CAD models and drawings, key geometric parameters such as length and diameter were determined. In cases where the cooling channels had non-circular cross-sections, the equivalent hydraulic diameter was calculated as follows:

$$d_h = \frac{4S}{P_w} \qquad \text{Eq. 6.1}$$

Where d_h is the equivalent hydraulic diameter [m], S the cross section [m^2], and P_w the wetted perimeter [m].

In addition, for each of the circuits, various parameters were estimated, including the volumetric flow rate in cubic meters per hour (m^3/h), volume in cubic meters (m^3), wetted area in square meters (m^2), mean velocity in meters per second (m/s), and the Reynolds number. These estimates were derived using water properties calculated at a temperature of 25°C and a pressure of 1 atmosphere, as detailed in Perry's Chemical Engineers' Handbook [78]. The values for these parameters are provided in Table 6.1.

Table 6.1: Water properties formula estimation

Name	Symbol	Unit of measure	Equation	
Density	ρ	$\frac{kg}{m^3}$	$\rho = -13.851 + 0.64038T - 0.00191T^2 + 1.8211 \cdot 10^{-6} \cdot T^3$	Eq. 6.2
Viscosity	μ	$Pa \cdot s$	$\mu = e^{(-52.843+\frac{3703.6}{T}+5.866\cdot\ln(T)-5.879\cdot 10^{-29}\cdot T^{10})}$	Eq. 6.3
Molar Weight	Mw	$\frac{kg}{mol}$	18.015	Eq. 6.4

where T is the temperature of water in Kelvin.

Table 6.2: Hydraulic parameters formula

Name	Symbol	Unit of measure	Equation	
Volumetric Flowrate	$\dot{V}$	$\frac{m^3}{h}$	$\dot{V} = \frac{\dot{m} \cdot 3600}{\rho}$	Eq. 6.5
Volume	V	m^3	$V = L \cdot S$	Eq. 6.6
Wetted Area	A_w	m^2	$A_w = P_w \cdot L$	Eq. 6.7
Mean velocity	v	$\frac{m}{s}$	$v = \frac{\dot{V}}{S \cdot 3600}$	Eq. 6.8
Reynolds number	Re		$Re = \frac{\rho \cdot v \cdot d_h}{\mu}$	Eq. 6.9

Where $\dot{m}$ is the mass flowrate in [kg/s] and L is the pipeline length [m].

The materials involved in the calculations are stainless steel (AISI-304 and AISI-316L) and copper. Additionally, alumina and polypropylene (PP) were considered, but only for overall volume and hydraulic characteristics calculations.

The primary hydraulic characteristics of the three main PCs are summarized in Table 6.3, and the following observations can be made:

- PC02 has the largest total volume, primarily due to the contribution of stainless steel piping. On the other hand, PC01 has the highest volume of copper.
- PC02 also boasts the highest nominal volumetric flow rate among the circuits.
- In terms of total wetted area, PC02 leads the way, while PC01 has the smallest total wetted area.
- When it comes to copper wetted area, PC01 and PC02 are comparable, with values of 6.2 and 6.94, respectively. Consequently, PC01 has the highest ratio of copper to stainless steel wetted area, with a ratio of 0.34, while PC02 and PC03 have ratios of 0.07 and 0.06, respectively.
- PC03 is the longest circuit in terms of length.

Table 6.3**:** PCs hydraulic calculations

	PC01			**PC02**			**PC03**		
Tot Volumetric Flowrate [$m^3\ h^{-1}$]	64.798			181.642			44.062		
	Cu	*SS*	*Tot*	*Cu*	*SS*	*Tot*	*Cu*	*SS*	*Tot*
Length of the pipeline [m]	78.23	128.80	235.98	378.21	449.75	827.95	335.01	505.97	840.99
Wetted Area [m^2]	6.20	18.24	24.44	6.94	97.03	103.98	3.70	61.91	65.60
Inner volume [m^3]	0.041	0.58	0.81	0.011	2.74	2.75	0.004	1.13	1.13

After determining the hydraulic characteristics of PC01, PC02, and PC03, an estimation of the variation in water conductivity was made based on the general corrosion of copper and stainless steel components. This estimation was carried out using an analytical approach that assumes water degradation is a result of general corrosion occurring in metallic components within the circuit, such as copper and AISI304L.

The increase in water conductivity can be associated with an elevation in ion concentration within the solution. This relationship is rooted in the fact that the conductivity (k) of an ionic solution is determined by

$$k\left(\frac{\mu S}{cm}\right) = 1000 \cdot \sum \Lambda_i \cdot Ci \qquad \text{Eq. 6.10}$$

where:

Λ_i= The molar conductance of species i [mho $cm^2\ mol^{-1}$] or [S $cm^2\ mol^{-1}$]

C_i = The molar concentration of species i [mol L^{-1}][20].

To calculate the resulting water conductivity, it is possible to determine the type of ions dissolved in the water and their concentration using experimental techniques such as Inductively Coupled Plasma-Mass Spectrometry (ICP-MS), and then apply Eq. 6.10.

For copper, a corrosion rate of 3600 µg $m^{-2}\ day^{-1}$ was assumed. This value was derived from a study by T.E. Eriksen [79], where 99.7 wt% copper was exposed to deionized and double-distilled water for 61 days.

Table 6.4: Total concentration of metallic ions in solution for PC01, PC02 and PC03.

	PC01			PC02			PC03		
	Cu	SS	Tot	Cu	SS	Tot	Cu	SS	Tot
ppm in a day	0.026	0.011	0.037	0.009	0.017	0.026	0.011	0.026	0.037
ppm in 1 hour	0.104	0.073	0.176	0.034	0.114	0.148	0.044	0.177	0.222

With regards of stainless steel, Molander [50] provided corrosion rate trends in the temperature range of 134 – 200 °C as a function of specimen exposure time to ultrapure water. Although no literature was found regarding corrosion of stainless steel in ultrapure water at ambient temperature, a corrosion rate of 480 μg m^{-2} day^{-1} (obtained from the Molander graph [50] for stainless steel at 134°C after 10,000 hours of exposure) was selected. This choice accounts for the fact that SPIDER has been operating for over 2 years at temperatures of 20-25 °C. While the chosen corrosion rate value was obtained at a higher temperature than SPIDER's circuits, it provides a conservative estimate of water degradation. Lower temperatures, in the absence of oxygen, are generally considered advantageous from a stainless steel corrosion perspective [80].

The concentration of metallic ions in the solution, resulting from the general corrosion of components, is presented in Table 6.4 This concentration was estimated by multiplying the corrosion rates (in μg m^{-2} day^{-1}) by the wetted surface area of the components (in m^2) and then dividing this value by the overall circuit volume (in m^3):

$$ppm = \frac{Cor.rate\ [\mu g\ m^{-2}\ day^{-1}] \cdot Wet.Area\ [m^2] \cdot 1[day]}{PC\ Volume\ [m^3] \cdot 1000} \quad \text{Eq. 6.11}$$

Table 6.4 highlights an interesting observation: even though the copper wetted area is similar for both PC01 and PC02 circuits (as indicated in Table 6.1). PC02 exhibits a lower concentration [ppm] of Cu ions in the water after 24 hours. This can be attributed to the larger volume of the PC02 circuit. In contrast, the Cu ppm released within a day for PC01 and PC03 are comparable, mainly because they share a similar ratio of Cu wetted area to total volume.

From these simplified calculations, the ppm in the circuits could be related to an increase of water conductivity in the system by using conductivity - ppm conversion factors found in Table 6.5 Frankel [81] and shown in for copper and stainless steel.

Table 6.5: Resistivity and conductivity conversion taken from Frankel [81] book

Water type	ppm	Conductivity	Resistivity	ppm or mg/L				
	as CaCO3	[µS/cm]	[MΩ·cm]	only Cu	only Fe	only Cr	only Ni	only AISI 304L
II	0.850	2.210	0.450	0.541	0.316	0.294	0.495	0.320
	0.420	1.130	0.880	0.268	0.156	0.145	0.245	0.158
	0.170	0.490	2.050	0.108	0.063	0.059	0.099	0.064
	0.130	0.380	2.650	0.083	0.048	0.045	0.076	0.049
III	0.085	0.270	3.700	0.054	0.032	0.029	0.049	0.032
I	0.057	0.200	5.000	0.036	0.021	0.020	0.033	0.022
	0.042	0.160	6.150	0.027	0.016	0.015	0.024	0.016
	0.017	0.098	10.200	0.011	0.006	0.006	0.010	0.006

Therefore, the increase in conductivity observed during SPIDER operation could be directly related to an increase in ionic species dissolved in the ultra-high resistivity water [20].

Water degradation rates in terms of conductivity increase are of the same order of magnitude for all the PCs, with an approximate increase of 10^{-3} [µS cm^{-1} h^{-1}] per hour. This similarity in degradation rates directly correlates with the estimated release of ppm from each circuit, which determines the conductivity variation. Additionally, the frequency of water treatments per week was calculated based on 8 hours of operation for 4 days. This analysis revealed that PC01 requires two water changes per week, indicating the highest frequency of water treatments among the circuits. This higher frequency is driven by the stricter water quality requirements, particularly regarding conductivity, in PC01.

Table 6.6: Conductivity increase calculation results for PC01, PC02 and PC03.

	PC01			PC02			PC03		
Water conductivity requirements [µS/(cm)]	0.2 – 0.3			0.5 – 1			0.5 - 1		
	Cu	SS	Tot	Cu	SS	Tot	Cu	SS	Tot
Δk [µS/(cm day)]	0.1036	0.0726	0.1763	0.0342	0.1141	0.1484	0.0444	0.1774	0.2218
Δk [µS/(cm h)]	0.0043	0.0030	0.0073	0.0014	0.0048	0.0062	0.0018	0.0074	0.0092
Water treatments [1/week]	2.06			0.29			0.42		

These estimated water degradation rate were compared to the experimentally ones observed during 2019-2020 campaign. Figure 6.1 shows the trends for water degradation and the relative conductivity rate increase [µS cm^{-1} h^{-1}] for PC01, PC02 and PC03 during operation on the 28th May 2019, which was taken as a representative experimental day. Similar trends were observed on other experimental days. Figure 6.1 (a) shows the conductivity variation for PC01, Figure 6.1 (b) the conductivity variation for PC02 and Figure 6.1 (c) the conductivity variation for PC03. The conductivity variation was assessed over a 4-hour period, starting from 12:40:00 until 16:40:00. This specific time frame was chosen to ensure a linear and stable conductivity trend for all three primary circuits.

The conductivity increase rate during experiments is approximately 0.047 [µS cm^{-1} h^{-1}] in PC01, 0.003 [µS cm^{-1} h^{-1}] in PC02 and 0.007 [µS cm^{-1} h^{-1}] in PC03. These increase rate are not evaluated at constant temperature. The real conductivity increase trend can be compared with the one analytically before (Δk_{real} / $\Delta k_{estimated}$):

- PC01: $\frac{\Delta k_{real}}{\Delta k_{estimated}} = 6.4$
- PC02: $\frac{\Delta k_{real}}{\Delta k_{estimated}} = 0.5$
- PC03: $\frac{\Delta k_{real}}{\Delta k_{estimated}} = 0.67$

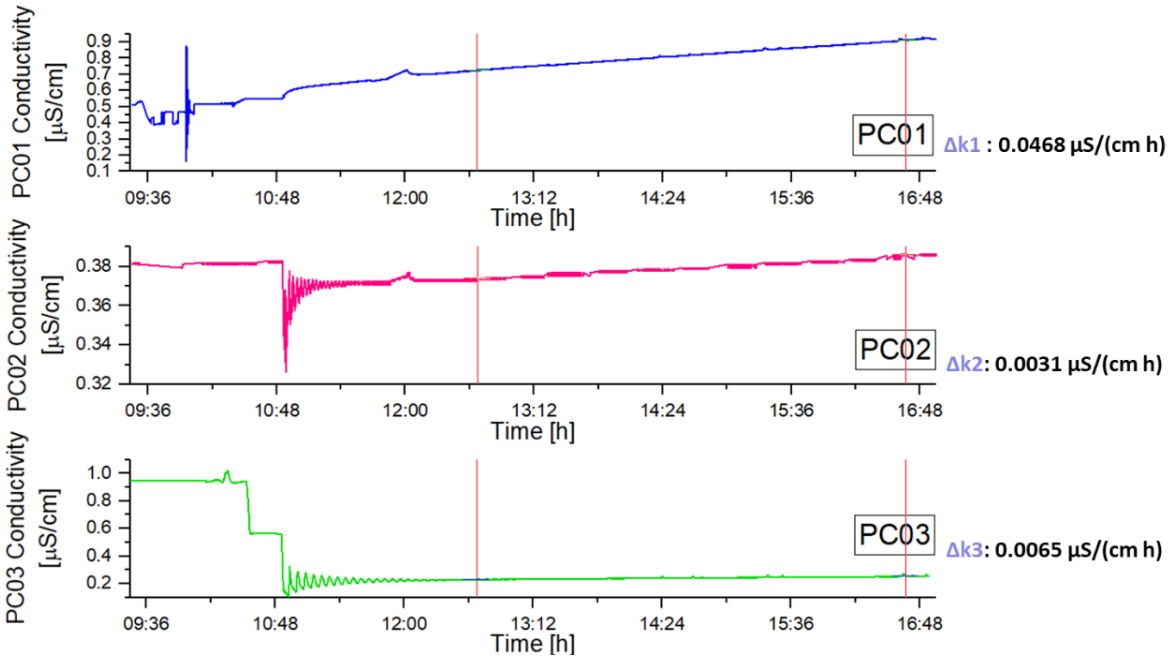

Figure 6.1: 28th May 2019: PCs conductivity variation in the range [12:40, 16:40]

Water conductivity degrades 6.4 times faster for PC01 than the calculations here presented. By contrast, PC02 and PC03 reveal a degradation of 0.5 and 0.67 times slower than the reported estimations.

These plots unmistakably demonstrate that PC01 consistently surpasses the upper conductivity threshold of 1 μS/cm within a mere few hours, demanding the daily replenishment of water prior to each new experimental session. Although the estimated frequency of PC01 water treatments was approximately twice a week, in reality, water is refreshed every morning before the start of each day's experiments. This recurring need for water replacement poses a pressing challenge for SPIDER operations, as it consumes about 40 minutes of time and must be completed before the commencement of daily experimental sessions.

6.2 Water Circulation Tests

Circulation experiments were performed at constant temperature and flow rate using high-purity water in PC01 and PC03 to tackle the cause of SPIDER cooling circuit water degradation. PC03 was considered the “baseline” circuit for these analyses.

To avoid any contamination during the analysis of UPW, an ASTM procedure [82], which is the one described in Section 5.1.2.1, was followed. Sampling UPW from SPIDER was conducted by only using components made in stainless steel, and by flushing water for at least 5 min prior to sampling. UPW samples from PC01 were prepared following the standard reported in Section 5.1.2.2. Trace metal analysis was performed using an ICP-MS Agilent Technologies 7700x system (Agilent Technologies International, Santa Clara, CA, USA) on three water samples prepared from the same circulation experiment. The concentration of ions in each circulation experiment was determined by averaging the values from three water samples while taking into account the standard error. Three circulation experiments were done for each configuration in different days or months using the same initial conditions to assess repeatability and robustness of the implemented experimental procedure. Corrosion products found in solid form were observed in secondary electron and backscattered mode using an SEM and analysed with energy-dispersive X-ray spectroscopy (EDS). XRD analyses were conducted on wetted corrosion products in their original form and on dried powders after a heat treatment at 600 ◦C for a few hours inside a muffle furnace.

Before conducting any water circulation test, conductivity sensors, indicated in the following PCs sketch with the letter “k”, were recalibrated. It was found that the conductivity sensors installed in PC01, PC02 and PC03 were transmitting wrong values of water conductivity as they had been calibrated in the past with a wrong procedure that changed sensors cell constant. It was discovered that the cell constant of sensors in PC01, PC02 and PC03 was different between each other’s and, additionally, it was different from the cell

constant established by the manufacturer. The cell constant in a conductivity sensor is defined by:

$$\Theta = \frac{\text{measured resistance } (\Omega)}{\text{reference solution resistivity } (\Omega \cdot \text{cm})} = \text{cell constant } (\text{cm}^{-1}) \qquad \text{Eq. 6.12}$$

Before November 2020, calibrations of conductivity sensors were done using a buffer solution with a conductivity of 84 μS/cm at 25 °C or by comparison using a conductivity sensor. The buffer solution conductivity was well above the operational range in which SPIDER sensors operate (conductivity between 0.055 – 2 μS/cm at 25 °C). A new method was applied from November 2020 to calibrate conductivity sensors. This method involves the use of UPW as a standard to calibrate conductivity sensors. Calibration is achieved by comparing the readings of the sensors in question with those of a certified sensor designed for UPW applications, which is installed in series within the circuit during the calibration procedure. By applying this method, , it was possible to verify that sensors installed in SPIDER were not working properly simply because of the wrong cell constant imposed. By re-inserting the manufacturer cell constant, 0.01 cm^{-1}, the conductivity sensors starts to read correctly again. This calibrating method was also applied to MITICA.Primary Circuit PC01.

6.3 Primary Circuit PC01

SPIDER PC01 cools down the Acceleration Grid Power Supply (AGPS), the Ion Source and Extraction Power Supplies (ISEPS) and Transmission Line (TL). ISEPS includes all the power supplies required for running the negative ion source of ITER NBI and for extracting an ion beam from the source [83]. The SPIDER ISEPS system is installed within the High Voltage Deck (HVD), a Faraday cage of 150 m^2 approximate floor area, supported by insulators [83]. The ISEPS local control system is divided in four subunits, corresponding to the extraction grid power supply (ISEG), the radiofrequency power supply (ISRF), Power distribution system and the Source Support power supplies (ISSS). ISRF is composed of a common high voltage dc power supply (ISRF-TE) feeding four independent RF generators (ISRF1/2/3/4).

6.3.1 Circulation Experiments

Circulation experiments were performed at constant temperature (T = 25 ◦C) and flow rate (∼75 m3/h). High-purity water was utilized to ensure that, at the onset of each circulation experiment, a water conductivity of approximately 0.06 μS/cm at 20°C was attained.

Throughout these water circulation tests, the water loop exclusively incorporated the four independent RF generators (ISRF1/2/3/4), characterized mainly by copper coils.

Consequently, the water came into contact with components primarily composed of copper, stainless steel, and plastic. Plastic tubing was employed for insulation purposes on the power supplies (PS).

To systematically investigate the origins of water degradation, the PC01 circuit was segmented into different subsystems, effectively isolating each individual component. This initial phase of testing focused on assessing water degradation in the absence of voltage application to components and considering only the circuit from the hydraulic point of view. In this way, it was possible to isolate and identify the possible source for the observed water degradation.

Water samples were taken from each circulation experiment at the beginning of the test (time = 0) when water conductivity reached ∼0.06 μS/cm. A second sampling was performed at the end of a 3.5 h circulation experiment performed at constant temperature, pressure, and flowrate. UPW was sampled at production site and used as a blank (background control). PC01 circulation experiments were conducted following three configurations.

1) "*All in*" configuration: the entire circuit was wetted by UPW. All the components were inserted in the circuit.
2) "*Bypass only*" configuration: only stainless steel surfaces were exposed to UPW by isolating all the copper components from the main stainless steel piping circuit.
3) "*ISEPS in*" configuration: the main copper components of the ion source and extraction power supply (ISEPS) were inserted in the water loop. The transmission line (TL) was excluded. ISEPS loop was only characterized by ISRF generators.

The AGPS was not included in the above-mentioned tests. The increase in conductivity for each experiment was measured in a time interval where the temperature was stable at 25 ◦C to avoid temperature-related fluctuations in the conductivity.

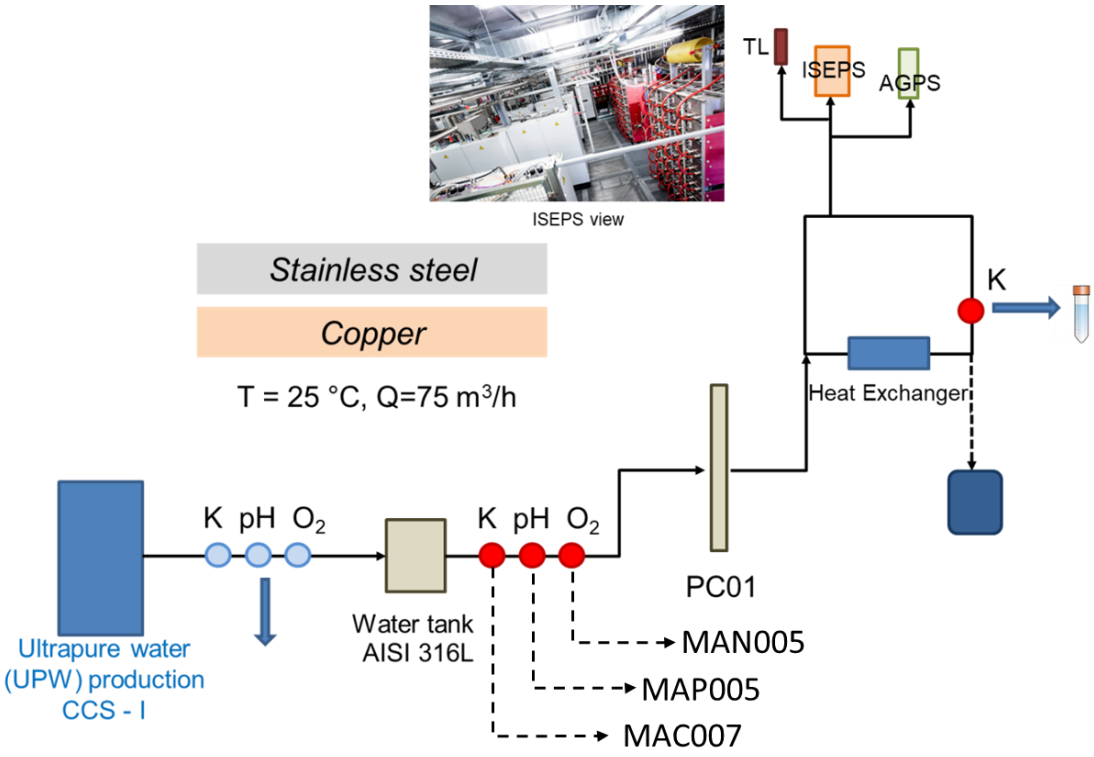

Figure 6.2: SPIDER PC01 cooling circuit schematic showing the position of water sensors and sampling points.

Figure 6.2 shows a schematic of PC01 circuit with details of the location of sampling points and conductivity sensors. Unfortunately, no O_2 sensors and pH sensors were installed in line in SPIDER circuits so it was not possible to monitor water properties, and only water conductivity could be reported. The conductivity increase during circulation experiments was reported for each configuration tested, namely, "*Bypass only*," "*ISEPS in*," and "*All in*", for each day.

Figure 6.3 shows the conductivity trend and temperature profile for each experiment. Figure 6.4 presents the concentrations of trace metals, specifically quantified cations, determined through ICP-MS analysis of water samples. Only certain cations were quantified in this study. The results revealed that copper and zinc played an active role in the water degradation phenomenon, as both were detected in PC01 water samples in significant quantities, surpassing the limit of detection (LOD) of the ICP-MS instrument. Repeatability of the corrosion process investigated is demonstrated by the overlap and minimal discrepancy from water conductivity trends in experiments shown in Figure 6.3 and Figure 6.4.

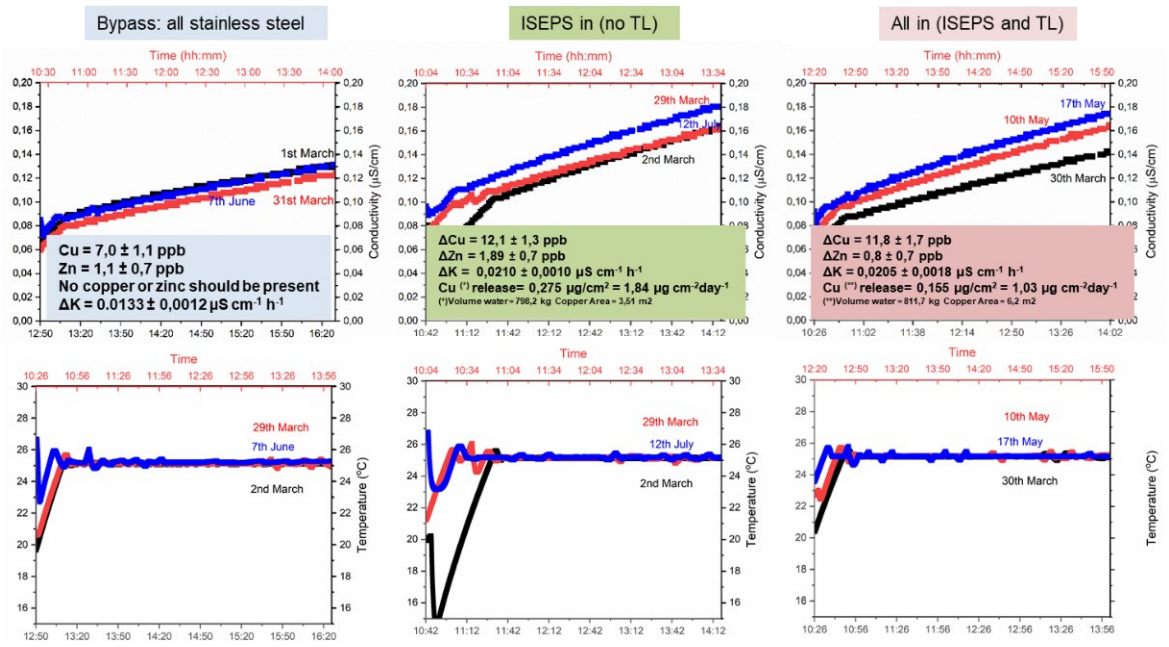

Figure 6.3: Water conductivity trends in SPIDER circulation experiments (top) and temperature profiles during each test (bottom). Concentrations of ions (C_{Cu} and C_{Zn}) measured in water sampled with ICP-MS

Figure 6.4 clearly indicates a significant release of Cu and Zn originating from ISEPS. In the "ISEPS in" experiments, a notable copper release rate of 1.84 $\mu g \cdot cm^{-2} \cdot day^{-1}$ was measured, accompanied by a noticeable increase in conductivity of $\Delta k = 0.0210 \pm 0.0010$ $\mu S \cdot cm^{-1} \cdot h^{-1}$, as reported in Figure 6.3.

The ppb plot in Figure 6.4 further illustrates a substantial elevation in the concentrations of Cu and Zn detected in the "*ISEPS in*" experiment, coinciding with an increase in water conductivity when compared to the "Bypass only" configuration.

Interestingly, both the "*ISEPS in*" and "*All in*" experiments exhibited identical increases in water conductivity and Cu release into the water. This observation is derived by the overlap in average values and error bars for Cu and Δk (variation in conductivity), as depicted in Figure 4.4. While it was well known to have copper components in PC01 in contact with the water, the presence of zinc in the circuit was unexpected. The coexistence of Cu and Zn was linked to a potential corrosion source within ISEPS.

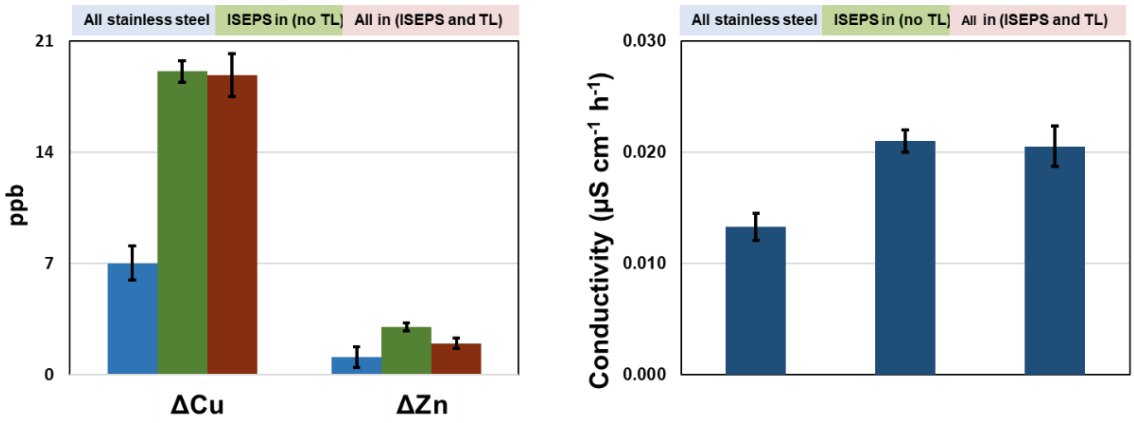

Figure 6.4: ΔC_{Cu} and ΔC_{Zn} average and SD values measured by ICP-MS on water sampled from circulation experiments, average Δk,and SD values

6.3.2 Zinc Contaminants: Pressure Reducers Analyses

The source of the Cu and zinc Zn release was traced back to four pressure reducer components within the ISEPS system that were supposed to be constructed from stainless steel. Upon inspection during maintenance, it was discovered that incompatible materials, not meeting the SPIDER requirements, were used in these components. Specifically, a galvanized plate, a spring made from EN 10270-1 SH (C) steel, and a brass cap were found in a section where UPW flowed. The increased water conductivity was attributed to the presence of significant concentrations of Cu and Zn ions in the UPW circuit.

Corrosion products resulting from the pressure reducer components are visible in Figure 6.5a, which includes two photographs of the pressure reducer and a SEM-EDX analysis of the corrosion products sampled. The identified corrosion products in the pressure reducer included zinc oxide, iron oxides, and copper oxides. Further analysis via XRD after heat treatment at 600°C confirmed the presence of hematite (Fe_2O_3), magnetite (Fe_3O_4), and zinc oxide (ZnO), as shown in Figure 6.5b. The detection of Cu and Zn in the water sampled from "*Bypass only*" experiments highlights the stainless steel piping circuit contamination: Cu and Zn should not be present in stainless steel piping. These contamination was linked to these pressure reducers present in ISEPS.

Pressure reducers with galvanized components were substituted by new ones only made by stainless steel.

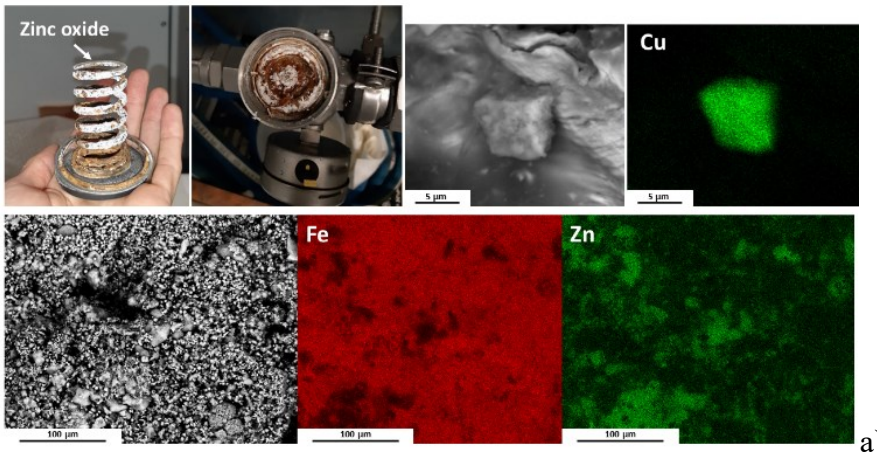

a)

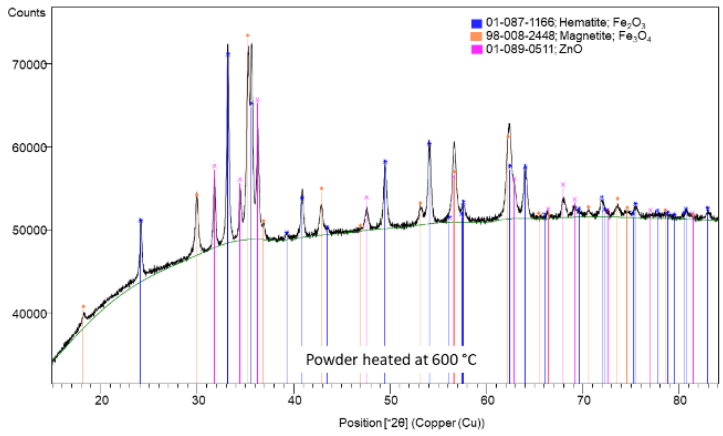

b)

Figure 6.5: a) Photograph of ISEPS pressure reducer. White powder was identified as zinc oxide and red powder was mostly rust. b) XRD analysis of corrosion products sampled from ISEPS pressure reducer.

After replacing the pressure reducers, new circulation tests in "*All in*" configuration were carried out. Before repeating the experiments, water in PC01 was changed for several weeks to clean as much as possible the circuit from zinc traces.

The results, as shown in Figure 6.6, revealed that both the conductivity degradation and the amount of zinc released into the water remained unchanged. This indicates that the source of zinc contamination was not solely the spring mounted on top of the pressure reducers.

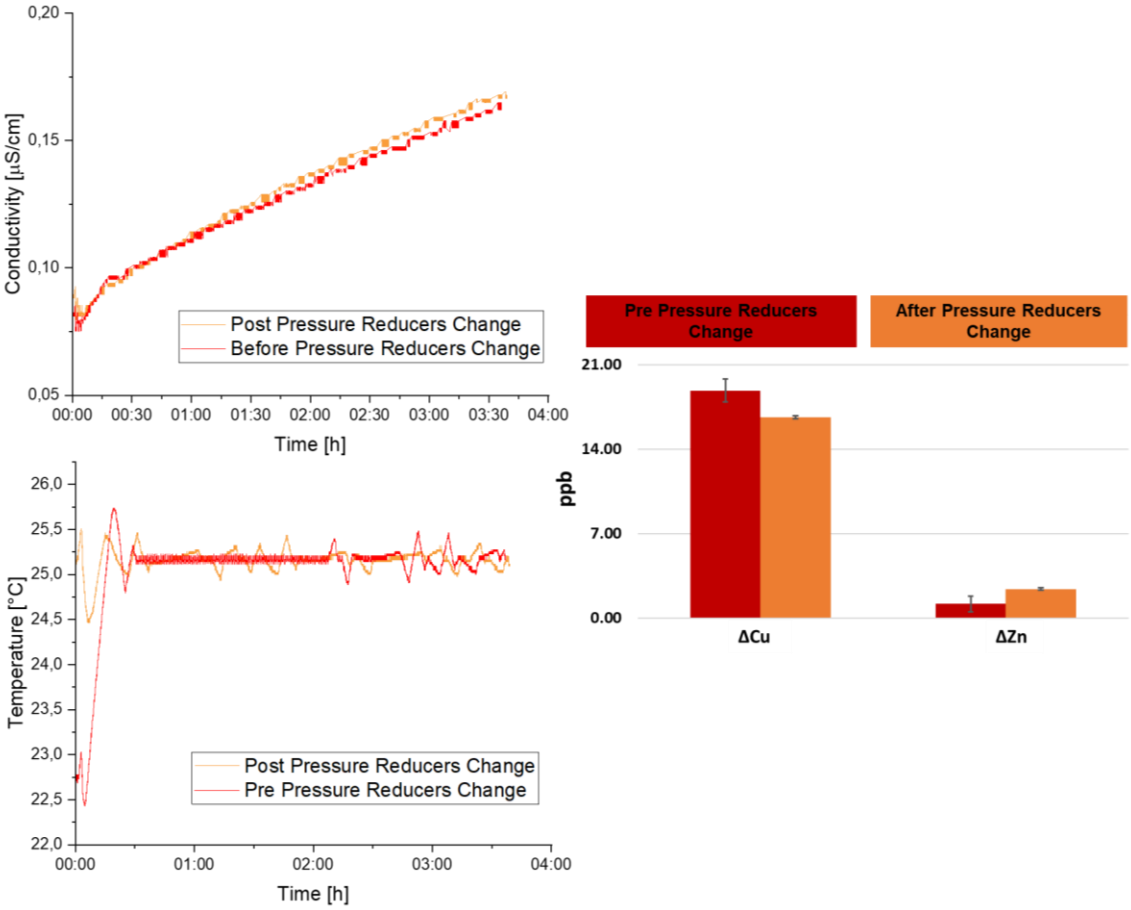

Figure 6.6: Water conductivity trends (left) and metal released in water (right) in SPIDER "*All in*" circulation experiments before and after pressure reducers change

6.3.3 Zinc Contaminants: Plastic Tubes Analyses

Another source of zinc was found in plastic tubes used to insulate PS. SPIDER PC01 incorporates not only copper and stainless steel components but also various types of plastic tubes, categorized as follows:

a) A red type of tube made of internal hose in NBR and a cover in nitrile. It is utilized to insulate Extraction Grid Power Supply (ISEG) module (Figure 6.7a).

b) A green type of tube characterized by an inner hose in black Nitrile Butadiene Rubber (NBR), a polyamide intermediate braid and an outer cover in Hydrogenated Nitrile Butadiene Rubber (HNBR). It is used to isolate the Source Support Power Supply (ISSS) module (Figure 6.7b).

a) b)

Figure 6.7: a) ISEG plastic tubes; b) ISSS plastic tubes

Plastic tubes were examined to evaluate their composition and potential impact on water quality degradation. Initially, stagnant water samples were collected from ISEG modules' tube systems, and these water samples were subjected to analysis using ICP-MS. Stagnant water in ISSS modules was not possible to be analysed. The analysis revealed high levels of zinc traces, as depicted in Figure 6.8.

Consequently, these plastic tubes were investigate by taking plastic samples from virgin tubes and conducting SEM analyses and metal release tests on them to confirm whether the zinc traces detected in stagnant water samples (Figure 6.8) could be attributed to the plastic.

SEM-EDX analyses indicated that both the ISSS green tube (right Figure 6.7) and the red tube (left Figure 6.7). were composed of NBR tubes with incorporated Zinc Oxide particles aimed at enhancing mechanical performance, as illustrated in Figure 6.9a and Figure 6.9b.

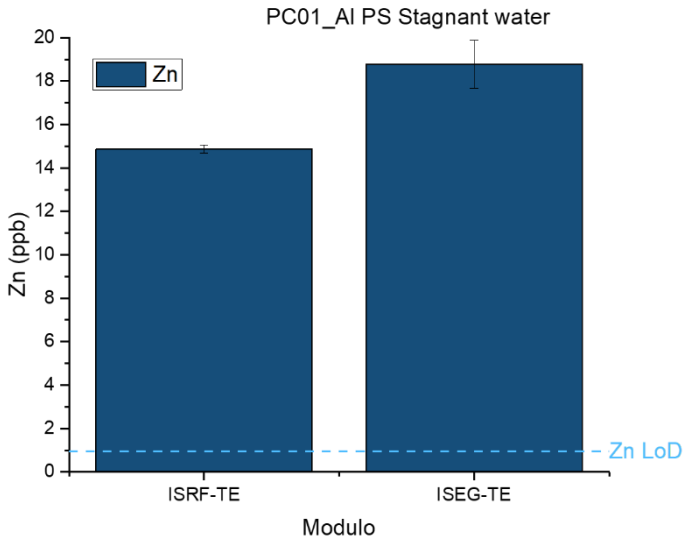

Figure 6.8: Water samples analyses of stagnant water collected from tubes type in ISEG

The metal release were conducted on plastic samples measuring 9.1 cm^2. The objective was to asses if the zinc oxide particle dissolve and contaminate the UPW. Plastic samples were subjected to a cleaning process involving a 5-minute ultrasonic bath with acetone, followed by 5 minutes in ethanol, and subsequent drying. These cleaned steel samples were then placed into UPW that had spilled from the CCS. These experiments were performed in perfluoroalkoxy (PFA) vessels that had been pre-cleaned with HCl, HNO_3 and UPW, following the ASTM D4453-17 procedure [82] described in Section 5.1.2.1. Each sample was immersed in 50 mL of stagnant UPW water, maintaining a constant surface area-to-volume ratio of 0.19 cm^{-1}. The entire procedure was carried out under ambient temperature conditions (approximately 25°C), using stagnant water in a high oxygen environment. Water samples were collected at various time intervals (3 hours, 24 hours, 1 day, 1 week) for subsequent ICP-MS analyses. The water in the vessels was changed at each sampling step to prevent any saturation effects caused by released ions in the solution. For assessment, triplicate samples were considered for each type of plastic, and a blank sample containing only the test solution was evaluated to confirm the absence of metals in the background solution. This was achieved by running these samples in parallel.

The metal release tests confirmed that these particles dissolved in water, releasing zinc ions that were detected in the stagnant water samples and during water circulation tests (Figure 6.9c).After 4 weeks, red tube employed in ISRF modules reached a release rate of about 10 [$\mu g/cm^2$]. To address this concern, the replacement of the current plastic tubes is under consideration with those designed for food-grade purposes.

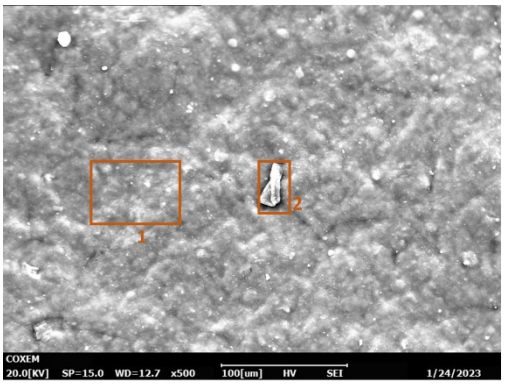

NBR addictivated with Caolinite (Al, Si), Zinc Oxide and Titanium Oxide

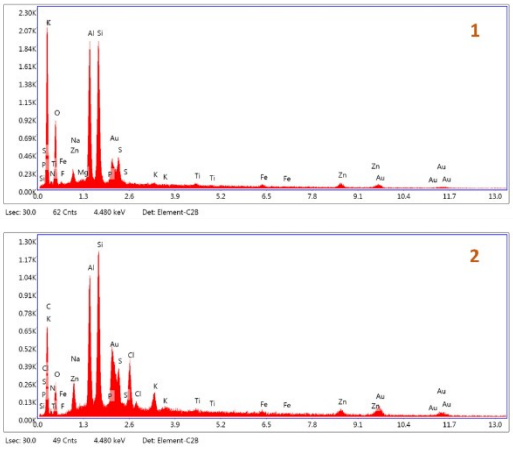

a)

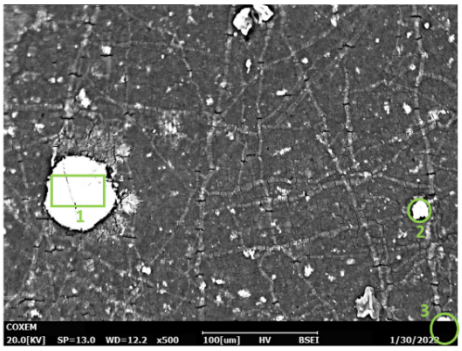

NBR with Aluminum, Zinc and Iron particles

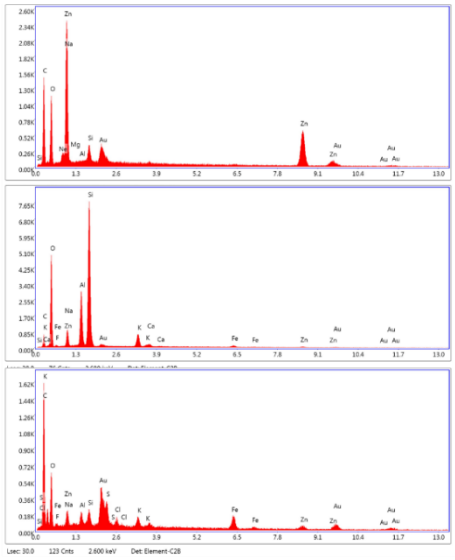

b)

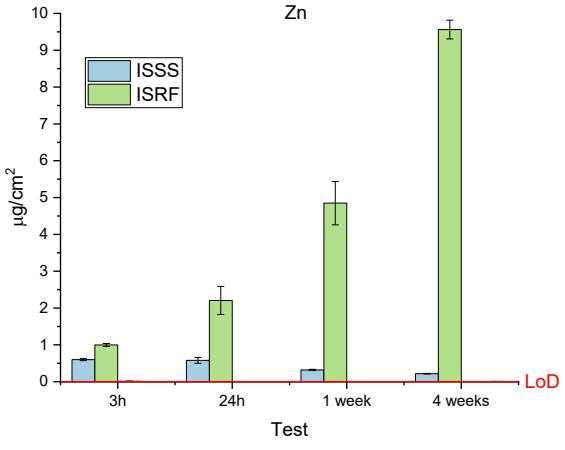

c)

Figure 6.9: Plastic tubes analyses. a) SEM-EDX analyses of ISEG tube; b) SEM-EDX analyses of ISSS tube; c) Zn releases in [µg/cm^2] from plastic samples exposed to UPW

6.3.4 Voltage Application

PC01 was kept at a constant temperature of T = 25°C during three typical SPIDER experimental days to investigate whether the application of voltage (approximately 40kV) had any impact on water degradation. The circuit was operated at this constant temperature while maintaining a flow rate of approximately 75 m³/h. This experiment was repeated twice, and the results were then compared to the water circulation experiments conducted under identical conditions in "*All in*" configuration but without the application of voltage (Figure 6.3).

Figure 6.10 presents the results from experimental days on May 11th and May 13th, 2021, when voltage was applied, and compares them with the results from a water circulation experiment conducted on May 10th, 2021, when voltage was not applied. This observation serves as a critical confirmation that the deterioration in water quality is unrelated to the application of voltage within the circuit. Instead, it can be definitively linked to the specific hydraulic configuration of the circuit itself. This means that the factors contributing to water degradation are inherent to how the system is designed and operated. Consequently, this

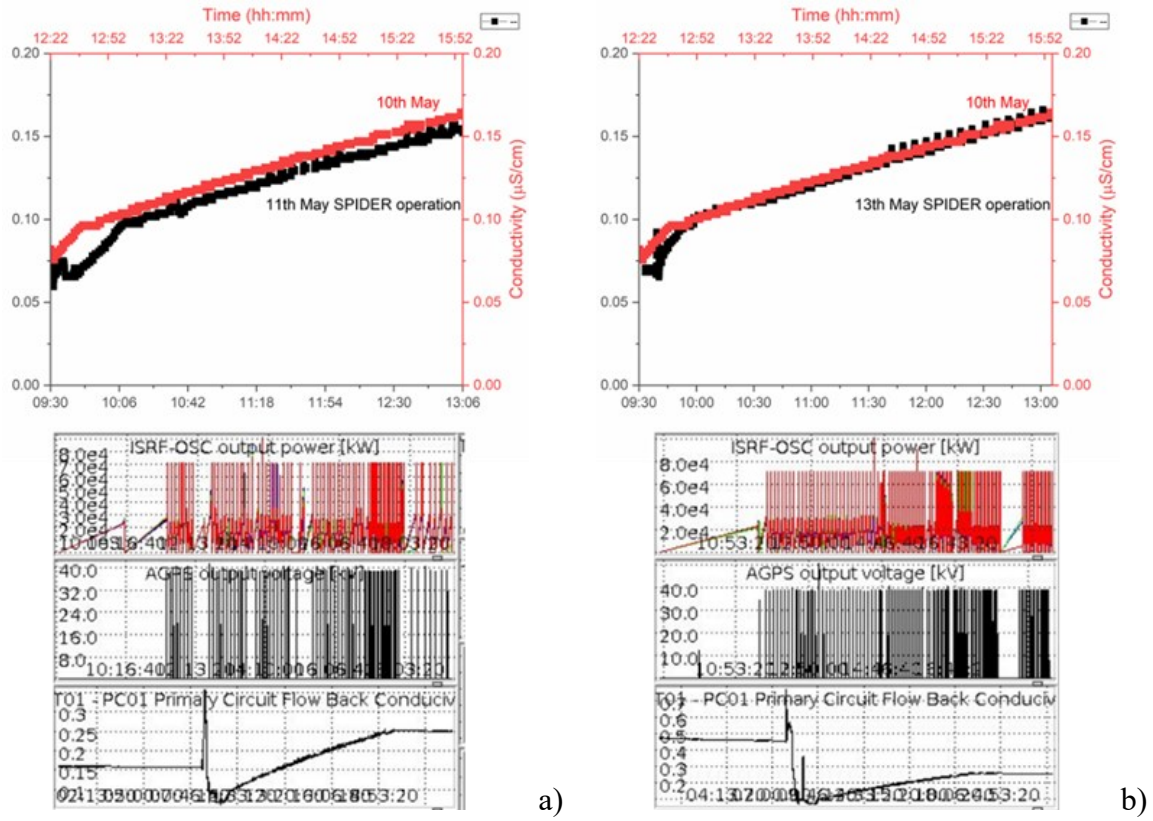

Figure 6.10: Water conductivity trends (left) in SPIDER circulation experiments with (11/05 and 13/05) and without (10/05)voltage application.

clarifies why similar instances of degradation were observed in earlier experiments where voltage was not introduced into the system. In essence, the root causes of water quality lie within the circuit's inherent characteristics, rather than being a direct consequence of electrical potentials applied to it.

6.4 Primary Circuit PC03

To understand the entity of water contamination, the results obtained from "bypass/stainless steel only" experiments were compared with the circulation experiments performed on a SPIDER circuit that was not heavily contaminated. Circulation experiments and trace metal analysis with ICP-MS were performed in PC03 circuit using the same methodology used in PC01.

6.4.1 Circulation Experiments

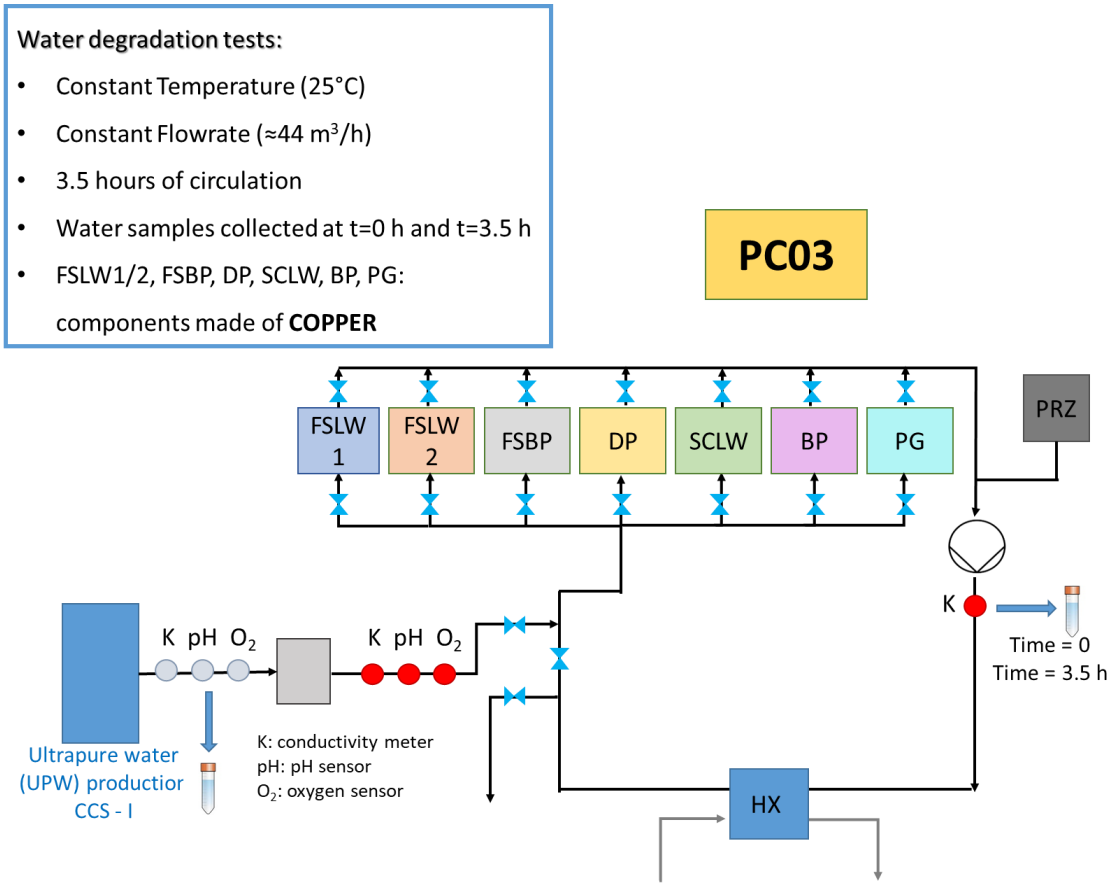

Figure 6.11: Sketch of PC03 circuit

Circulation experiments were systematically carried out under controlled conditions, maintaining a consistent temperature of 25°C and a steady flow rate of approximately 44 m³/h. This experiment was repeated twice.

PC03 considers several copper components: namely, Faraday Shields Lateral Walls (FSLW), Faraday Shield Back Plate (FSBP), Driver Plates (DP), Source Case Lateral Wall (SCLW), Bias Plate (BP), and Plasma Grid (PG), all primarily constructed from copper material. A sketch of PC03 is reported in Figure 6.11.

The outcomes of circulation experiments are graphically presented in Figure 6.12. Copper concentrations measured by ICP-MS in water samples from PC01 "*Bypass only*" experiments, where no copper components are incorporated into the circuit, were found to exceed the Cu levels measured in water samples from PC03 circulation experiments, even though PC03 featured several copper components in the circuit. In specific terms, the copper

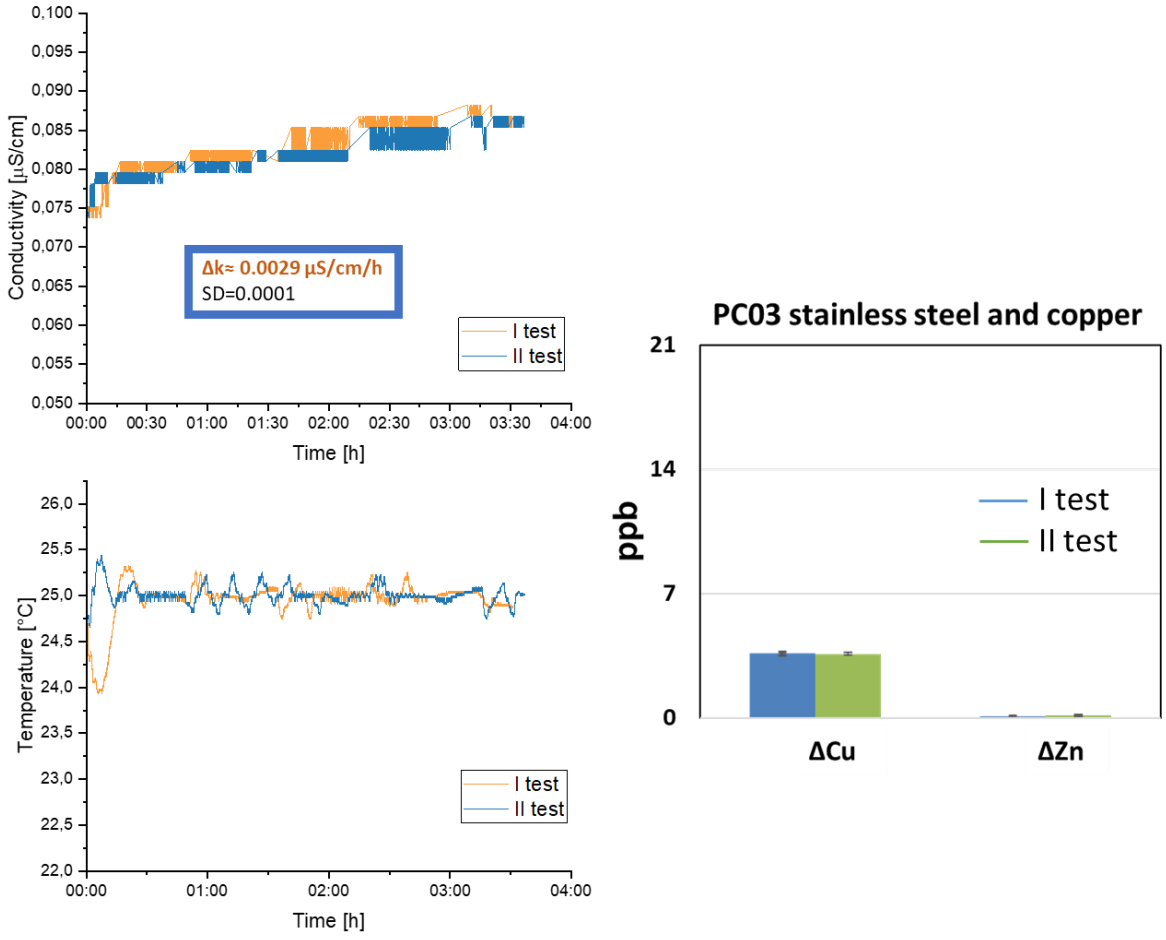

Figure 6.12: Water conductivity trends in SPIDER PC03 circulation experiments (left) and Cu and Zn released during the experiments (right)

release during PC03 circulation experiments was ΔC_{Cu}, PC03 = 3.61 ± 0.12 ppb, which corresponds to a daily copper release in PC03 equal to $Cu_{release}$= 0.73 μg·cm^{-2}·day^{-1}.

Comparing conductivity trends in PC01 and PC03, the conductivity increase rate (Δk) was quantified, with PC01 "*Bypass only*" experiments yielding a Δk = 0.0133 ± 0.0012 μS·cm^{-1}·h^{-1}, while PC03 exhibited a notably lower Δk = 0.0029 ± 0.0001 μS·cm^{-1}·h. These findings strongly indicate that the conductivity increase in PC01 is related to the high copper release in PC01 due to the contamination of the circuit with undesired materials. Corrosion by-products originating in ISEPS have propagated throughout the entire PC01 circuit, ultimately affecting water conductivity measurements.

6.5 Oxygen Estimation in PC01: Backflow Circulation Test

SPIDER water chemistry characteristics are quite stringent, since water conductivity for W-I should be within 0.1 ÷ 0.2 μS/cm, pH should be neutral (between 6.5 ÷ 7.5) and the oxygen concentration should be very low (< 50 ppb). Dissolved oxygen is detrimental especially for copper components since it affects copper corrosion rates [53], [59]. SPIDER primary cooling circuits, however, are not equipped with any O_2 sensor or pH sensor in line. The only parameter monitored so far in the primary cooling circuits is water conductivity.

In order to check water quality in SPIDER primary circuits, backflow experiments were designed and conducted. A backflow experiment involve back-flowing the water from the primary circuits towards the sensors installed after the 7m^3 tank used to store UPW from CCS-1. It is necessary to back-flow the water towards the O_2 and pH sensors called MAN0005 and MAP0005 since they are the only ones available in the plant. Figure 6.2 and Figure 6.13 report the location and name of pH, O_2 and conductivity sensors named MAP0005, MAN0005 and MAC0007 respectively. In Figure 6.13 it is possible to see the results from a backflow experiment conducted in PC01 water on 26th November 2020. Water from PC01 circuit was back flowed in the morning and at the end of the day towards the sensors called MAC0007 (conductivity sensor), MAN0005 (oxygen sensor) and MAP0005 (pH sensor) to monitor water quality. MAP0005 was broken so, unfortunately, the pH of PC01 water could not be monitored. To backflow the water from the primary circuits towards MAC0007 and MAN0005 sensors it is necessary to stop the main circuit pump and use the small pumps used to refill PCs with UPW. These pumps allow a flow rate of approximately 3.6 m^3/h when used together. Given that PC01 flowrate is usually 75 m^3/h, water was back flowed for approximately one hour to make sure that most of the water from PC01 circuit was sampled in MAC0007 and MAN0005.

Dissolved Oxygen (DO) was present in PC01 water from the morning as can be seen in Figure 6.13. Unfortunately the transmitted values for dissolved oxygen stopped at 2000 ppb. This upper limit value has been established for the MAN0005 sensor transmission

because it was not expected that DO levels in SPIDER primary circuit water would significantly exceed this threshold. After an entire day of water circulating in PC01 the concentration of DO was still very high and well beyond 2000 ppb: it was recorded a DO value in PC01 water of 13 000 ppb (= 13 ppm).

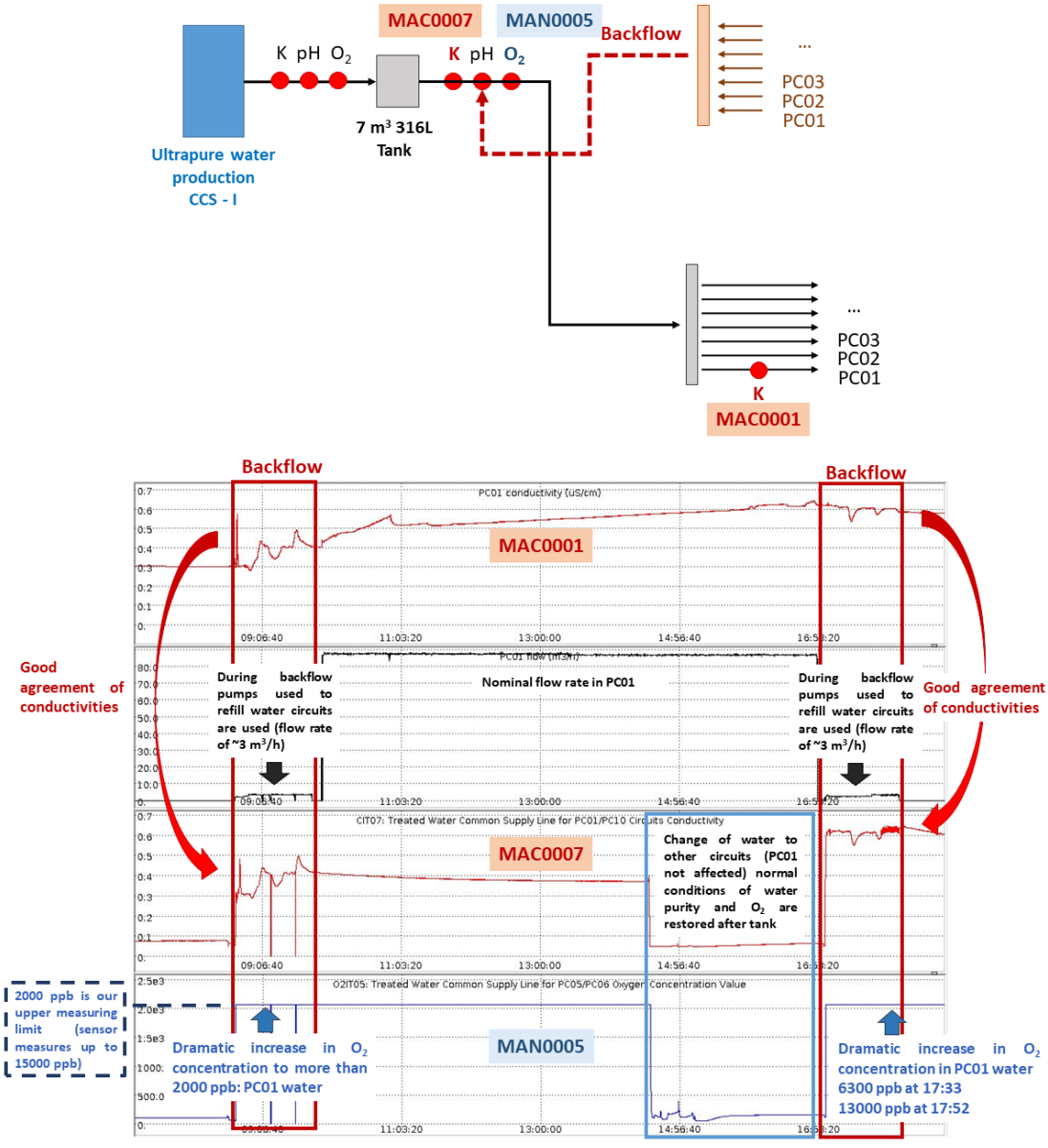

Figure 6.13: Schematic of a backflow experiment: water from the circuit (in this case PC01) is back flowed towards the sensors installed after the 7m^3 tank used to store UPW. The backflow is used to monitor water quality circulating in PC01. It is shown that in this day (26th November 2020) air was present in PC01 circuit since the oxygen concentration in water went up to 13 ppm.

Other backflow experiments were conducted between December and January in other circuits and, in all circumstances, the DO in SPIDER primary circuits water was well beyond the requested value of 50 ppb.

For this reason, in line oxygen and pH sensors were installed on SPIDER primary circuits to allow close monitoring of water quality during SPIDER experimental campaign with the aim to implement solutions to minimize dissolved oxygen in water. Backflow experiments cannot be performed during SPIDER experimental campaign since this requires the stop of the cooling circuit to allow back-flowing of the water. These sensors will be exploited and testes for the first time as SPIDER will start operating again at the end of 2023.

6.6 Discussion

The primary circuits of SPIDER have experienced significant degradation of water quality during operation. To investigate the source of this degradation, a preliminary assessment was conducted. This assessment involved calculating the wetted areas constructed from copper and stainless steel, as well as determining the volumes within PC01, PC02, and PC03 circuits. Subsequently, the corroded mass in these circuits due to general corrosion was estimated based on corrosion rate data from existing literature. The increase in conductivity resulting from the calculated corroded mass was then compared to the actual data obtained during SPIDER's operation.

In the case of circuits PC02 and PC03, there was a notable agreement between the theoretical predictions and the experimental water degradation. These circuits exhibited experimental water conductivity degradation that was respectively 0.5 and 0.67 times less than what was estimated. For circuit PC01 the real water conductivity degradation is instead 6.4 time higher than expected, indicating that further investigations must be carried out to identify the cause of the issue.

To further investigate the water degradation in SPIDER's PC01 circuit, circulation experiments were conducted under controlled conditions, including a constant temperature of 25°C, a flow rate of 75 m^3/h, and a water conductivity of approximately 0.06 µS/cm at 20°C. This methodology demonstrated consistent and robust results.

The analysis of water sampled from PC01 during these experiments, with the insertion of ISEPS in the circuit, revealed a significant increase in the concentration of ions, primarily composed of copper and zinc, as measured by ICP-MS analysis. After 3.5 hours of circulation, the increase in ion concentration was quantified as $\Delta C_{Cu} = 11.8 \pm 1.5$ ppb and $\Delta C_{Zn} = 1.89 \pm 0.3$ ppb.

Further investigation into the source of corrosion products identified galvanized plates, carbon spring steel, brass components within ISEPS pressure reducers, and plastic

containing zinc oxide particles. These components were found to contribute to the presence of iron oxides, zinc oxides, and copper oxides, as characterized by SEM-EDX and XRD analysis. The measured copper release and conductivity in PC01 experiments with "*ISEPS in*" at T = 25°C were $Cu_{release,\ PC01}$ = 1.84 $\mu g \cdot cm^{-2} \cdot day^{-1}$ and $\Delta k_{PC01\ exp}$ = 0.0210 ± 0.001 $\mu g \cdot cm^{-1} \cdot h^{-1}$. In "*Bypass only*" configuration, with only stainless steel included in the water loop. the conductivity increase was $\Delta k_{PC01\ exp}$= 0.0133 ± 0.0012 $\mu g \cdot cm^{-1} \cdot h^{-1}$ accompanied by ΔC_{Cu} = 7 ± 1.1 ppb.

By applying the same methodology to PC03 circuit, where no corrosion issues were detected, and several copper components are installed, it was found that copper release from general corrosion/erosion of copper was lower than PC01. $\Delta C_{Cu,\ PC03}$ = 3.61 ± 0.12 ppb, which is equal to $Cu_{release,\ PC03}$ = 0.73 $\mu g \cdot cm^{-2} \cdot day^{-1}$ accompanied by $\Delta k_{PC03\ exp}$= 0.0029 ± 0.0001 $\mu g \cdot cm^{-1} \cdot h^{-1}$.

Subsequently, experiments were conducted on PC01 water circulation with the application of voltage. These tests revealed that the deterioration in water quality was unrelated to the application of voltage within the circuit. Instead, it was conclusively linked to the specific hydraulic configuration of the circuit itself.

This confirmed that the high copper releases were indeed related to the presence of undesired components. While some of these components were already identified and replaced, others remain to be detected and addressed.

Backflow test in PC01 highlighted that air enters the water flowing in the circuit, leading the DO quantity over the maximum value set as "readable" for the oxygen sensors. In-line sensors were mounted on PC01 in order to measure pH and O_2 during SPIDER operation. These sensors will be tested for the first time when SPIDER will come back to operate at the end of 2023.

Chapter 7
MITICA Cooling Plant Water Degradation

MITICA is under realization at the Neutral Beam Test Facility (NBTF) at Consorzio RFX, in Padua and comprises several components made with different materials, mainly copper, stainless steel and some plastic pipes, coupled together. MITICA operates at electrical potentials up to –1 MeV [14], [84].

The initial operation of the MITICA cooling plant began with the cooling of Power Supplies (PS) that were already installed. However, the cooling circuit of the PS, called PC08, quickly revealed a significant issue: water degradation occurred at a much faster rate than initially estimated during the design phase. Within just a few hours of operation, the water's conductivity exceeded the upper limit of 0.3 μS/cm. To address this critical problem, a dedicated experimental campaign was launched to investigate the root causes of water degradation within the MITICA cooling circuit PC08. Subsequently, various improvements and measures were implemented to mitigate this issue.

7.1 Primary Circuit PC08

MITICA Primary Circuit (PC) that cools down MITICA Power Supplies (PS) is called PC08. Ultrapure (UPW) water is used as coolant in MITICA PCs [18], with a conductivity of 0.055 μS/cm at 25 ◦C produced by an in-house purification system called chemical control system (CCS). UPW was chosen thanks to its good thermal properties and to insulate f in-vessel components at different voltage levels by limiting the leakage current.

MITICA Power Supply (PS) is a complex system, presenting a variety of insulation technologies (oil, SF6, air, vacuum) and it comprises, as reported in Section 1.4.5: the Acceleration Grid Power Supply (AGPS), the High Voltage Deck 1 (HVD1) and the 100 m long SF6 insulated Transmission Line (TL). The HVD1, polarized at 1 MVdc, hosts the Ion Source and Extraction Power Supply system (ISEPS), which is at -1MV potential and it provides power to the Ion Source for production and extraction of the negative ions [85], [86]. The TL transmits the power provided by ISEPS to the NBI. The main power supplies which compose the ISEPS system are:

- Radio Frequency Power Supply (ISRF): one unit with four RF generators;
- Extraction Grid Power Supply (ISEG): one unit;

- Plasma Grid Filter Power Supply (ISPG): one unit;
- Bias Power Supply (ISBI): one unit;

The other power supplies are:

- Filament Heater power supply (ISFH): one unit;
- Filament Bias power supply (ISFB): one unit;
- Core Snubber Bias circuit power supply (ISS1, ISS2): two units.

The ISPG, ISBI, ISS1, ISS2, ISFH and ISFB compose the Source Support Power Supply (ISSS). HVD1 has an overall height of about 12 m and a total weight of 19 t [87], [88].

After having performed the voltage holding tests in 2018 and 2019 by applying voltage with the Testing Power Supply (TPS) generator, the integrated tests of the Acceleration Grid Power Supply (AGPS) of MITICA high voltage power supplies started in 2021. These tests required active cooling of some of the power supplies referred to the accelerating potential contained inside the HVD1. Water conductivity was monitored all along the tests to avoid excessive current drainage from the high voltage TPS, that would otherwise limit the available output voltage at the TPS [86], [89]. This commissioning

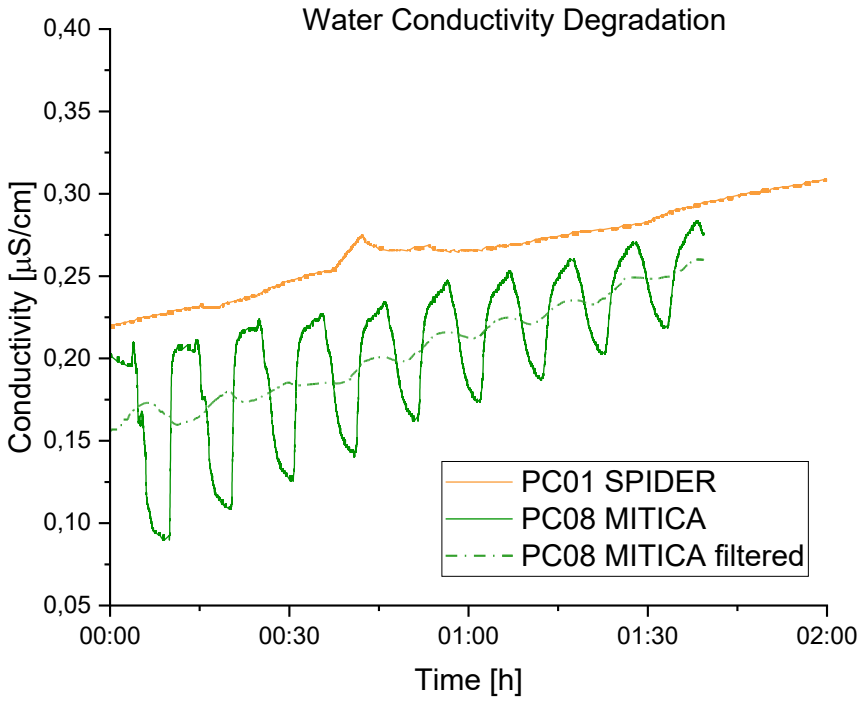

Figure 7.1: Water conductivity degradation in PC01 and PC08 during an experimental day, at constant temperature

highlighted a strong water degradation as severe as the one already observed in SPIDER PS Circuit called PC01, as shown in Figure 7.1 [22] . PC08 conductivity signal was filtered to remove the oscillation noise caused by a long water mixing time in the pipeline volume, which is five time bigger with respect PC01 one. PC08 conductivity operation limit is equal to 0.3 μS/cm at 25°C and, when this limit is exceeded, MITICA high voltage test needed to be stopped for injection of ultrapure water to restore water conductivity. This recurring need for water replacement poses a pressing challenge for future MITICA operations, as it consumes about 2 hours and 30 minutes of time and must be completed before the commencement of daily experimental sessions.

Also for PC08, an ad hoc experimental campaign was proposed and conducted to address the issue of water degradation in MITICA PC08. PC08 was divided into different branches to isolate each component, aiming to identify the potential source of water degradation while water was circulating in the circuit. All tests were conducted without applying any voltage.

Circulation tests were performed under constant temperature, pressure, and flow rate conditions. Water samples were collected at the beginning and conclusion of each experimental day and subjected to analysis using Inductively Coupled Plasma Mass Spectrometry (ICP-MS) to detect trace metal concentrations in parts per billion (ppb). Additionally, experiments on metal release were carried out to assess potential contamination from various types of plastic tubing used throughout PC08. The outcomes of these experiments were cross-verified through plastic characterization using SEM.

In addition to these investigations, a different set of circulation experiments was conducted by altering the pressurizer operating pressure, and yet another series of experiments implemented mixed bed resins within the circuit to purify the water by removing anions and cations. These comprehensive efforts were aimed at identifying and addressing the root causes of water degradation in MITICA PC08.

7.1.1 Circulation Experiments

Circulation experiments were conducted at a constant temperature (T = 25°C) and flow rate (~60 m^3/h), with ultrapure water injected into the circuit before each test to initiate the experiment with a conductivity of 0.16 μS/cm. Each experiment was replicated three times. As for water circulation tests performed for PC01, water samples were collected prior to any experimental day at time = 0, when water conductivity was 0.16 μS/cm, and at the experiment's conclusion after 3 hours and 30 minutes of circulation, as previously performed for PC01 and reported in Section 6.3.

During water circulation tests, the water loop exclusively integrated the Source Support Power Supply (ISSS) and Extraction Grid Power Supply (ISEG). The design approach prioritized simplicity for the water circuit, employing solely plastic, copper, and stainless steel materials in direct contact with the cooling water. Notably, all liquid cold plates and water heatsinks in the Power Supplies and in the RF Generators have copper in contact with the water.

Figure 7.2 illustrates the layout of PC08 during the execution of water circulation tests. These experiments were carried out based on two distinct configurations:

1. *"PS inclusion"* configuration: ISSS and ISEG were exposed to UPW, resulting in the wetting of copper, stainless steel, and plastic tubes by UPW.
2. *"Bypass-only"* configuration: the water loop excluded ISSS and ISEG. Consequently, only stainless steel and plastic piper were wetted by UPW

To assess the repeatability and robustness of the implemented experimental procedure, three distinct circulation experiments were conducted for each configuration. These experiments were carried out on various days or months, all while ensuring that the initial conditions remained consistent.

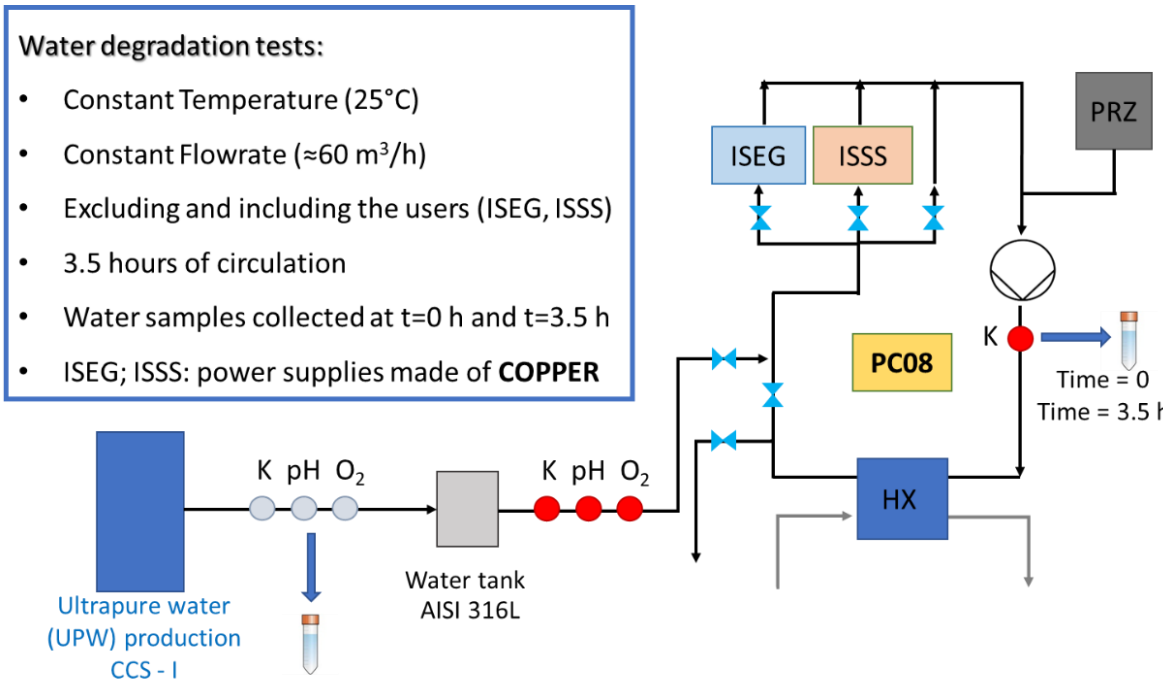

Figure 7.2: PC08 scheme when water circulation tests were performed. PRZ stands for "pressurizer" and HX for "Heat Exchanger"

The increase in conductivity during circulation experiments and the corresponding temperature profiles are presented for each tested configuration in Figure 7.3. The trend in conductivity showed distinct oscillations with a periodicity of approximately 5 minutes, as depicted in Figure 5. These oscillations can be attributed to mixing challenges within the circuit's volume during water replacement. This periodicity is estimated to be closely related to the time required for a specific volume of water to traverse the entire circuit. The results, presented for both *"PS inclusion"* and *"Bypass-only"* configurations, reveal comparable degradation trends (Δk_{PS} = 0.047 ± 0.002 $\mu S \cdot cm^{-1} \cdot h^{-1}$, and Δk_{bypass} = 0.041 ± 0.007 $\mu S \cdot cm^{-1} \cdot h^{-1}$), highlighting marginal improvements when the PS modules were excluded from the water loop.

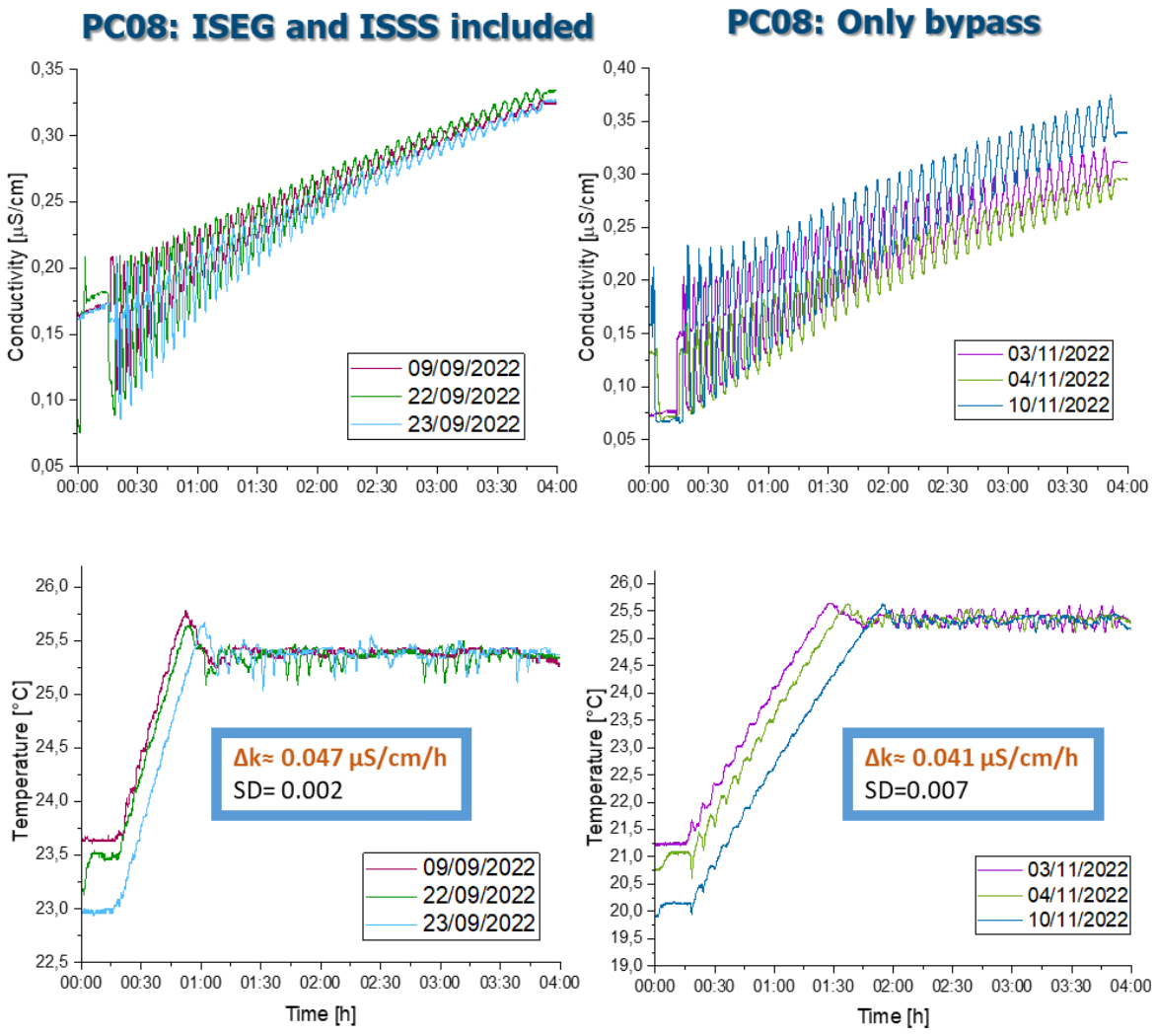

Figure 7.3**:** Water conductivity trends in MITICA PC08 circulation experiments (top) and temperature profiles during each test (bottom)

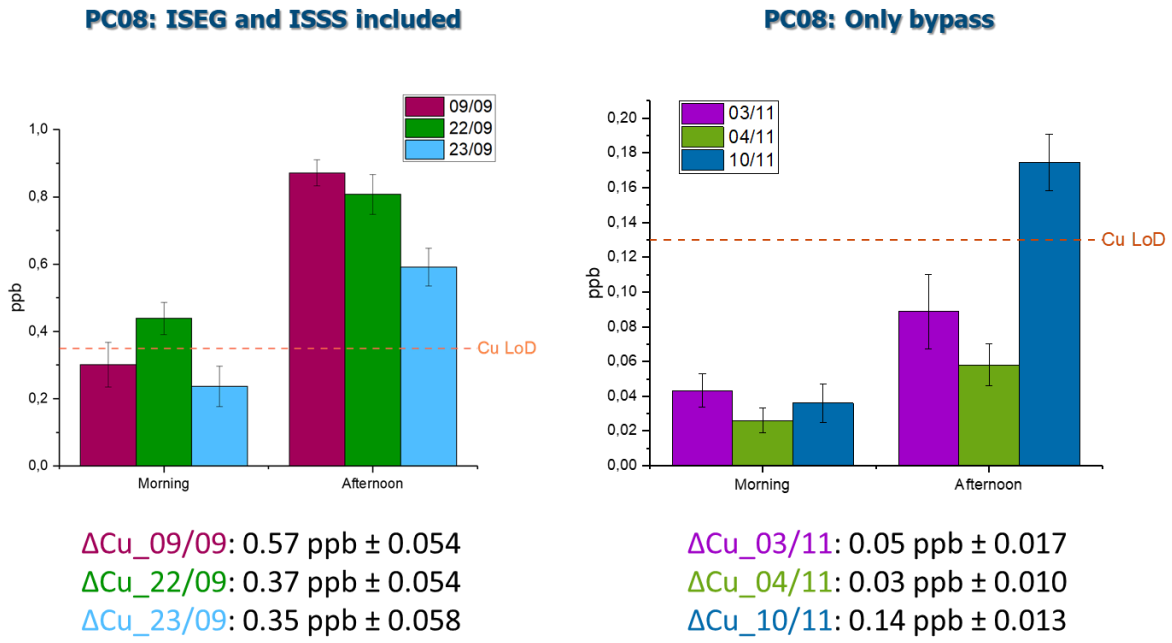

Figure 7.4: ΔCu average and Standard Deviation (SD) values measured by ICP-MS on water sampled from circulation experiments

Figure 7.4 reports the concentrations of trace metals quantified with ICP-MS on water samples. For this study, only some cations were quantified with copper being the sole metal detected above the instrument's Limit of Detection (LoD). The ICP-MS findings underscore that, within the context of these circuits, no observable correlation exists between the cation metals released into the water and the noted increase in conductivity.

When comparing the findings presented in this study with those of a similar previous campaign conducted in the SPIDER Primary Circuit, referred to as PC01 (Section 6.3), a notable observation emerges. While both circuits exhibited strong degradation in conductivity, the quantified increment in copper content prior to and following the experiment involving ISEG and ISSS inclusion is two orders of magnitude lower in PC08 than the copper increase recorded in PC01, in *"All-in"* configuration (ΔCu_{PC01} = 11,8 ± 1.7 ppb; ΔCu_{PC08} = 0.43 ± 0 .055 ppb). Consequently, the primary source of water degradation in MITICA PC08 cannot be attributed to the release of cation metals into the water like it was reported for PC01. Instead, the potential influence of inadequate water chemistry control was taken into account.

Figure 7.4 illustrates that, within the *"Bypass-only"* configuration, that do not comprises copper components in the water loop, traces of copper consistently remained below the LoD throughout all experimental days, with the exception of the final day

(10/11/2022), during which it was detected at approximately 0.14 ppb in the afternoon. This presence of copper on the last day can be attributed to an error occurring during the manual water change executed in the morning, inadvertently introducing air, and consequently oxygen, into the circuit. This introduction of oxygen was measured by the oxygen sensors integrated within the water fill line and located after the $7m^3$ water tank (Figure 7.2). The repercussions of this error can also be observed in Figure 7.3, where the concluding day of the *"Bypass-only"* configuration experiment (10/11/2022) exhibited a more pronounced degradation in conductivity in comparison to the preceding days. This phenomenon can be elucidated by recognizing that, as described in Section 3.2.2, a significant component of air is carbon dioxide (CO_2), which readily dissolves and reacts with water to generate H^+ ions. This, in turn, leads to an escalation in proton concentration, resulting in a decrease in pH and ultimately an elevation in conductivity [32], [92].

The introduction of air may have also influenced the release of copper into the water, as detected on the experiment day 10/11. In an oxygen-free environment, copper remains stable and does not corrode when in contact with pure water. However, in the presence of oxygen, copper oxides are formed, which gradually dissolve in the water [55], [59]. The influx of air, along with oxygen, might have prompted the release of copper ions, causing a shift in the water's pH. Formation of the copper ion occurs from the oxide state when pH is just below 7.0. Under these conditions, the replacement of oxygen within the oxide state occurs readily [31]. These ions could have potentially migrated from the copper surfaces of the PS and subsequently redeposited along the PC08 circuit during earlier operational phases.

The copper metal release tests conducted in both oxidizing and reducing environments (Section 5.3.2) unveiled a distinctive trend in copper release into the water. In an oxidizing environment, this led to the formation of tenorite on the copper samples, whereas in a reducing environment (with dissolved oxygen levels lower than 50 ppb in water), cuprite was observed (as depicted in the above Section 5.3.3). These findings not only validate the potential explanation for the detection of copper in water on the experiment day 10/11, with the copper PS excluded, but also confirm that the primary degradation of water in MITICA PC08 can be attributed to a deterioration of water chemistry. Thus, an improvement in water chemistry control is necessary. One promising solution that was considered and tested was to raise the working pressure within the system, particularly taking into account the elevated position of HVD1 by 12 meters (Section 0). This adaptation has the potential to decrease the chances of air infiltration into the system from its highest point, consequently aiding in the preservation of the desired water chemistry conditions. Another improvement considered and implemented is the insertion of online mixed bed resins (Section 7.2.2).

7.1.2 Plastic Tubes Analyses

As previously mentioned, MITICA PC08 incorporates not only copper and stainless steel components but also various types of plastic tubes, categorized as follows:

- A heat resistant, white Ethylene-Propylene Diene Monomer (EPDM) Rubber-Compound electrically non-conductive. It is employed to insulate the HVD1 Faraday Cage.
- A green Polypropylene-Random Crystallinity Temperature (PP-RCT) tube with high performance and resistance to temperature and pressure. This type of tube is used to reduce the overall weight of the tubes that have been anchored on the walls.

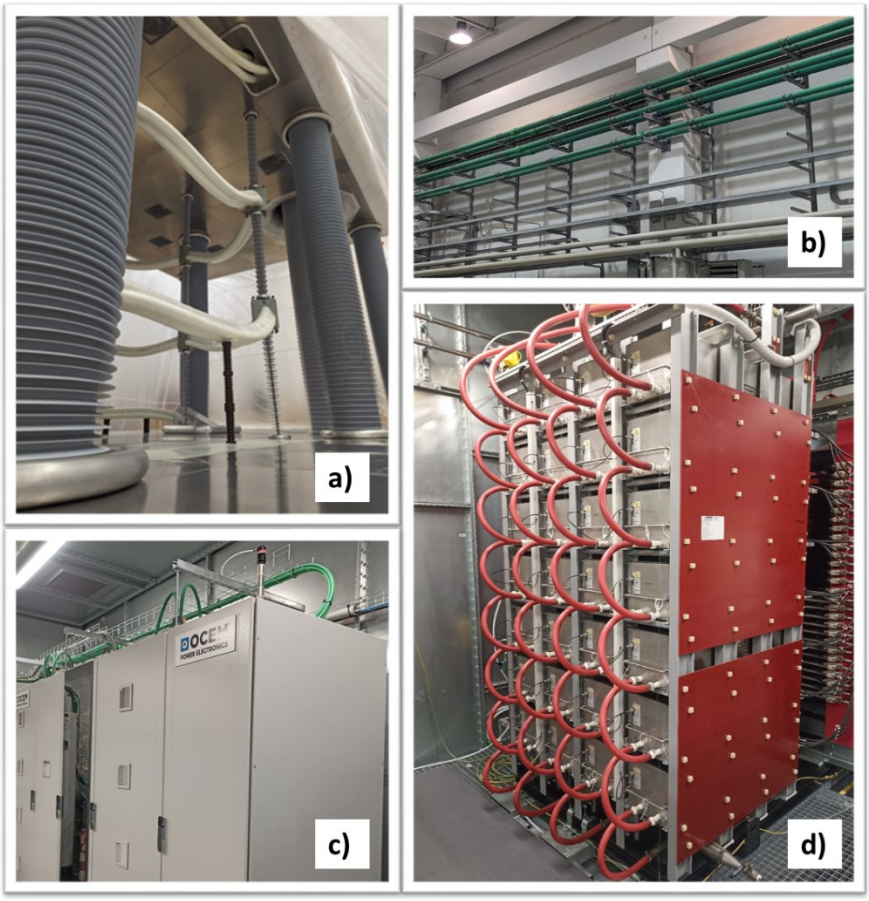

Figure 7.5: Plastic tubes used in MITICA PC08. a) EPDM white rubber, b) green PP-RCT; c) green NBR in ISSS module; d) red NBR in ISEG module

- A second green type of tube characterized by an inner hose in black Nitrile Butadiene Rubber (NBR), a polyamide intermediate braid and an outer cover in Hydrogenated Nitrile Butadiene Rubber (HNBR). It is used to isolate the ISSS module. It is the same used for SPIDER PC01 ISSS.
- A red type of tube made of internal hose in NBR and a cover in nitrile. It is utilized to insulate ISEG module. It is the same used for SPIDER PC01 ISEG

As already did for SPIDER PC01, the potential impact of plastic tubes on water degradation was examined by collecting water samples from these tubes after they had been stagnant for at least 2 days. The analysis revealed higher-than-expected levels of copper and zinc traces, as depicted in Figure 7.6a. Visual examination of the plastic connections revealed red deposits, which were subsequently identified as copper residue redeposited onto PS surfaces, as shown in Figure 7.6b.

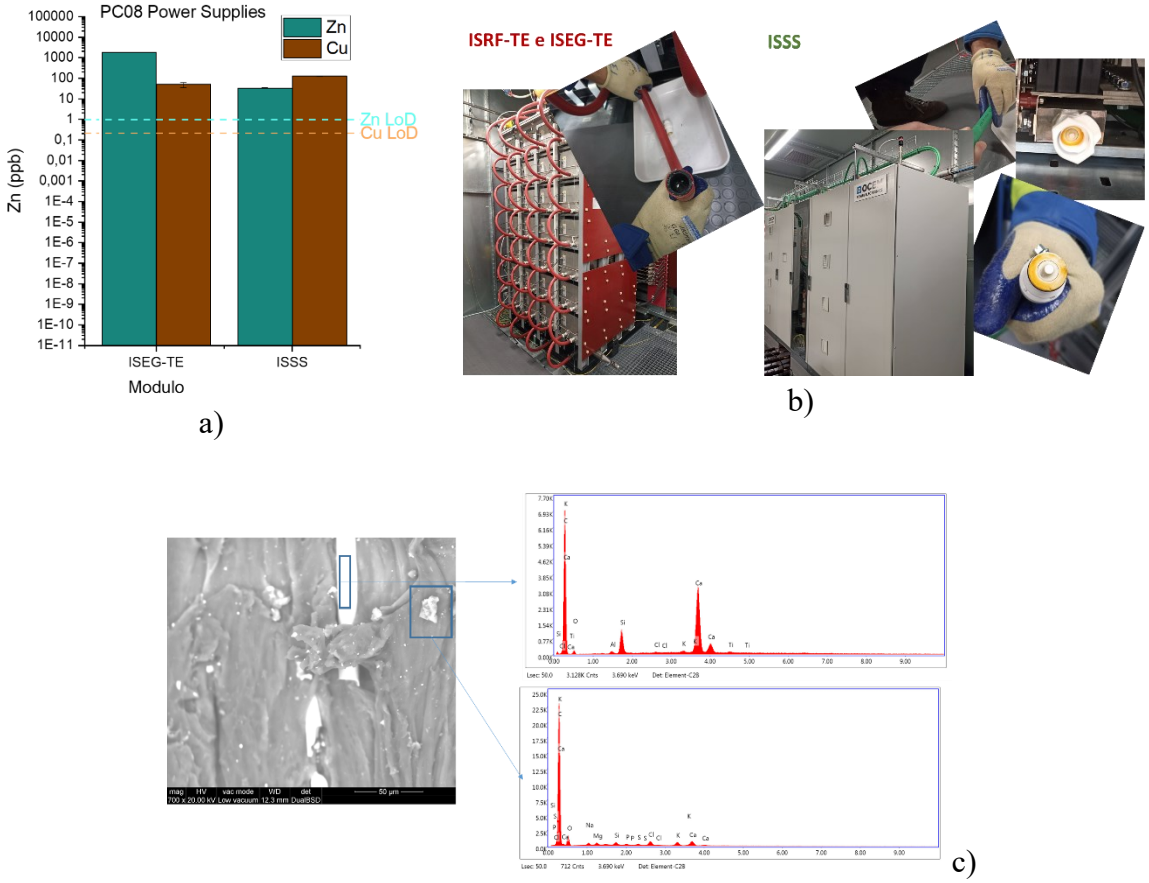

Figure 7.6: Plastic tubes analyses. a) water samples analyses of stagnant water collected from tubes type in ISEG and ISSS; b) visual inspection of tubes; c) SEM-EDX analyses of type b) tube

The analyses previously presented, focusing on plastic tubes of types c) and d) within .Primary Circuit PC01, provided conclusive evidence of the presence of zinc particles embedded in the plastic matrix. However, during the water circulation tests conducted in PC08, no traces of zinc were detected. This variance can be attributed to the relatively short length of the plastic tubes in PC08 in comparison to the overall volume of the circuit (V_{PC08} = 5.6 m^3, whereas V_{PC01} = 1.1 m^3). As a result, any zinc ions present would have been significantly diluted within the entire water volume, rendering them undetectable in the analyses.

Nevertheless, it's essential to exercise caution and not dismiss the presence of zinc altogether. Even though zinc was not detected during these specific tests, it still has the potential to contribute to localized corrosion concerns, such as pitting and crevice corrosion. These issues could emerge in future operations if not properly addressed.

Figure 7.6c showcases the SEM-EDX analyses of type b) tubes, which are anchored on the walls of the circuit. These tubes were found to contain calcium carbonate and potassium carbonate particles, added for mechanical reinforcement purposes. Importantly, these green tubes affixed to the walls did not exhibit any zinc particles within their matrix. Therefore, this type of plastic material appears to be suitable for use with ultrapure water.

7.2 Improvements Primary Circuit PC08

Several enhancements were suggested and experimented with on Primary Circuit PC08 to mitigate the ingress of air and manage the deterioration of water conductivity. The initial modification, which has now become a permanent change, involved raising the pressurizer's operating pressure to minimize potential air ingress from the circuit's highest point. Another tested improvement involved the installation of online resins to consistently extract ions from the water, thus maintaining its conductivity at a constant level.

7.2.1 Circulation Experiments with Working Pressure Increased

The ISEPS system, situated on a 12-meter elevated platform hosted by HVD1, spans an area of 12 meters by 10 meters. This platform is intentionally isolated from the ground for electrical insulation purposes, achieved through the use of helical pipes and by maintaining a separation from adjacent walls. A schematic representation of PC08, highlighting the elevation differences, is depicted in Figure 7.7.

According to the original design, the pressure set at the pressurizers has consistently been maintained at P_{PRZ}=2.5 bar during operation. This pressure level has also been employed in all prior circulation experiments. When the circuit was not in operation, a control logic

system promptly enforced a P_{PRZ} of 2.5 bar to maintain circuit pressure. Consequently, at the highest point of the circuit, the pressure was maintained at 1.3 bar.

During the circuit's design phase, it was initially assumed that this pressure setting would be adequate to prevent the entry of air into the circuit. However, practical observations revealed significant oscillations in the readings of flowmeters positioned along the pipelines. According to the instrument datasheets, such oscillations occur when air infiltrates the circuit, leading to inaccurate measurements. To mitigate the potential for air ingress into the circuit, the working pressurizer pressure, P_{PRZ}, was raised to 4.8 bar during operation and further increased to 5 bar when the circuit was not in use.

New water circulation tests were recently conducted under specific conditions. These circulation experiments were carried out at a constant temperature of 20°C and a reduced flow rate of approximately 37 m³/h. The decision to decrease the flow rate was made to ensure that the maximum allowable pressure at the inlet of ISEPS was not exceeded, while taking into account the simultaneous increase in operating pressure. To compensate for the reduced flow rate during the experiments, the temperature set point was lowered to 20°C. This adjustment was made to facilitate the quicker attainment of the desired temperature set point.

The circulation tests were performed with two different pressure settings imposed at the pressurizers: a minimum pressure of 2.5 bar (P_{min}) and a maximum pressure of 4.8 bar (P_{max}). Each experiment was conducted twice to ensure reliability. Notably, these tests aimed to assess whether the new configuration was improving the degradation rate. Since previous experiments had already indicated that PC08's degradation was primarily due to water

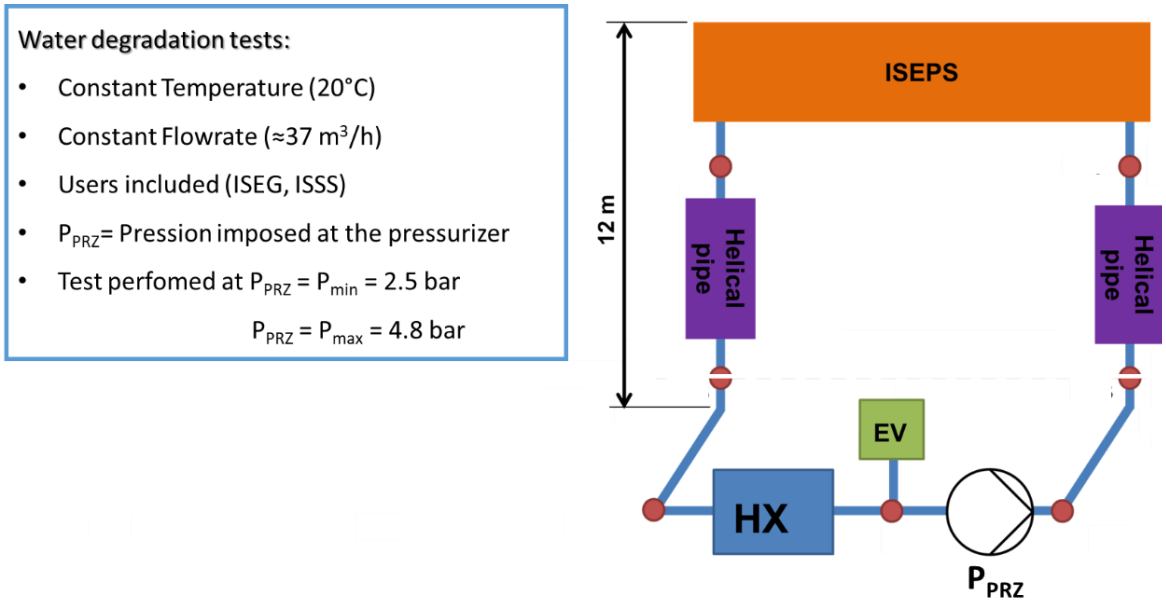

Figure 7.7: PC08 scheme with geometrical heights

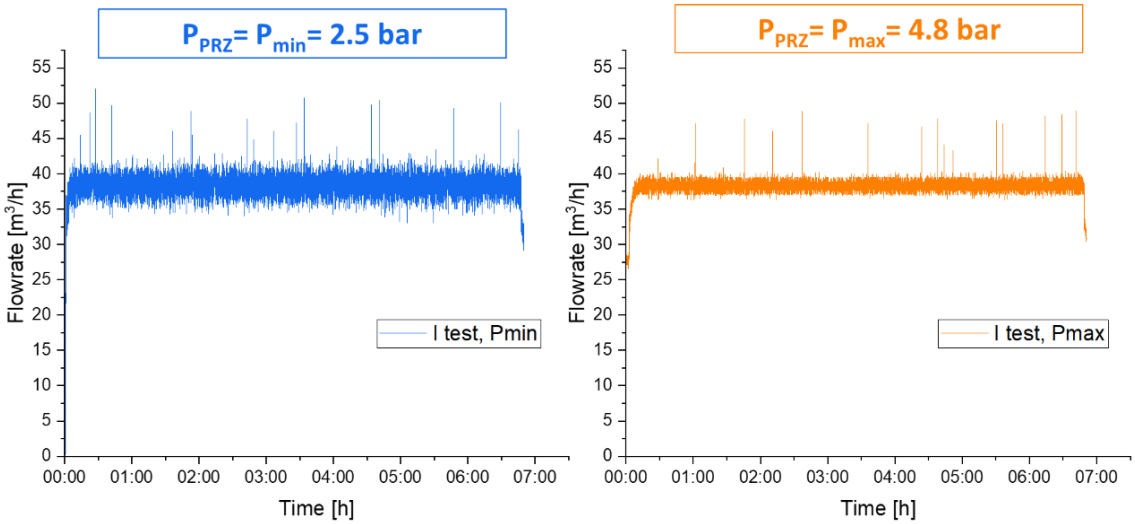

Figure 7.8: Flowrate measurements with P_{min} and P_{max}

chemistry issues rather than metal release into the water, no water samples were collected this time. As for the previous water circulation tests, the water loop exclusively integrated the Source Support Power Supply (ISSS) and Extraction Grid Power Supply (ISEG).

Figure 7.8 illustrates the flow rate trends observed at P_{min} and P_{max}. It is readily apparent that at the minimum pressure setting, the flow meters consistently displayed readings that oscillated between 35 and 42 m³/h, while at the maximum pressure setting, the flow rate oscillated between 36 and 38 m³/h. These results suggest that the hypothesis regarding the new hydraulic configuration's effectiveness in reducing air ingress into the circuit was correct.

The conductivity trends provided further confirmation of the hypothesis. Figure 7.9 presents the increase in conductivity during circulation experiments and the corresponding temperature profiles for each tested configuration. To enhance the clarity of the degradation trend, the oscillations in the conductivity trend were filtered using a moving average tool. The bold lines depict the filtered data, while the less transparent lines in the background represent the unfiltered conductivity trends. The results are presented for both "P_{max}" and "P_{min}" configurations, revealing a reduction in water degradation trends (Δk_{Pmin} = 0.031 ± 0.001 $\mu S \cdot cm^{-1}\ h^{-1}$, and Δk_{Pmax} = 0.022 ± 0.0005 $\mu S \cdot cm^{-1}\ h^{-1}$), highlighting improvements when the pressurizer working pressure is increased. However, it's worth noting that the temperature could not be maintained consistently at 20°C during some experimental days due to external temperature variations. The tests at P_{max} were conducted in June when the ambient temperature exceeded 25°C, making it challenging to keep the Secondary Circuits SCs at a temperature below 20°C. Despite this, the degradation rate was lower in the P_{max} experiments compared to the P_{min} ones.

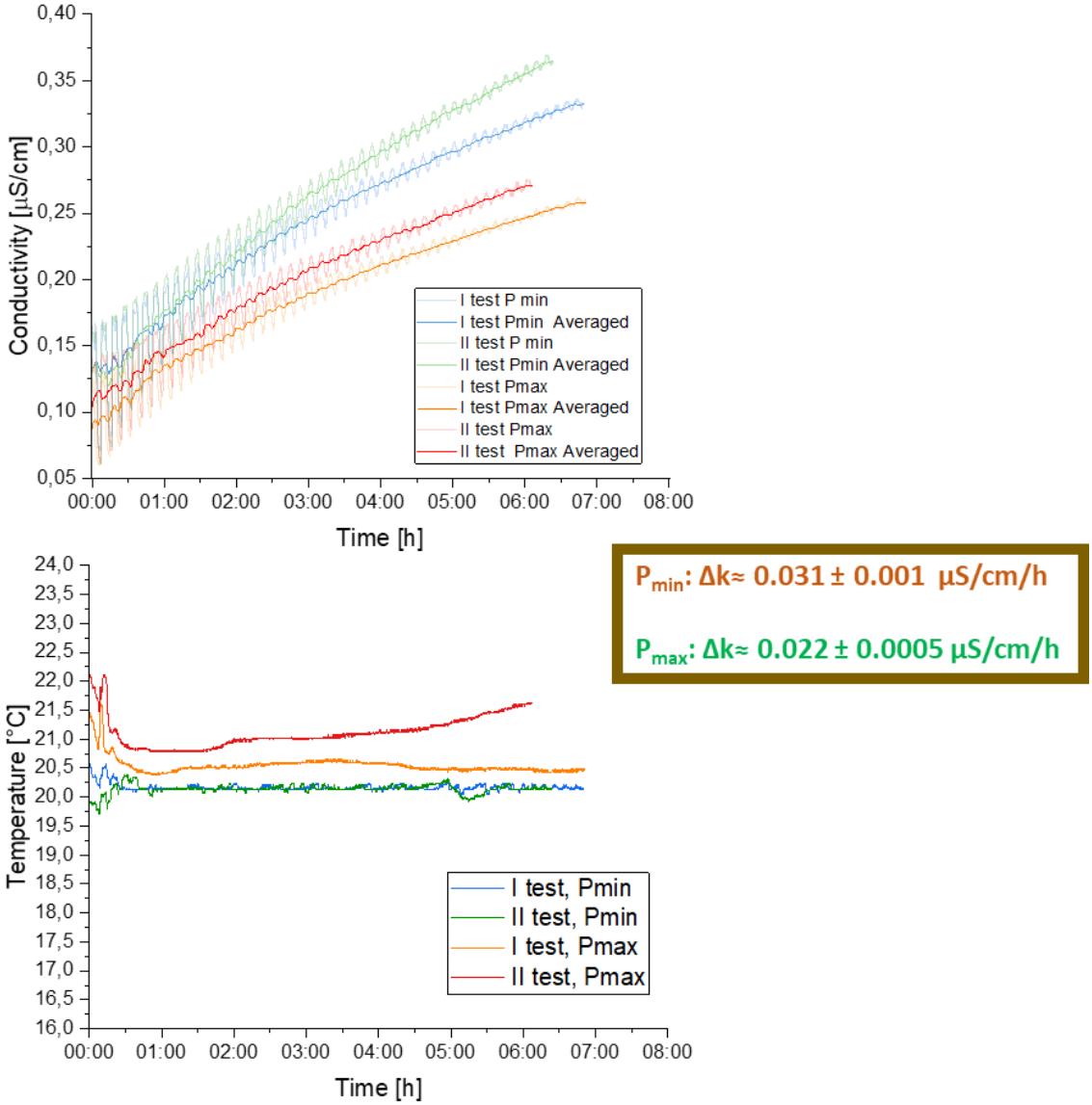

Figure 7.9: Water conductivity trends in MITICA PC08 circulation experiments (top) and temperature profiles during each test (bottom) for P_{max} and P_{min}.

The promising results helped to reach the 1MeV during MITICA high voltage test. Considering that future high voltage test will require to keep the conductivity value below 0.3 $\mu S \cdot cm^{-1}$ for at least 8 hours, the installation of mixed bed resins along MITICA PC08 was considered.

7.2.2 Circulation Experiments with Mixed Bed Resins Installed

Water degradation tests:

- Constant Temperature (20°C)
- Constant Flowrate (≈37 m^3/h)
- Users included (ISEG, ISSS)
- Resins Included
- Resins flowrate: 0.6 m3/h (1.6% of the tot flowrate)

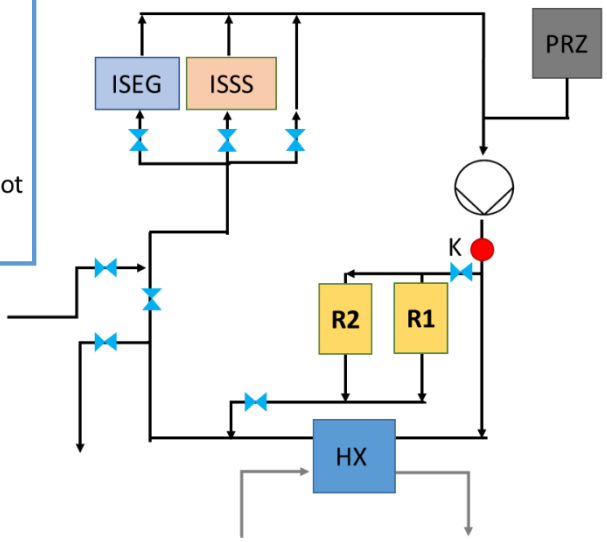

a)

b)

Figure 7.10: a) PC08 scheme when water circulation tests were performed. “R1” and “R2” stands for resin n.1 and resin n.2, b) image of the resins installed in PC08

For future high-voltage tests, it will be necessary to maintain the conductivity value below 0.3 $\mu S \cdot cm^{-1}$ for a minimum of 8 hours. To achieve this, two mixed bed resins were installed along MITICA PC08. Since the maximum working pressure for the resins is 8 bar, they were strategically placed both before and after the heat exchanger. This configuration also capitalized on the pressure drop induced in the primary circuit loop by the heat exchanger. A schematic representation of PC08 with the resins installed can be seen in Figure 7.10a, whereas Figure 7.10b reports a photo of resins mounted in the circuit. Resins were installed in parallel.

The properties of the installed resins are reported in Table 7.1.

As reported in Table 7.1 these particular resins, which are also installed offline in PC04 and PC07, are effective above a water conductivity level of 0.5 µS/cm. Regrettably, these were the only available resins in the warehouse for testing. The initial test aimed to assess the effectiveness of the new configuration and determine if the water passing through the resins could reduce the conductivity from a higher value (0.5 µS/cm) back to 0.5 µS/cm.

Table 7.1: Mixed bed resins properties

	Refill Line
Exchange Capacity	450 g as CaCO3
Maximum Flow rate	500 l/h
Treated water quality	>2 MΩ at the end of the cycle
Operating pressure	Min 1bar – max 8 bar
Operating limits	Potable water – TH < 35°f

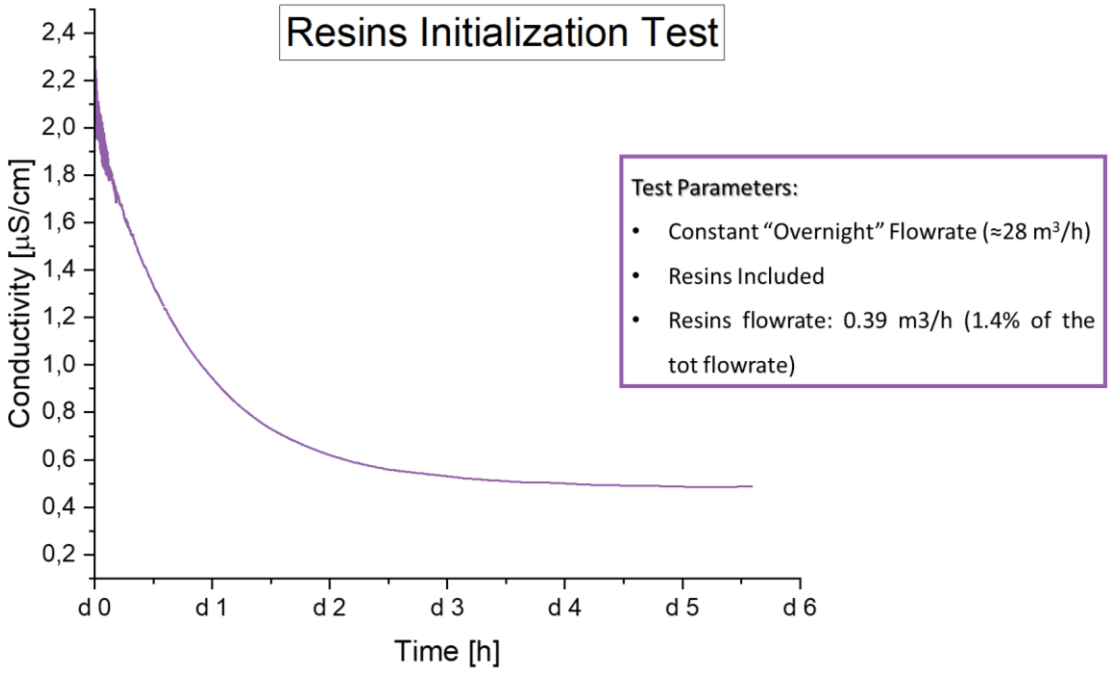

Figure 7.11: Conductivity trend in "resins initialization test". Starting conductivity value at about 2 µS/cm

The "resins initialization test" was carried out at a reduced flow rate of approximately 28 m³/h, which corresponds to the "overnight flow rate" at which PC08 operates continuously throughout the night. This allowed the effects of the resins to be observed over a span of 6 days. Inside the resins, a flow rate of 0.39 m³/h was maintained. Figure 7.11 presents the conductivity trend, demonstrating that the conductivity was successfully brought and maintained at a constant 0.5 µS/cm. Therefore, the new installation proved to be effective.

To evaluate if the resins also influenced the conductivity degradation trend below the maximum operating value of 0.5 µS/cm, further water circulation experiments were conducted. These experiments were performed under constant conditions of 20°C temperature, a flow rate of approximately 37 m³/h, and a pressurizer pressure $P_{PRZ} = P_{max} =$ 4.8 bar. Inside the resins, water was flowing with 0.6 m³/h. Similar to the previous circulation tests at different pressurizer pressures, no water samples were collected during these experiments.

The circulation tests were conducted with the resins installed under the mentioned hydraulic conditions, and the experiment was repeated twice to ensure reliability. The results were then compared with the results obtained from the previous experiment conducted at the same conditions but without the resins in the water loop.

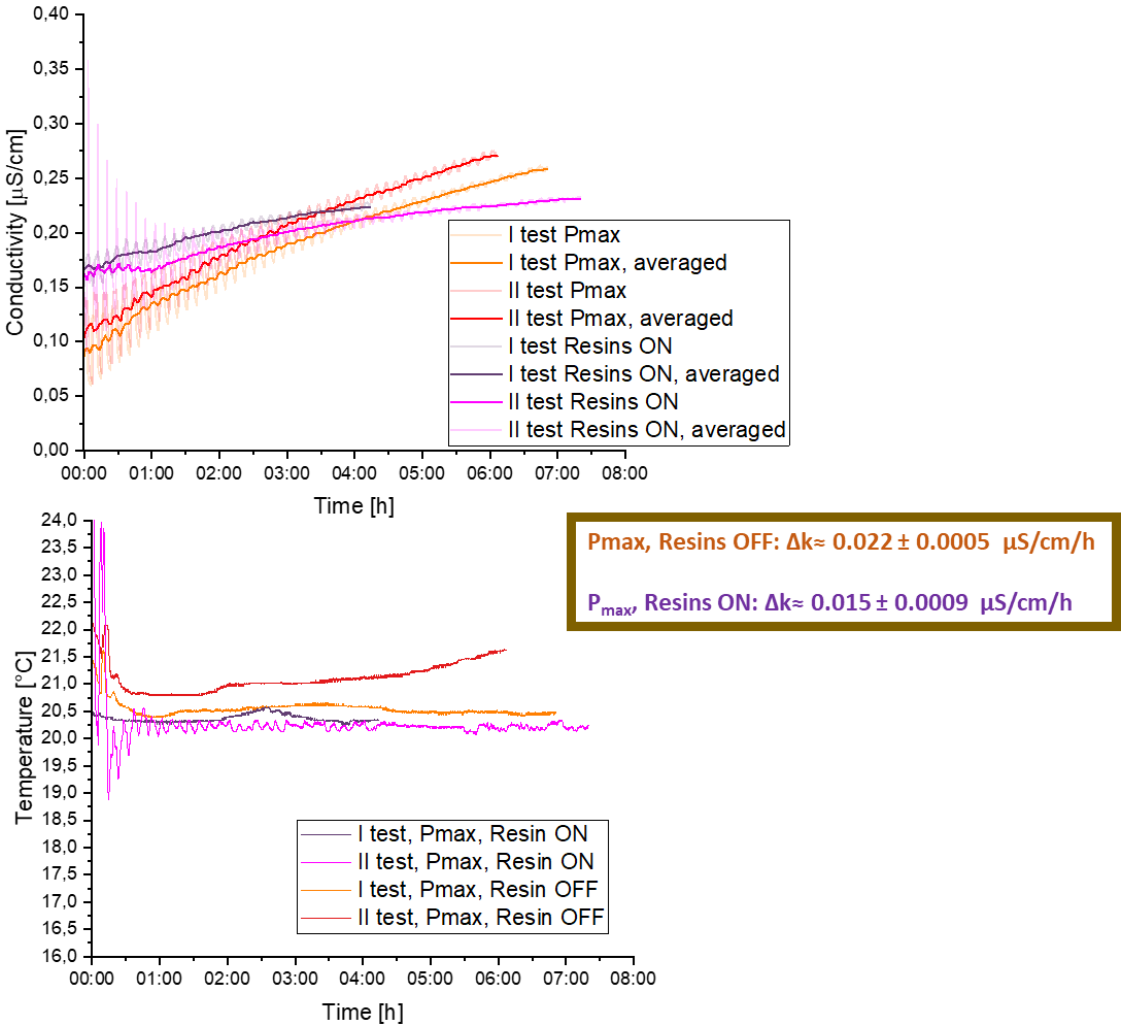

Figure 7.12: Water conductivity trends in MITICA PC08 circulation experiments (top) and temperature profiles during each test (bottom) for $P_{max,\ Resins\ OFF}$ and $P_{max,\ Resins\ ON}$

Figure 7.12 illustrates the increase in conductivity during circulation experiments and provides the corresponding temperature profiles for each tested configuration. To clarify the degradation trend, oscillations in the conductivity trend were filtered using a moving average tool. The bold lines represent the filtered data, while the less transparent lines in the background depict the unfiltered conductivity trends. The results are presented for both "$P_{max,\ Resins\ OFF}$" and "$P_{max,\ Resins\ ON}$" configurations, revealing a reduction in water degradation trends ($\Delta k_{Pmax,\ resins\ OFF} = 0.022 \pm 0.0005$ µS·cm^{-1} h^{-1}, and $\Delta k_{Pmax,\ resins\ ON} = 0.015 \pm 0.0009$ µS·cm^{-1} h^{-1}), indicating improvements when the resins are utilized. Water continues to degrade until it reaches the maximum value of 0.5 µS/cm, but this degradation is slower when the resins are included in the system. These promising results suggest the need to explore new types of

resins that can maintain water conductivity below the maximum threshold of 0.3 µS/cm, allowing MITICA PC08 to operate for the duration of high voltage tests.

It's crucial to emphasize that while the introduction of resins into the system has proven effective in managing water conductivity, it represents a short-term remedy rather than a comprehensive solution to the root problem responsible for water degradation. The true cause of the issue, which leads to an increase in water conductivity, has yet to be fully addressed.

7.3 Discussion

Initial observations from the MITICA Primary Circuit PC08 have revealed that water quality deteriorated more rapidly than initially expected. Ensuring high water quality is of paramount importance, particularly in the case of MITICA, where operations at 1 MeV demand stringent electrical insulation of in-vessel components. In order to investigate this water degradation, circulation experiments were conducted under constant conditions, including a fixed temperature of 25°C and a flow rate of 60 m³/h.

Circulation tests were performed, encompassing two different configurations: one with Power Supplies consisting of copper components ("*PS inclusion*") and another without Power Supplies, where water solely circulated through stainless steel components ("*Bypass-only*" configurations). The outcomes of these tests revealed comparable degradation trends for both "*PS inclusion*" and "*Bypass-only*" setups, with $\Delta k_{PS} = 0.047 \pm 0.002$ µS·cm^{-1}·h^{-1}, and $\Delta k_{bypass} = 0.041 \pm 0.007$ µS·cm^{-1}·h^{-}. The study's findings point towards inadequate control of water chemistry as the primary factor contributing to water degradation in MITICA PC08, rather than the release of metals. One significant factor affecting water chemistry was identified as the inadvertent ingress of air into the circuit, which could be attributed to operational errors.

Furthermore, stagnant water samples from plastic tubes within the ISSS and ISEG modules revealed unexpected traces of copper and zinc. Subsequent metal release tests on these tubes confirmed the dissolution of zinc particles in water, posing a potential risk of localized corrosion if not addressed. To mitigate this corrosion risk and ensure the long-term integrity of the system, it is under consideration to replace the existing plastic tubes with ones specifically designed for food-grade applications.

New water circulation tests were performed with two different pressure settings imposed at the pressurizers: a minimum pressure of 2.5 bar (P_{min}) and a maximum pressure of 4.8 bar (P_{max}). These tests aimed to demonstrate that increasing the working pressure reduces the ingress of air from the highest point in the system, thereby contributing to the maintenance of the desired water chemistry conditions. The results confirmed that the

degradation rate was lower in the P_{max} experiments compared to the P_{min} ones, with Δk_{Pmin} = 0.031 ± 0.001 $\mu S \cdot cm^{-1} h^{-1}$, and Δk_{Pmax} = 0.022 ± 0.0005 $\mu S \cdot cm^{-1} h^{-1}$.

Looking ahead to future high-voltage tests, it will be necessary to maintain the conductivity value below 0.3 $\mu S \cdot cm^{-1}$ for a minimum of 8 hours. To achieve this, two mixed bed resins were introduced into MITICA PC08. This approach has proven effective in managing water conductivity leading to a conductivity degradation rate of $\Delta k_{Pmax,\ resins\ ON}$ = 0.015 ± 0.0009 $\mu S \cdot cm^{-1} h^{-1}$, but it should be noted that it represents a short-term solution rather than a comprehensive resolution to the root problem responsible for water degradation. The underlying cause of the issue, which leads to an increase in water conductivity, remains to be fully addressed.

In-depth investigations going forward should centre on probing for the existence of stray electrical currents within the system. These stray currents have the potential to significantly expedite the corrosion process. Identifying and mitigating any stray currents will be essential to tackling the core problem at hand.

Moreover, there is a practical need to transition towards automating the water change process. Presently, the manual intervention required for water replacement introduces the risk of human error, including the inadvertent introduction of air into the circuit. Automating this procedure would reduce the possibility of errors.

Conclusions

The research outlined in this thesis primarily focused on understanding corrosion-erosion phenomena within the primary circuits of nuclear reactors and fusion facilities. Specifically, this Industrial Doctorate project aimed to investigate the causes of water chemistry degradation and corrosion-erosion within components of the ITER Neutral Beam Test Facility (NBTF) that utilize ultrapure water with high resistivity values of up to 10 MΩ·cm. The NBTF, located at Consorzio RFX in Padua, Italy, hosts two key experiments: MITICA, a 1 MeV full-scale prototype of the ITER Neutral Beam Injector (NBI), and SPIDER, the low-energy 100 keV ITER HNB full-size Ion Source.

Ultrapure water is used as a coolant in the primary circuits of SPIDER and MITICA, and it interacts with the inner surfaces made of copper and stainless steel. This interaction results in the thinning of cooling channel walls. This degradation process involves both chemical and electrochemical reactions, leading to corrosion and mechanical surface modifications referred to as erosion. The combined effect of corrosion and erosion, causing material wastage, is termed "corrosion-erosion." Preventing and monitoring these phenomena is vital to enhance the performance and longevity of SPIDER, MITICA, and future fusion facilities. Water chemistry plays a critical role in minimizing the formation of corrosion products and insulating high-tension components.

The thesis investigations can be categorized into two main research areas: metal degradation analysis using metal release tests and water degradation in NBTF primary circuits through water circulation tests.

In the metal degradation analysis section, the focus was on assessing the corrosion rates of stainless steel (SS) and copper (Cu) within the primary cooling systems of SPIDER and MITICA. These systems are primarily constructed from copper alloys and stainless steel. Metal release tests were conducted under two different environmental conditions: SS and Cu samples exposed individually and coupled together in a high oxygen environment; and SS and Cu samples exposed individually in both high and reducing environments. All experiments were conducted in stagnant water at ambient temperature. The corrosion rate of SS and Cu were determined when these materials were coupled and joined, as is the case in NBTF, using a specific joining technique known as Vacuum Tight Threaded Junction (VTTJ). Metal release tests were then compared with preliminary Stress Corrosion Cracking (SCC) tests conducted using the microcapillary method. The key findings from these metal analyses were as follows:

- The coupling of SS and Cu did not significantly affect the release of metal ions but only the SCC initiation behaviour. SCC tests revealed that SS samples exposed individually to high-oxygen (HO) conditions exhibit slightly higher resistance to localized corrosion compared to SS coupled with copper.

- Experiments conducted in high-oxygen environments showed an increase in the release of copper ions over time due to the presence of oxygen. In contrast, experiments in a controlled glove box environment with reduced oxygen levels inhibited the release of copper ions.
- SS samples released a comparable amount of ions in HO and LO conditions. This behaviour was clarified by the combination of potentiodynamic and galvanostatic results. A passive layer does not form on the SS surface when DO levels are low. Consequently, the SCC behaviour worsens for SS samples exposed to LO conditions compared to HO conditions.
- The type of oxide formed on the surface of copper varied depending on the oxygen conditions. In high-oxygen environments, mainly tenorite was formed, which did not provide effective protection against further metal. Potentiodynamic polarization results underscored the fact that neither tenorite nor cuprite serves as a reliable barrier to prevent ongoing corrosion of the metal

In the water degradation analysis sections, the research focused on investigating water degradation within some of the primary circuits of SPIDER and MITICA. The most significant degradation was observed in the primary circuit cooling the power supplies, named as PC01 for SPIDER and PC08 for MITICA. Controlled circulation tests were carried out at a constant temperature and flow rate to estimate the increase in water conductivity and measure the concentration of metallic cations dissolved in the water using the Inductively Coupled Plasma-Mass Spectrometry (ICP-MS) technique.

Regarding SPIDER, a preliminary assessment of water conductivity degradation was carried out. This assessment involved calculating the wetted areas constructed from copper and stainless steel, as well as determining the volumes within PC01, PC02, and PC03 circuits. The analyses pointed out that theoretically all three circuits have the same degradation rate, but in reality PC01 is the only one showing a water degradation 6.4 higher with respect the estimated. Water circulation test were priorly performed in PC01 at constant temperature and flowrate by inserting (“ISEPS in” configuration) and excluding ISEPS in the circuit (“bypass” configuration). The results showed that when ISEPS was included in the loop, higher conductivity degradation was observed. Furthermore, a significant increment of Cu and Zn was detected in “ISEPS in” experiment accompanied by an increment of water conductivity if compared with the “bypass configuration” experiment. To understand the entity of water contamination, the results of these experiments were compared with those from circulation tests performed on PC03, which contains various copper components. The analysis revealed that PC01, in the "bypass configuration," exhibited higher levels of copper metallic ions in solution and conductivity increase compared to PC03. This finding suggested that the source of copper in PC01 was related to corrosion processes and was not solely attributable to the presence of stainless steel and copper components. Further experiments

involved the application of voltage within the PC01 water circulation. These tests conclusively demonstrated that the deterioration in water quality was not linked to the application of voltage within the circuit. Instead, it was directly associated with the specific hydraulic configuration of the circuit.

The research confirmed that the high releases of copper in PC01 were indeed connected to the presence of undesired components. Zinc components, such as pressure reducers with zinc springs and plastic tubes containing zinc oxide particles, were identified during the investigation. While some pressure reducers were replaced, others remained to be detected and addressed.

In summary, the analysis of PC01 indicated a correlation between the increase in water conductivity and the release of cations, with the major contributing factors being the presence of impurities and undesired components, which led to elevated copper releases. Backflow tests further highlighted the entry of air into the circuit. To address these issues, online sensors were recommended and subsequently installed in a SPIDER primary circuit. These sensors are designed to continuously monitor oxygen levels and pH, with their data planned for use when SPIDER resumes operation.

In the case of MITICA, the assessment of water degradation in PC08 was conducted through circulation tests similar to those carried out for SPIDER PC01. The research findings indicated that the primary factor contributing to water degradation in MITICA PC08 was inadequate control of water chemistry, rather than the release of metals. One significant issue affecting water chemistry was the unintentional entry of air into the circuit, which could be attributed to operational errors. Additionally, stagnant water samples collected from plastic tubes within the power supplies unexpectedly revealed traces of copper and zinc. Notably, these plastic tubes were also used in SPIDER PC01.

The research aimed to draw connections between the observations made in metal release tests and water circulation tests, leading to proposed circuit improvements to mitigate water degradation and prevent the thinning of cooling channel walls. These proposed modifications were implemented in a MITICA primary circuit. One key strategy was to minimize the ingress of air from elevated locations within the plant, especially considering that the highest point in the MITICA system is located 12 meters above ground level. This was achieved by increasing the pressurizer working pressure from 2.5 bar to 4.8 bar. Subsequent water circulation tests demonstrated that elevating the working pressure effectively reduced the ingress of air from high points in the system, thereby contributing to the maintenance of the desired water chemistry conditions. These findings emphasized the importance, especially for future facilities, of identifying the highest points within the cooling system and establishing general guidelines to prevent air from entering these points.

Additionally, online mixed bed resins were introduced to ensure a continuous purification of water in the primary loops, thereby maintaining low levels of water conductivity as a first complemental solution to the cyclical replacement of degraded water. This approach has proven effective in managing water conductivity, but it should be noted that it represents a short-term solution rather than a comprehensive resolution to the root problem responsible for water degradation. The underlying cause of the issue, which leads to an increase in water conductivity, remains to be fully addressed Another strategy implemented was the introduction of online mixed bed resins to ensure continuous water purification in the primary loops. This approach effectively maintained low levels of water conductivity and served as an initial solution alongside the cyclical replacement of degraded water. However, it is essential to note that this method represents a short-term solution rather than a comprehensive resolution to the underlying problem responsible for water degradation. The root cause of the issue, leading to increased water conductivity, still requires a comprehensive solution.

Future Works

This thesis underscores the critical importance of implementing best practices for managing water quality in nuclear reactors and fusion facilities. Inadequate control of water quality and poor material selection for components in contact with water can lead to corrosive processes that negatively impact both the equipment and the overall operation of reactors and facilities.

While nuclear reactors that use water as a coolant have developed extensive knowledge and practices for managing water chemistry, fusion facilities are still in the process of establishing comprehensive guidelines. It is imperative to define recommended parameters, applicable techniques, sampling procedures, sampling frequency for monitoring water quality, and the development of quality assurance and water management programs. This groundwork is particularly vital given the construction of fusion reactors worldwide, such as ITER and DTT, which will dominate future fusion operation programs.

In this chapter, future work that can help clarify the remaining unknowns is discussed. One proposed area of study involves examining pre-passivated stainless steel samples in reducing environments to assess how the protective oxide layer behaves when exposed to ultrapure water (UPW) with low oxygen content. This investigation will help understand the effects of subjecting SS samples to a reducing environment after they have developed a protective passivating layer, with attention to the actual impact of oxygen levels. Various procedures for pre-passivating the samples are being considered, with guidance from ASTM A967/A967M-17 [70] expected to help in identifying the most appropriate pre-passivation method.

Furthermore, the integrity of the passive layer on stainless steel formed in different environments will be evaluated under cyclic operational modes that alternate between oxidizing and reducing conditions, as expected in facilities like ITER, JT-60SA, and DTT. The protective films that can form on material surface can be attacked in the presence of some chemicals, which this can lead to dissolution of the metal. In cases where these films undergo mechanical damage or chemical weakening, localized corrosion in the form of pitting may ensue. The study will also include investigating surface passivation during the immersion time using electrochemical techniques to assess oxide evolution over exposure time to alternating environmental conditions. Moreover, analyses of the passive layer using surface techniques such as XPS will be conducted.

As discussed in the thesis, multiple incidents leading to component failures have been documented in fusion facilities like JET and DaΘne. To address this concern, a comprehensive analysis of the relationship between local water chemistry and water flow regimes is being considered. This analysis aims to provide insights into the assessment, prediction, and prevention of localized corrosion, ultimately contributing to safety and operational reliability. The use of simulations tool to evaluate localize corrosion on the basis

of water turbulence prediction, change in pressure and water chemistry parameters in under consideration.

The future strategy involves initiating the process of accumulating experience by examining components utilized in fusion facilities such as JET, which is expected to conclude its experimental operations and undergo dismantling within the next year. These components have been in service for an extended period under specific experimental conditions. The examination of the internal structures of these components will serve as a starting point for establishing a direct correlation between actual operational conditions and their tangible impact on material surfaces.

The water circulation tests conducted in this thesis work have highlighted the critical significance of designing the cooling circuit with careful consideration of hydrodynamics. The results underscored the importance of identifying the highest points within the cooling system, particularly with an eye toward future facilities. It is crucial to establish general guidelines aimed at preventing the ingress of air at these specific points in the cooling system. Drawing from the experience gained in nuclear reactors that utilize water as a coolant, valuable insights can be collect and used in designing cooling systems for future fusion facilities like DTT and ITER. Future steps will be the collaboration with teams working in these facilities to share the knowledge acquired during this three-year doctoral research project.

Regarding future developments at the NBTF facility, there are several plans in place. One of the key initiatives involves the replacement of the existing resins in PC08 with new ones specifically designed to operate at conductivity levels below 0.3 uS/cm. These resins are also planned to be installed in PC01. Additionally, in-depth investigations will focus on probing for the existence of stray electrical currents within the system, as these currents have the potential to significantly expedite the corrosion process in primary circuits cooling the power supplies.

Furthermore, the comprehensive study has drawn attention to a notable vacancy within the NBTF cooling plant – the absence of an inline Chemical and Volume Control System (CVCS). Currently, the Chemical and Control System (CCS) operates offline, lacking the capability for real-time monitoring of water chemistry parameters. This deficiency necessitates the daily replacement of water in PC01 and PC08, which hinders facility operations. To address this issue and enhance the reliability and efficiency of SPIDER and MITICA operations, potential improvements to the NBTF cooling plant's design will be thoroughly examined and evaluated.

As a short-term modification in NBTF cooling plane, there are plans to transition towards automating the water change process. The current manual intervention required for water replacement carries the risk of human error, including the inadvertent introduction of air into the circuit. The automation of this procedure is expected to reduce the likelihood of errors, further enhancing the operational efficiency and safety of the facility.

As general guideline, future fusion facilities that intend to utilize ultrapure water should take into account the research and analyses conducted within nuclear power plants to ensure consistent and reliable operations, as well as the integrity of components. The careful selection of appropriate materials and the thorough crafting of technical specifications for companies during the design phase are of utmost importance in constructing an efficient cooling plant, particularly from a hydrodynamic perspective. These measures are essential to prevent impurities from compromising the integrity and performance of the system.

Acknowledgements

I really wanted to write my acknowledgments in English, but unfortunately my heart is not a native speaker… therefore here are my "ringraziamenti" in Italian.

Vorrei incominciare ringraziando Piergiorgio Sonato che mi richiamato al Consorzio quando avevo già iniziato a lavorare in azienda… se non fosse per te, ora sicuramente non sarei qua. Magari con un titolo di studio in meno e forse più ricca, ma sicuramente meno felice e soddisfatta!

Un ringraziamento di cuore va a tutto il "Team COOLing" che in questi anni è stata una garanzia di successi. Moreno e Gaetano siete mitici e instancabili! Il "workout cooling tour" dovrebbe essere proposto alla comunità scientifica per attivare muscoli e neuroni. Matteo, il SAVIO, grazie per avermi presentato con pazienza subdola l'impianto di raffreddamento per poi scaricare la patata bollente a me! Un grazie particolare a Claudia, ahimè ex membro del team… mi hai introdotta nel mondo della chimica dell'acqua con passione e dato luce al mio lavoro quando era ancora tutto nebuloso!

Un grazie va a Mauro Dalla Palma che mi hai motivato e energizzato in questi anni, soprattutto in questo ultimo periodo di stress in cui l'impossibile è dovuto diventare possibile!

Un super grazie anche a Alessandra Canton, che per la terza volta mi hai letto il malloppone scritto e ti sei aggiudicata il titolo di amuleto porta fortuna!

E se la tesi è stata svolta, sviluppata, scritta, è grazie alla collaborazione fra vari istituti che mi hanno supportata coi lori preziosi consigli e forte esperienza. Quindi un grazie a INFN Legnaro e la sua officina meccanica; a INFN Padova per avermi fatto conoscere Valentina, amica di analisi SEM; al CEASC che mi ha dato l'opportunità di fare analisi superficiali sui campioni; a UNIPD Dipartimento di Chimica che ha analizzato carrellate di provette d'acqua e a ICMATE che mi ha concesso di usare i suoi laboratori di Materiali e mi ha dato un gran sostegno anche nell'analizzare e interpretare tutti i dati.

Grazie a tutti i ragazzi del Consorzio, che in questi anni hanno sempre colorato le serate con gioia, allegria e… un po' di birrette al momento giusto con tavolate da 30 persone. Un grazie in particolare va a voi, Gio e Susy, mie testimoni di nozze, e gran compagne di vita! Un grazie a tutto il restante team BIONDE DENTRO (Lola e Betta) … è stato strano fare questo percorso di studi senza di voi presenti tutto il giorno. E grazie a tutti gli amici storici che fra viaggetti e seratine continuiamo a condividere tanto! Siete un bellissimo team arcobaleno che dona gioia e brio! Non vedo l'ora di festeggiare con tutti voi, anche solo per la consegna di questa altra tesi (emmobasta!!!)

Un pensiero speciale va alla mia famiglia… nonno, nonna forse non avete capito ancora cosa è un dottorato, ma con il vostro ragù al cinghiale, baccalà alla livornese e costante affetto (e affettato) siete sempre una forza incredibile. Zizza, sei sempre la voce acuta ma pazzerella che solleva dall'altra parte della cornetta. E mamma… grazie per continuare a sostenermi nei miei studi. Non ti preoccupare che prima o poi capirai che cosa ho fatto in questi tre anni (forse non l'ho capito ancora nemmeno io! ma shhh)

E non volevo fare la gattara, ma un pensiero va anche a te, piccola Milù, che mi hai accompagnato in ogni mia tesi, da quella di maturità fino anche a questa lasciandoci dopo ben 19 anni poco prima della consegna. In qualche modo hai messo la tua zampotta anche qui e lasciato il testimone a Ruffino, che vedo hai istruito a distanza a dovere su come acciambellarsi sulla tastiera di un PC.

Ed eccoci arrivati a te Pru… ovviamente ti ho messo alla fine perché piano piano hai assunto un ruolo cardine nella mia vita e pilastro di ogni mio progetto futuro. La fine di ogni capitolo è o non è già l'inizio di quello dopo? Sei stato la mia più grande fonte di felicità da fidanzato e il mio più grande investimento affettivo da marito. Il futuro è incerto ma con te è come affrontarlo con un corrimano sempre alla mia destra (che essendo molto goffa mi serve eccome!). Che sia Padova, Bologna, Genova, Roma o … Bangkok, è bello sapere che lo affronteremo assieme! Sparandoci anche qualche concerto qua e là, ovviamente. E birrette! Sì, Sì, non scordiamo l'alcool.

E a Te, che da anni continui ad avere quell'Invisible Touch sulla mia vita. Con quel tuo tocco paterno, riesci sempre a districare i nodi creati dalla sbadata moira Lachesi mentre intesse il filo della vita…dando origine ad una trama meravigliosa. Ti voglio bene

Bibliography

[1] C. Zou, Q. Zhao, G. Zhang, and B. Xiong, "Energy revolution: From a fossil energy era to a new energy era," *Nat. Gas Ind.*, vol. 36, no. 1, pp. 1–10, 2016, doi: 10.3787/j.issn.1000-0976.2016.01.001.

[2] G. Santos, "Road transport and CO2 emissions: What are the challenges?," *Transp. Policy*, vol. 59, no. November 2015, pp. 71–74, 2017, doi: 10.1016/j.tranpol.2017.06.007.

[3] M. J. Sadowski, "Nuclear fusion-energy for future," *Nukleonika*, vol. 50, no. June, pp. 53–58, 2005.

[4] R. Kembleton, "Nuclear fusion: What of the future?," in *Managing Global Warming: An Interface of Technology and Human Issues*, Elsevier, 2019, pp. 199–220.

[5] D. Ivanova, "Plasma-facing components in tokamaks: Material modification and fuel retention." KTH Royal Institute of Technology, 2012.

[6] F. Romanelli *et al.*, "Fusion Electricity: A roadmap to the realization of fusion energy," 2012.

[7] A. G. Peeters, "The physics of fusion power," *Lect. Notes*, pp. 1–77, 2009, [Online]. Available: papers3://publication/uuid/932E738E-3DC6-427D-8E80-4FB43A986437

[8] J. A. Romero *et al.*, "Sliding mode control of a tokamak transformer," *Proc. IEEE Conf. Decis. Control*, pp. 386–393, 2012, doi: 10.1109/CDC.2012.6426907.

[9] G. O. Ludwig, M. C. R. Andrade, M. Gryaznevich, and T. N. Todd, "Physics performance analysis of low-power tokamak reactors," *Nucl. Fusion*, vol. 49, no. 8, 2009, doi: 10.1088/0029-5515/49/8/085026.

[10] R. Aymar, "ITER overview," *Fusion Eng. Des.*, vol. 36, no. 1, pp. 9–21, 1997, doi: 10.1016/S0920-3796(97)00008-2.

[11] M. Kikuchi, K. Lackner, and M. Quang, "Fusion Physics," *Iaea*, pp. 24–26, 2012.

[12] P. Sonato *et al.*, "Status of PRIMA, the test facility for ITER neutral beam injectors," *AIP Conf. Proc.*, vol. 1515, no. 2013, pp. 549–558, 2013, doi: 10.1063/1.4792827.

[13] P. Sonato *et al.*, "The ITER full size plasma source device design," *Fusion Eng. Des.*, vol. 84, no. 2–6, pp. 269–274, Jun. 2009, doi: 10.1016/j.fusengdes.2008.11.095.

[14] V. Toigo *et al.*, "On the road to ITER NBIs: SPIDER improvement after first operation and MITICA construction progress," *Fusion Eng. Des.*, vol. 168, no. May, p. 112622, Jul. 2021, doi: 10.1016/j.fusengdes.2021.112622.

[15] D. Marcuzzi *et al.*, "Detail design of the beam source for the SPIDER experiment," *Fusion Eng. Des.*, vol. 85, no. 10–12, pp. 1792–1797, Dec. 2010, doi: 10.1016/j.fusengdes.2010.05.039.

[16] M. J. Singh, H. P. L. De Esch, R. Hemsworth, and D. Boilson, "Mo layer thickness

requirement on the ion source back plate for the HNB and DNB ion sources in ITER," in *AIP Conference Proceedings*, Apr. 2015, vol. 1655. doi: 10.1063/1.4916449.

[17] G. Serianni *et al.*, "SPIDER in the roadmap of the ITER neutral beams," *Fusion Eng. Des.*, vol. 146, no. April, pp. 2539–2546, Sep. 2019, doi: 10.1016/j.fusengdes.2019.04.036.

[18] F. Fellin, D. Marcuzzi, P. Zaccaria, and G. Agarici, "Proposal of cooling plant, for SPIDER and MITICA experiments," *Fusion Eng. Des.*, vol. 86, no. 6–8, pp. 843–846, 2011, doi: 10.1016/j.fusengdes.2011.04.030.

[19] A. Interanational, "Designation : D 1193 – 06 Standard specification for reagent water," 2006.

[20] T. S. Light, E. A. Kingman, A. C. Bevilacqua, and T. Associates, "cond_CO2," pp. 0–17, 1995.

[21] T. S. Light, S. Licht, A. C. Bevilacqua, and K. R. Morash, "The fundamental conductivity and resistivity of water," *Electrochem. Solid-State Lett.*, vol. 8, no. 1, pp. 16–19, 2005, doi: 10.1149/1.1836121.

[22] A. C. Bevilacqua, "Ultrapure Water–The Standard for Resistivity Measurements of Ultrapure Water," *1998 Semicond. Pure Water Chem. Conf.*, pp. 2–5, 1998, [Online]. Available: http://www.snowpure.com/docs/thornton-upw-resistivity-measurement.pdf

[23] D. Lioce *et al.*, "ITER Tokamak Cooling Water System Design Status," *Fusion Sci. Technol.*, vol. 75, no. 8, pp. 841–848, 2019, doi: 10.1080/15361055.2019.1644135.

[24] J. Zhang, L. Li, S. He, and Y. Chen, "Calculation of Radioactivity and Dose Rate of Activated Corrosion Products in Water-Cooled Fusion Reactor," *Sci. Technol. Nucl. Install.*, vol. 2016, 2016, doi: 10.1155/2016/6051834.

[25] C. Harrington *et al.*, "Chemistry and corrosion research and development for the water cooling circuits of European DEMO," *Fusion Eng. Des.*, vol. 146, no. December 2018, pp. 478–481, 2019, doi: 10.1016/j.fusengdes.2018.12.095.

[26] G. Federici *et al.*, "DEMO design activity in Europe: Progress and updates," *Fusion Eng. Des.*, vol. 136, no. September 2017, pp. 729–741, 2018, doi: 10.1016/j.fusengdes.2018.04.001.

[27] A. Petrov, "Assessment of Radiolysis in Tokamak Cooling Water System of Iter Fusion Reactor," *21st Int. Conf. Water Chem. Nucl. React. Syst.*, 2018.

[28] D. D. Macdonald, G. R. Engelhardt, and A. Petrov, "A Critical Review of Radiolysis Issues in Water-Cooled Fission and Fusion Reactors: Part I, Assessment of Radiolysis Models," *Corros. Mater. Degrad.*, vol. 3, no. 3, pp. 470–536, 2022, doi: 10.3390/cmd3030028.

[29] H. Kawamura *et al.*, "BWR water chemistry guidelines and PWR primary water chemistry guidelines in Japan – Purpose and technical background," *Nucl. Eng. Des.*, vol. 309, pp. 161–174, Dec. 2016, doi: 10.1016/j.nucengdes.2016.08.029.

[30] E. Riché, A. Carrié, N. Andin, and S. Mabic, “Application Note: High Purity Water and pH,” *Am. Lab.*, no. July, 2006, [Online]. Available: www.aln20.com/newproducts

[31] R. Dortwegt, “Low-conductivity water systems for accelerators,” *Proc. IEEE Part. Accel. Conf.*, vol. 1, pp. 630–634, 2003, doi: 10.1109/pac.2003.1288995.

[32] INTERNATIONAL ATOMIC ENERGY AGENCY, “Good practices for water quality management in research reactors and spent fuel storage facilities,” *IAEA Nucl. Energy Ser.*, vol. No. NP-T-5, no. NP-T-5.2, p. 151, 2011, [Online]. Available: https://www.iaea.org/publications/8539/good-practices-for-water-quality-management-in-research-reactors-and-spent-fuel-storage-facilities

[33] R. Svoboda, “PPCHEM DISSOLVED GASES IN WATER A Practical View on the Dissolution of Air in Demineralized Water ABSTRACT,” no. September, 2020, doi: 344168847.

[34] H. Kawamura *et al.*, “BWR water chemistry guidelines and PWR primary water chemistry guidelines in Japan – Purpose and technical background,” *Nucl. Eng. Des.*, vol. 309, pp. 161–174, 2016, doi: 10.1016/j.nucengdes.2016.08.029.

[35] A. Molander, “Corrosion and water chemistry aspects concerning the tokamak cooling water systems of ITER,” *AIChE Annu. Meet. Conf. Proc.*, 2008.

[36] J. J. Barron and C. Ashton, “Conductivity Measurement - A REAGECON TECHNICAL PAPER,” *A Pract. Guid. to Accurate Conduct. Meas.*, vol. 7, no. 3, pp. 1–5, 2013, [Online]. Available: http://www.camlabworld.com/originalimages/sitefiles/Tech_papers/TempCondMeas.pdf

[37] E. Ljungberg, L.; Hallden, “BWR Water Chemistry Impurity Studies: Literature Review of Effectes on Stress Corrosion Cracking,” *EPRI*, 1984.

[38] D. Lister and S. Uchida, “Determining water chemistry conditions in nuclear reactor coolants,” *J. Nucl. Sci. Technol.*, vol. 52, no. 4, pp. 451–466, 2015, doi: 10.1080/00223131.2014.973460.

[39] L. W. Gordon, B. M,; Jewett, C. W.; Pickett, A. E.; Indig, A. E.; Andresen, P. L.; Niedrach, “Hydrogen Water Chemistry for BWRs,” *EPRI*, 1985.

[40] P. Aaltonen and H. Hanninen, “Water chemistry and behaviour of materials in PWRs and BWRs,” *Des. approaches Heat. React. Rep. an Advis. Gr. Meet.*, pp. 205–222, 1997, [Online]. Available: https://www.cambridge.org/core/product/identifier/S0007125000082039/type/journal_article

[41] S. C. P. and E. K. K. Yang Ho Cheon ∗ and Nam Yeong Lee, Byeong Ho Park, “Primary Coolant pH Control for Soluble Boron-Free PWRs.” 2015.

[42] M. Lips, “Water chemistry in pressurized water reactors - A Gösgen-specific overview,” *Chimia (Aarau).*, vol. 59, no. 12, pp. 929–937, 2005, doi: 10.2533/000942905777675372.

[43] K. Ishida *et al.*, "Hydrazine and hydrogen co-injection to mitigate stress corrosion cracking of structural materials in boiling water reactors (V) effects of hydrazine and dissolved oxygen on flow accelerated corrosion of carbon steel," *J. Nucl. Sci. Technol.*, vol. 44, no. 2, pp. 222–232, 2007, doi: 10.1080/18811248.2007.9711276.

[44] V. Kain, "Flow accelerated corrosion: Forms, mechanisms and case studies," *Procedia Eng.*, vol. 86, pp. 576–588, 2014, doi: 10.1016/j.proeng.2014.11.083.

[45] S. Trevin, "Flow accelerated corrosion (FAC) in nuclear power plant components," *Nucl. Corros. Sci. Eng.*, pp. 186–229, 2012, doi: 10.1533/9780857095343.2.186.

[46] P. Agostinetti, F. Degli Agostini, and P. Sonato, "Application of the novel VTTJ technique (Vacuum Tight Threaded Junction) to fusion reactor relevant geometry and materials," *Fusion Eng. Des.*, vol. 124, pp. 659–663, 2017, doi: 10.1016/j.fusengdes.2017.01.048.

[47] S. Lozano-perez, T. Yamada, T. Terachi, and M. Schro, "Multi-scale characterization of stress corrosion cracking of cold-worked stainless steels and the influence of Cr content," vol. 57, pp. 5361–5381, 2009, doi: 10.1016/j.actamat.2009.07.040.

[48] B. Stellwag, "The mechanism of oxide film formation on austenitic stainless steels in high temperature water," *Corros. Sci.*, vol. 40, no. 2–3, pp. 337–370, 1998, doi: 10.1016/S0010-938X(97)00140-6.

[49] R. Svoboda, C. Picech, and H. Hehs, "Experiences with stainless steel hollow conductors for generator stator water cooling," *Am. Soc. Mech. Eng. Power Div. PWR*, vol. 35, no. January 2004, pp. 373–377, 2004, doi: 10.1115/POWER2004-52155.

[50] A. Molander, "A Review of Corrosion and Water Chemistry Aspects Concerning the Tokamak Cooling Water Systems of Iter," 2008.

[51] T. Shoji, Z. Lu, and Q. Peng, "Factors affecting stress corrosion cracking (SCC) and fundamental mechanistic understanding of stainless steels," *Stress Corros. Crack. Theory Pract.*, pp. 245–272, 2011, doi: 10.1533/9780857093769.3.245.

[52] F. P. Ford and J. Povich, "Effect of Oxygen Temperature Combinations on the Stress Corrosion Susceptibility of Sensitized Type 304 Stainless Stell in High Purity Water.," *Corrosion*, vol. 35, no. 12. pp. 569–574, 1979. doi: 10.5006/0010-9312-35.12.569.

[53] R. Svoboda and D. A. Palmer, "Behaviour of Copper in Generator Stator Cooling-Water Systems," pp. 1–6, 2008.

[54] M. Shannon and E. Surrey, "Failure of Ion Backplates on JET," 2006.

[55] L. Pellegrino, "Experience with long term operation with demineralized water systems at Dafne," *Proc. EPAC 2004, Lucerne, Switz. Exp.*, pp. 2080–2082, 2004.

[56] R. Svoboda, "Interpretation of stator cooling water chemistry data," no. March 2018, 2019.

[57] C. N. Cleveland, "Corrosion of Copper in Deaerated Deionized Water and Geometry Induced Frequency Dispersion of the Ring Electrode," *J. Chem. Inf. Model.*, vol. 53,

no. 9, pp. 1689–1699, 2013.

[58] R. Svoboda, “Corrosion and Deposits in Water-Cooled Generator Stator Windings : Overview of Water Cooling of Generators,” vol. 20, no. October 2018, pp. 297–309, 2019.

[59] R. Svoboda, “Corrosion and Deposits in Water-Cooled Generator Stator Windings : Part 1 : Behaviour of Copper Author ’ s Copy,” no. October 2018, 2019.

[60] R. Svoboda, “Corrosion and Deposits in Water-Cooled Generator Stator Windings : Part 3 : Removal of Flow Restrictions,” vol. 20, no. October 2018, pp. 297–309, 2019.

[61] T. Bauer, M. Svoboda, S. Dockheer, and R. Svoboda, “Chemical Cleaning of Water-Cooled Generators : Effect on System Materials Chemical Cleaning of Water-Cooled Generators : Effect on System Materials,” no. December, 2019.

[62] R. Dortwegt and E. V. Maughan, “The chemistry of copper in water and related studies planned at the advanced photon source,” *Proc. IEEE Part. Accel. Conf.*, vol. 2, pp. 1456–1458, 2001, doi: 10.1109/pac.2001.986712.

[63] M. S. Breimesser, S. Ritter, H.-P. Seifert, T. Suter, and S. Virtanen, “A New Approach towards the Characterization of IG SCC of Austenitic Stainless Steel by the Electrochemical Microcapillary Technique,” *ECS Meet. Abstr.*, vol. MA2011-02, no. 22, pp. 1694–1694, 2011, doi: 10.1149/ma2011-02/22/1694.

[64] A. Yazdanpanah, L. Pezzato, and M. Dabalà, “Stress corrosion cracking of AISI 304 under chromium variation within the standard limits: Failure analysis implementing microcapillary method,” *Eng. Fail. Anal.*, vol. 142, no. August, 2022, doi: 10.1016/j.engfailanal.2022.106797.

[65] A. Yazdanpanah, M. Franceschi, R. I. Revilla, S. Khademzadeh, I. De Graeve, and M. Dabalà, “Revealing the stress corrosion cracking initiation mechanism of alloy 718 prepared by laser powder bed fusion assessed by microcapillary method,” *Corros. Sci.*, vol. 208, no. August, 2022, doi: 10.1016/j.corsci.2022.110642.

[66] P. Agostinetti *et al.*, “Vacuum Tight Threaded Junctions (VTTJ): A new solution for reliable heterogeneous junctions in ITER,” *Fusion Eng. Des.*, vol. 96–97, pp. 48–55, 2015, doi: 10.1016/j.fusengdes.2015.04.010.

[67] Alfred E. Bauer, “Stainless Steel in Waters: Galvanic Corrosion and its Prevention,” *Stainl. Steel Waters Galvanic Corros. its Prev.*, p. 15, [Online]. Available: http://www.nickelinstitute.org/~/Media/Files/TechnicalLiterature/StainlessSteelinWatersGalvanicCorrosionandit PreventionAEBauer.pdf#page=

[68] The European Stainless Steel Development Association, “Stainless Steel in Contact with Other Metallic Materials,” *Mater. Appl. Ser.*, vol. 10, pp. 1–24, 2009.

[69] M. Yahia, “Effect of demineralized water on carbon steel and stainless steel,” *ResearchGate*, no. May, 2016, doi: 10.13140/RG.2.2.22719.71845.

[70] J. F. Rios, J. A. Calderón, and R. P. Nogueira, “Electrochemical behavior of copper in drinking water: Evaluation of dissolution process at low anodic overpotential,” *J.*

Braz. Chem. Soc., vol. 22, no. 7, pp. 1362–1370, 2011, doi: 10.1590/S0103-50532011000700023.

[71] N. Mazinanian, I. Odnevall Wallinder, and Y. Hedberg, "Comparison of the influence of citric acid and acetic acid as simulant for acidic food on the release of alloy constituents from stainless steel AISI 201," *J. Food Eng.*, vol. 145, no. March 1973, pp. 51–63, 2015, doi: 10.1016/j.jfoodeng.2014.08.006.

[72] UNI EN ISO 17294-2, "Water quality — Application of inductively coupled plasma mass spectrometry (ICP-MS) — Part 2: Determination of selected elements including uranium isotopes," *Int. Stand.*, p. 31, 2016, [Online]. Available: https://www.iso.org/standard/62962.html

[73] ASME International, "ASTM A967/A967M-17 : Standard Specification for Chemical Passivation Treatments for Stainless Steel Parts," *ASTM standard*. 2007.

[74] C. Gasparrini *et al.*, "Water Chemistry in Fusion Cooling Systems : Borated Water for DTT Vacuum Vessel," pp. 28–32, 2022.

[75] W. Niu, Z. Li, F. Ernst, and R. S. Lillard, "The passivity of low-temperature carburized austenitic stainless steel AISI-316L in a simulated boiling-water-reactor environment," *J. Nucl. Mater.*, vol. 537, 2020, doi: 10.1016/j.jnucmat.2020.152197.

[76] N. Mazinanian, G. Herting, I. Odnevall Wallinder, and Y. Hedberg, "Metal release and corrosion resistance of different stainless steel grades in simulated food contact," *Corrosion*, vol. 72, no. 6, pp. 775–790, 2016, doi: 10.5006/2057.

[77] X. Dong, R. G. Iacocca, B. L. Bustard, and C. A. J. Kemp, "Investigation of stainless steel corrosion in ultrahigh-purity water and steam systems by surface analytical techniques," *J. Mater. Eng. Perform.*, vol. 19, no. 1, pp. 135–141, 2010, doi: 10.1007/s11665-009-9430-x.

[78] D. W. Green and R. H. Perry, *Perry's chemical engineers' handbook*. McGraw-Hill Education, 2007. [Online]. Available: http://books.google.com/books?id=X1wIW9TrqXMC&pgis=1

[79] T. E. Eriksen, P. Ndalamba, and I. Grenthe, "On the corrosion of copper in pure water," *Corros. Sci.*, vol. 29, no. 10, pp. 1241–1250, Jan. 1989, doi: 10.1016/0010-938X(89)90071-1.

[80] N. Baluc, "Corrosion issues in thermonuclear fusion reactors and facilities," *Nucl. Corros. Sci. Eng.*, pp. 906–938, 2012, doi: 10.1533/9780857095343.6.906.

[81] M. Frankel, *Facility Piping System*, Second. 2002.

[82] "Standard Practice for Handling of Ultra-Pure Water Samples," *ASTM D4453-17*, vol. 91 (August, pp. 2–6, 2017, doi: 10.1520/D4453-17.

[83] M. Bigi *et al.*, "Design, manufacture and factory testing of the Ion Source and Extraction Power Supplies for the SPIDER experiment," *Fusion Eng. Des.*, vol. 96–97, pp. 405–410, 2015, doi: 10.1016/j.fusengdes.2015.06.163.

[84] V. Toigo *et al.*, “Progress in the ITER neutral beam test facility,” *Nucl. Fusion*, vol. 59, no. 8, p. 086058, Aug. 2019, doi: 10.1088/1741-4326/ab2271.

[85] V. Toigo *et al.*, “The PRIMA Test Facility: SPIDER and MITICA test-beds for ITER neutral beam injectors,” *New J. Phys.*, vol. 19, no. 8, p. 85004, 2017, doi: 10.1088/1367-2630/aa78e8.

[86] L. Zanotto *et al.*, “A strategy to identify breakdown location in MITICA test facility: results of high voltage test campaign,” *Fusion Eng. Des.*, vol. 187, 2023, doi: 10.1016/j.fusengdes.2022.113381.

[87] M. Boldrin *et al.*, “Final design of the High Voltage Deck 1 and Bushing for MITICA: The ITER Heating Neutral Beam Injector prototype,” *Fusion Eng. Des.*, vol. 123, pp. 395–399, 2017, doi: 10.1016/j.fusengdes.2017.03.133.

[88] M. Boldrin *et al.*, “The High Voltage Deck 1 and Bushing for the ITER Neutral Beam Injector: Integrated design and installation in MITICA experiment,” *Fusion Eng. Des.*, vol. 146, no. August 2018, pp. 1895–1898, 2019, doi: 10.1016/j.fusengdes.2019.03.059.

[89] M. Boldrin *et al.*, “Partial discharges detection in 1 MV power supplies in MITICA experiment, the ITER heating neutral beam injector prototype,” *Fusion Eng. Des.*, vol. 187, no. December 2022, p. 113385, 2023, doi: 10.1016/j.fusengdes.2022.113385.

[90] C. Cavallini *et al.*, “Investigation of corrosion-erosion phenomena in the primary cooling system of SPIDER,” *Fusion Eng. Des.*, vol. 166, no. November 2020, p. 112271, 2021, doi: 10.1016/j.fusengdes.2021.112271.

[91] C. Gasparrini *et al.*, “Water Degradation in ITER Neutral Beam Test Facility Cooling Circuits,” *IEEE Trans. Plasma Sci.*, pp. 1–5, 2022, doi: 10.1109/tps.2022.3173737.

[92] I. M. Ageev and Y. M. Rybin, “Features of Measuring the Electrical Conductivity of Distilled Water in Contact with Air,” *Meas. Tech.*, vol. 62, no. 10, pp. 923–927, 2020, doi: 10.1007/s11018-020-01714-2.